

UNIVERSITY OF MINNESOTA

This is to certify that I have examined this bound copy of a doctoral thesis by

Yasser Moustafa Ibrahim Kadah

and have found that it is complete and satisfactory in all respects,  
and that any and all revisions required by the final  
examining committee have been made.

Xiaoping Hu

---

Name of Faculty Adviser

---

Signature of Faculty Adviser

---

Date

GRADUATE SCHOOL

NOVEL RECONSTRUCTION TECHNIQUES FOR  
MAGNETIC RESONANCE IMAGING

A THESIS

SUBMITTED TO THE FACULTY OF THE GRADUATE SCHOOL  
OF THE UNIVERSITY OF MINNESOTA

BY

Yasser Moustafa Ibrahim Kadah

IN PARTIAL FULFILLMENT OF THE REQUIREMENTS  
FOR THE DEGREE OF  
DOCTOR OF PHILOSOPHY

Xiaoping Hu, Adviser

June 1997

© Yasser Moustafa Ibrahim Kadah 1997

## ABSTRACT

The main acquisition and reconstruction technique in magnetic resonance imaging is the Fourier imaging technique. In spite of its success in conventional applications, it has some limitations when applied to unconventional areas such as magnetic resonance angiography and dynamic imaging. Moreover, its sensitivity to subtle deviations in the magnetic fields imposed by the technique results in a severe problem of geometric distortion. In this thesis, three novel reconstruction approaches that can solve some of the problems associated with Fourier imaging are proposed. The first, which is called pseudo-Fourier imaging, is a generalized spatial encoding method based on selective excitations with unconventional slice profiles combined with phase encoding. The classical selective excitation and Fourier encoding techniques are shown to be special cases of the new formulation. An example of using the new theory is described and implemented. The second and third approaches describe two new techniques to solve the geometric distortion problem. In the first, the data is processed with a correction kernel derived from the field map in the domain of the distorted images. The second technique recognizes the nature of the problem as an inverse problem of an ill-conditioned operator that can in general be estimated. The problem is discretized and several algebraic methods are introduced to invert the distortion operator in the least-squares sense. These proposed novel reconstruction techniques are important steps toward the expansion of the MRI usage in several unconventional applications such as stereotactic neurosurgery and radiotherapy treatment planning.

# TABLE OF CONTENTS

<b>List of Figures</b>	<b>viii</b>
<b>Chapter 1 Introduction</b>	<b>1</b>
1.1 Basic MRI Physics . . . . .	1
1.2 Imaging Techniques . . . . .	4
1.3 Magnetic Resonance Angiography (MRA) . . . . .	6
1.4 Clinical Applications . . . . .	7
<b>Chapter 2 Pseudo-Fourier Imaging (PFI)</b>	<b>9</b>
2.1 Background . . . . .	9
2.2 Theory . . . . .	11
2.2.1 Decomposition of continuous functions using frames . . . . .	11
2.2.2 Pseudo-Fourier imaging . . . . .	12
2.2.3 Formal reconstruction stability conditions . . . . .	14
2.3 Example of Applying PFI Theory . . . . .	15
2.4 Implementation under Practical Conditions . . . . .	16
2.5 Signal-to-Noise Ratio of PFI . . . . .	19
2.6 Potential Applications of PFI . . . . .	22
2.6.1 Volume imaging . . . . .	22
2.6.2 Magnetic resonance angiography (MRA) . . . . .	22
2.6.3 Dynamic imaging . . . . .	23
2.7 Experimental Verification of PFI . . . . .	23

2.8	Discussion . . . . .	25
<b>Chapter 3</b>	<b>Simulated Phase Evolution Rewinding (SPHERE)</b>	<b>35</b>
3.1	Background . . . . .	35
3.2	Theory . . . . .	37
3.3	Performance Analysis of SPHERE . . . . .	40
3.3.1	Special case 1: Blipped-EPI . . . . .	40
3.3.2	Special case 2: Segmented-EPI with centric-reordering . . . . .	41
3.3.3	General case of arbitrary trajectory . . . . .	42
3.3.4	Point spread function of SPHERE . . . . .	44
3.4	Method . . . . .	47
3.5	Results . . . . .	48
3.6	Discussion . . . . .	50
<b>Chapter 4</b>	<b>Algebraic Reconstruction for Magnetic Resonance Imaging under <math>B_0</math> Inhomogeneity</b>	<b>68</b>
4.1	Introduction . . . . .	68
4.2	General Problem formulation . . . . .	69
4.2.1	Continuous problem formulation . . . . .	69
4.2.2	Discretization . . . . .	71
4.2.3	Inhomogeneity problem in EPI: from 2-D to 1-D . . . . .	73
4.2.4	Example of a matrix operator . . . . .	74
4.3	Imaging Sequence Dependence . . . . .	76
4.4	Numerical Solution Methods . . . . .	78
4.4.1	SVD matrix solver . . . . .	78
4.4.2	Conjugate gradient method (CGM) matrix solver . . . . .	79
4.4.3	Solution constraining . . . . .	81

4.5	Experimental Results . . . . .	83
4.6	Discussion . . . . .	84
<b>Chapter 5</b>	<b>Conclusions</b>	<b>93</b>
	<b>Bibliography</b>	<b>96</b>

## LIST OF FIGURES

2.1	PFI data acquisition . . . . .	28
2.2	PFI reconstruction . . . . .	29
2.3	RF excitation related to the imaging window of PFI . . . . .	30
2.4	PFI excitation profile variation with flip angle . . . . .	30
2.5	Imaging window variation with flip angle . . . . .	31
2.6	Results of PFI compared to Fourier imaging . . . . .	32
2.7	Zoomed version of Fig.(2.6) to show the 1 mm resolution lines . . . . .	33
2.8	MIP images from PFI with imaging window size of 8 mm . . . . .	33
2.9	MIP images from PFI with imaging window size of 16 mm . . . . .	34
2.10	Illustration of spatial/k-space localization with PFI . . . . .	34
3.1	Block diagram of SPHERE . . . . .	56
3.2	Illustration of the different kernels used with SPHERE . . . . .	57
3.3	Correction ambiguity function . . . . .	58
3.4	Point spread function for segmented EPI with centric reordering . . . . .	59
3.5	Point spread function for spiral imaging . . . . .	60
3.6	Experimental results with blipped-EPI data . . . . .	61
3.7	Experimental results with segmented EPI with centric reordering phantom data . . . . .	62
3.8	Experimental results with segmented EPI with centric reordering human data . . . . .	63
3.9	Experimental results with spiral imaging phantom data . . . . .	64

3.10	Experimental results with spiral imaging human data . . . . .	65
3.11	Comparison between SPHERE and the conjugate phase method . . .	66
3.12	Segmented correction using SPHERE . . . . .	67
4.1	Comparison of the results of different discretization methods . . . . .	88
4.2	Correction of human data with 2-step conjugate gradient iteration. .	89
4.3	Comparison of blipped-EPI and segmented EPI with centric reordering for phantom data. . . . .	90
4.4	Comparison of blipped-EPI and segmented EPI with centric reordering for a coronal human brain scan. . . . .	91
4.5	Comparison of blipped-EPI and segmented EPI with centric reordering for a sagittal human brain scan. . . . .	92

## Chapter 1

### INTRODUCTION

Magnetic resonance imaging (MRI) is a powerful non-invasive tool for visualizing the inside of the human body. Like other medical imaging modalities, magnetic resonance images reflect the spatial distribution of certain tissue-dependent parameters. When a disease causes such parameters to change from their normal values, medical imaging is of great value to diagnose it as well as to identify its locations and spatial extent. In this perspective, MRI is of superior performance for its ability to create images that map one of several parameters or different parameter combinations. When this versatility is added to the inherently volumetric acquisition capabilities of the technique, MRI stands out as a unique diagnostic tool in medicine.

#### 1.1 Basic MRI Physics

The idea of MRI is based on the effect of high magnetic field on certain important atomic nuclei in the human body. All substances are affected to different extents when they are placed in a magnetic field. Among many substances in the body, the hydrogen nucleus (the proton) is the most interesting from the imaging point of view. This is mainly due to its abundance in all organic compounds in different amounts and distributions that would allow a clear distinction between them if proton images are acquired. In nature, protons, among other nuclei, have what is called *nuclear spin*. That is, they can be thought of as spinning around their axes the way Earth turns around its axis. When a nucleus spins, it has angular momentum and when that

spinning nucleus has a net charge, it also has a magnetic dipole moment. Magnetic dipole moments can be thought of as tiny bar magnets that are oriented in random directions in the absence of outside influences. In this state, the statistical vector sum of all dipole moments is zero. On the other hand, in the presence of a strong magnetic field, such bar magnets tend to align along the direction of that field. The vector sum of all magnetic dipole moments in this case tends to have a nonzero value, which is usually referred to as the *magnetization vector*  $\vec{M}$ . An important property of magnetic dipole moments is that they *precess*. This means that each of these vectors has a fixed tail while its head is revolving, resulting in a wobbling motion. The frequency of precession  $\omega$  is related to the magnetic field of strength  $B$  as,

$$\omega = \gamma \cdot B \tag{1.1}$$

where  $\gamma$  is termed the gyromagnetic ratio that is a constant for a given nucleus and equals to 42.577 MHz/T for the hydrogen nucleus. This important relation is called the *Larmor equation*.

As a result of the precession of magnetic dipoles, a radiofrequency signal can be detected by a coil placed around such precessing nuclei. The strength of this signal is a direct function of the number of magnetic dipoles or equivalently to the number of nuclei in the uniform field. If the imposed external magnetic field is designed to have a spatial variation in such a way to create an unambiguous mapping between the spatial locations and their precession frequencies given by Larmor equation, the reconstruction of images of the spatial distribution of a certain nucleus is possible in principle [1].

It should be noted that the number of spins that align with the magnetic field and generate the magnetization vector is a very small fraction of the total number of spins even under high magnetic fields. Specifically, this fraction is given by the *Boltzmann ratio* as a function of the magnetic field strength among other things. The magnetic field that is applied to align the spins is called the *static field* ( $B_0$ ), and is usually

chosen in the Tesla range to allow for reasonable values of the Boltzmann ratio. This precession of the magnetization vector  $\vec{M} = (M_x, M_y, M_z)$  can be expressed as a function of the applied magnetic field gradients  $\vec{B} = (B_x, B_y, B_z)$  by a set of approximate equations called the *Bloch equations* in the form:

$$\frac{dM_z}{dt} = \left(\frac{1}{T_1}\right) (M_o - M_z) + \gamma \cdot (\vec{M} \times \vec{B})_z \quad (1.2)$$

$$\frac{dM_x}{dt} = -\left(\frac{M_x}{T_2}\right) + \gamma \cdot (\vec{M} \times \vec{B})_x \quad (1.3)$$

$$\frac{dM_y}{dt} = -\left(\frac{M_y}{T_2}\right) + \gamma \cdot (\vec{M} \times \vec{B})_y \quad (1.4)$$

where  $M_o$  is the magnitude of the equilibrium magnetization vector. The time constants  $T_1$  and  $T_2$  are called the *spin-lattice* and *spin-spin* relaxation times respectively. The naming convention of the axes is such that the  $z$ -axis is along the applied static magnetic field, while the other two axes can be arbitrarily chosen. Starting from an arbitrary initial magnetization vector, these equations suggest that the magnetization components along the  $x$  and  $y$  axes take the form of dampen sinusoids while that along the  $z$ -axis is of exponential form. In other words, the magnetization vector spirals its way to its steady state position where it is oriented along the static magnetic field. This physical phenomenon is called the *free induction decay* (FID). Given that the relaxation times are direct functions of the type of substances within the imaged subject, it is possible in principle to obtain information about the composition of an imaged subject by observing the characteristics of its FID. This is usually done by using the above equations to tip the magnetization vector from its steady state position and then collect the resultant FID. This tipping of the magnetization vector was shown to be possible via applying an external RF pulse at the Larmor frequency. This was derived from an alternative form of the Bloch equations after a simple transformation of the coordinate system to what is called the *rotating frame of reference*. This transformation utilizes a set of coordinates that rotate with the spiraling magnetization vector providing more convenient forms for the solutions of

$M_x$  and  $M_y$  that are free of the RF frequency component. In other words, in this rotating frame, the magnetization vector is not spiraling. Also, its tipping angle is a direct function of the strength of the applied RF pulse and its duration [2].

## 1.2 Imaging Techniques

In order to reconstruct an image in MRI, a unique correspondence between the signal from a particular location within the field of view and its spatial position must be established. The most common imaging technique (and the one that brought MRI to reality) is what is called *Fourier imaging*. Fourier imaging achieves spatial encoding by employing linear magnetic field gradients across the imaged region. These gradients are utilized in two closely related fashions to perform spatial encoding through either changing the frequency or the phase of signals coming from different spatial positions. In either case, a Fourier transform of the FID signal would directly yield the desired image. This can be applied to one or all of the three spatial dimensions thus permitting a complete volumetric imaging. In a mathematical form, the return FID signal  $S(\vec{k})$  can be expressed as:

$$S(\vec{k}) = \int f(\vec{r}) \cdot e^{j2\pi\vec{k}\cdot\vec{r}} d\vec{r}. \quad (1.5)$$

The object  $f(\vec{r})$  can therefore be reconstructed as,

$$f(\vec{r}) = \int S(\vec{k}) \cdot e^{-j2\pi\vec{k}\cdot\vec{r}} d\vec{k}. \quad (1.6)$$

$S(\vec{k})$  is called the *k-space* representation of the object. The k-space vector  $\vec{k}$  is completely determined by the applied gradient strengths and their time dependence, which both define the trajectory of  $\vec{k}$  in the k-space during the period of the experiment. In the basic form of Fourier imaging, the k-space trajectory is selected to take a simple rectilinear form to yield a uniformly-sampled k-space representation that is suitable for discrete Fourier transform. Nevertheless, it is sometimes advantageous

to use other more complex trajectories. For example, spiral trajectories are used for their relatively shorter imaging time. A computational disadvantage of such trajectories arises when the k-space is sampled in a non-uniform fashion. In this case, the reconstruction involves some added complexity resulting from the need to apply a gridding procedure before the Fourier transform is used to obtain the image [2].

In conventional magnetic resonance imaging machines, Fourier imaging is implemented through small linear gradients along each of the three spatial axes. The FID signal from the precessing magnetization vector is detected by two coils arranged in quadrature to receive the signals corresponding to the  $x$  and  $y$  components of the magnetization vector. In a typical imaging experiment, the magnetization vector is tipped and the RF signal reflecting the FID phenomenon is observed. By selecting the time when the data are received (i.e., *echo time*,  $TE$ ) to control  $T_2$  relaxation and the repetition rate of the scanning (i.e., the reciprocal of the *repetition time*,  $TR$ ) to control  $T_1$  relaxation, proton density images weighted by one or a combination of these two parameters can be obtained quite flexibly.

Since it is only possible to receive a one-dimensional signal within any given time period, several techniques were suggested to achieve two-dimensional images through single or multiple one-dimensional FID signal acquisitions. The simplest of these is when one-dimensional acquisitions correspond to different lines of the two-dimensional k-space under constant gradients. After all lines covering the two-dimensional k-space area of interest are acquired sequentially, the two-dimensional image can be reconstructed. Alternatively, in the single FID acquisition case, time varying gradients are used to obtain the complete area of the two-dimensional k-space in a single-shot manner. This class of methods is called echo-planar imaging (EPI), and is considered of great value for many applications. EPI can be implemented in a variety of ways using different two-dimensional trajectories such as zigzag-EPI, blipped-EPI, or spiral EPI [2]. These techniques have the unique advantage of allowing extremely fast acquisition. On the other hand, they have the disadvantages of their susceptibility

to severe geometric distortions in the presence of magnetic field inhomogeneity, and their rather demanding requirements on the available magnetic field gradients.

### 1.3 Magnetic Resonance Angiography (MRA)

In addition to imaging tissues, MRI can also be used to visualize blood vessels in the field of view. When MRI is used for this purpose, it is usually called *magnetic resonance angiography* (MRA). The acquired vascular images in MRA look similar to those obtained by X-ray digital subtraction angiography (DSA). In general, MRA is performed by utilizing either of two major principles: time-of-flight (TOF) and phase contrast (PC). With TOF, the blood vessels visualized using a standard fast scan yield a bright signal as result of fresh spins in the moving blood and the steady state spin saturation phenomena in the stationary tissues. Subsequently, selective visualization of blood vessels in TOF MRA is achieved using the *maximum intensity projection* (MIP) algorithm. In this algorithm, the acquired volume data set is scanned along a projection direction to find the maximum intensity in all slices corresponding to the location of a given pixel in the projection plane. Then, this value is recorded in that location and the process is repeated for all pixels in the projection plane until a full projection image in that plane is collected. This resultant image is called the MIP image and is considered of important clinical value. It should be noted that the MIP algorithm can be used with volume data acquired through either multiple 2-D Fourier transform slices (2DFT) or 3-D Fourier transform (3DFT). These two methods have several relative advantages and disadvantages that make the choice between them for a particular application rather difficult. For example, the 3DFT technique has the advantages of better signal-to-noise ratio in addition to its ability to produce very thin slices. Unfortunately, it suffers from spin saturation problems that hinder the technique from imaging slowly flowing blood. On the other hand, even though a much less severe saturation problem exists with the 2DFT technique, this comes at the

expense of much lower signal-to-noise ratio and thicker slices. Therefore, the choice of which of these two techniques to use depends mainly on the relative importance of their contradicting characteristics as applied to the specific problem at hand [3].

The second technique, phase contrast (PC) MRA, makes use of a different principle to label the blood vessels, namely the signal phase arising from applying a balanced bipolar gradient pulse. This bipolar pulse does not have any effect on the stationary structures in the image since the positive and negative lobes of the gradient cancel out. On the other hand, for moving structures and flowing blood, an incomplete cancellation takes place resulting in a cumulative phase that is a direct function of the motion speed. Therefore, by observing this phase difference, it is possible to precisely derive an image of the vasculature as well as velocity maps [1].

## 1.4 Clinical Applications

MRI has been used extensively in many clinical applications. Those applications include its use to image the brain, the abdominal structures, the heart, as well as in detecting abnormalities in blood vessels in such cases as stroke. Nevertheless, there are some areas where MRI has not been as successful as other imaging modalities. For example, in stereotactic neurosurgery, x-ray computed tomography (CT) combined with x-ray digital subtraction angiography (DSA) is probably the only practical option [4]. In this procedure, an electrode or a biopsy needle is directed from the scalp to target structures deep within the brain [5]. Image data from multiple modalities are used to visualize the three-dimensional location of the target structure as related to the outside of the scalp. Also, it is important to detect the major blood vessels that can intercept the path of the surgical needle on its way to that target. Even though MRI has an advantage over other modalities for its ability to combine both structural and vascular imaging in an inherently volumetric acquisition, patient-dependent geometric distortion problems in addition to trade-offs between different techniques of

MRA acquisition hindered its use in important applications such as this. The geometric distortion, considered to be the main problem in this application, is the result of susceptibility mismatches that are present in many areas of the head especially near air cavities. This distortion renders the technique unsuitable for localizing deep structures for this high precision operation.

Another important application in which MRI has not been as successful is radiotherapy treatment planning [6, 7]. This application also requires precise definition of structures and blood vessels and therefore faces similar problems with MRI as stereotactic localization. Hence, it is clear that new acquisition and/or reconstruction techniques need to be devised to overcome these fundamental problems in order to make MRI more versatile and to extend its practical applications even further.

In this thesis, the problems of MRI acquisition and geometric distortion correction techniques are considered. In Chapter 2, the theory and experimental verification of a novel MRI spatial encoding technique are presented. The new technique has potential in several applications such as volume imaging, magnetic resonance angiography, and dynamic imaging. In Chapters 3 and 4, the theories and experimental verifications of two new approaches to solve the problem of geometric distortion are presented. The first approach proposes an inverse operator to reverse the process of distortion. On the other hand, the second approach recognized the problem as an inverse problem of a linear Fredholm integral equation of the first kind and proposes suitable solvers to obtain robust estimation of the least-squares solution to the problem. Both approaches have large potential for use with fast imaging modalities such as EPI. The development of these three new acquisition/reconstruction techniques will have an impact on MRI versatility and will certainly help to extend its application to new areas.

## Chapter 2

### PSEUDO-FOURIER IMAGING (PFI)

#### 2.1 Background

In magnetic resonance imaging, spatial localization is achieved using selective excitation or Fourier encoding. These two approaches have rather different, sometimes complementary, characteristics. Selective excitation is realized by applying a band-limited RF pulse in the presence of a slice selection gradient. The spatial resolution attainable with this technique is determined by the slice profile which is a direct function of the slice selection gradient strength and the shape of the RF pulse. In forming an image based on selective excitation (e.g., line scanning), data are acquired using multiple localized excitations each affecting a different region of the imaged field of view. Hence, RF excitations can be interleaved within the same repetition time,  $TR$ , for added efficiency. Moreover, it is possible to update the image locally with few excitations to follow dynamic events occurring in a portion of the field of view. Nevertheless, since each region is excited separately, the signal-to-noise ratio (SNR) is expected to be rather low since no data averaging is implicitly incorporated in this process.

On the other hand, Fourier encoding achieves spatial localization through spatial frequency or phase encoding while the entire volume of interest is excited. By applying varying amounts of Fourier encoding (phase encoding steps) to sufficiently sample the k-space region of interest, the field of view can be reconstructed using a Fourier transform operation. This means that the resolution in this case is in principle unrestricted while keeping an excellent SNR as a direct result of the implicit

averaging in the Fourier transform operation. Since the entire field of view is excited each time, the technique is susceptible to partial saturation as a function of the time interval between excitations. Moreover, the global nature of Fourier encoding lacks the desirable spatial localization property, making it necessary to re-acquire the entire data set to update any portion of the image.

The differences between selective excitation and Fourier encoding are well-known and have been carefully taken into consideration in various applications. For example, in volume imaging, multi-slice imaging takes advantage of the interleaving capability of selective excitation to efficiently collect images with high contrast, while 3-D acquisition is routinely used to obtain high resolution, high signal-to-noise ratio images. In certain applications, the use of either one of these two techniques may not be optimal and a combination of the two methods may in fact be desirable. For example, in time-of-flight magnetic resonance angiography (TOF MRA), the trade-off between signal-to-noise ratio, slice thickness, and contrast makes it suboptimal to use either multi-slice or 3-D acquisition. This motivated the introduction of hybrid techniques to combine features from both techniques. For example, in multiple overlapping thin slab acquisition (MOTSA) [11], the volume of interest is scanned via the acquisition of a number of slabs, each acquired in a 3-D fashion while the different slabs are covered in a multi-slice fashion. In this case, the thin slabs allow for good flow contrast while the 3-D encoding within the slabs provides good spatial resolution and an improved signal-to-noise ratio. In spite of the success of such hybrid techniques, they are limited by their data inefficiency arising from slab overlapping (as much as 50%). Therefore, a technique that allows smooth and flexible combination of the characteristics of selective excitation and Fourier encoding while acquiring the data efficiently can be advantageous.

More recently, the application of MRI has been extended to interventional and dynamic imaging studies. In most of these applications, only a localized region needs to be updated rapidly. Such applications inspired the development of several novel

encoding techniques such as wavelet encoding [12] and SVD-based encoding [13]. Nevertheless, problems in the practical implementation and use for actual clinical applications hindered such techniques from becoming realistic alternatives. Therefore, a spatial encoding technique that allows for fast localized image updating while keeping a simple implementation procedure is desirable for such applications.

In this chapter, the problem of magnetic resonance imaging with flexible excitation profiles acquired at a number of phase encoding steps is considered [8, 9, 10]. In particular, a novel approach for spatial encoding based on acquiring a set of windowed Fourier transform coefficients is developed. This new procedure is shown to be a general technique representing a flexible hybrid of selective excitation and Fourier encoding. In particular, the proposed technique corresponds to the multi-slice technique at one extreme and the Fourier encoding technique at the other. The conditions under which the reconstruction process is stable are described demonstrating that its implementation can be readily achieved on the current MRI systems. Finally, the experimental results of implementing the new technique on a commercial MRI machine are presented.

## 2.2 Theory

### 2.2.1 Decomposition of continuous functions using frames

Consider a continuous function  $f \in L^2(\mathcal{R})$ , where  $L^2(\mathcal{R})$  is the Hilbert space of all functions  $\{f : \mathcal{R} \rightarrow \mathcal{C}\}$ ,  $\mathcal{R}$  is the set of real numbers and  $\mathcal{C}$  is the set of complex numbers. A decomposition of this function can be obtained in terms of a set of basis functions that form a frame for  $L^2(\mathcal{R})$ . An interesting class of frames is the one generated from a single function  $w(x) \in L^2(\mathcal{R})$  (often called the basic window) by translation and modulation in the form  $\{w_{m,n}(x) = \exp(j2\pi\omega_m x) \cdot w(x - x_n)\}$ . Such functions are called the *Weyl-Heisenberg coherent states* and have several applications in quantum physics [14]. When these functions form a frame for  $L^2(\mathcal{R})$ , they can be

used to decompose any function in this functional space with the windowed Fourier transform defined as:

$$WFT(f)(m\omega_o, nx_o) = \int_{-\infty}^{\infty} f(x) \cdot w(x - nx_o) \cdot e^{-j2\pi m\omega_o x} dx \quad (2.1)$$

with  $\omega_o, x_o > 0$  and  $m, n \in \mathcal{Z}$ , the set of integers. In the special case when the coherent states are derived from a Gaussian function, this decomposition is called the *Gabor transform*. In a more general sense, the basic window is a general function that is usually chosen to have a compact support in either the frequency or the time domains. The resultant windowed Fourier transform consists of uniform sampling of the phase-space in what is known as the *Gabor lattice* [15]. This transform has a stable inverse provided that the set of coherent states composed of the basic window and its translations and modulations is complete [14]. In other words, any function  $f(x) \in L^2(\mathcal{R})$  can be reconstructed from its decomposition into Weyl-Heisenberg coherent states in this case.

### 2.2.2 Pseudo-Fourier imaging

Consider now the problem of imaging a 1-D object of signal intensity  $f(x)$ . The signal generated by applying a selective excitation with profile  $W(x)$  centered at  $x_n$  is of the form:

$$r_{selective} = \int_{-\infty}^{\infty} f(x) \cdot W(x - x_n) dx. \quad (2.2)$$

On the other hand, using a hard pulse to uniformly excite the full extent of the object combined with phase encoding at a step  $m$  yields,

$$r_{PE} = \int_{-\infty}^{\infty} f(x) \cdot e^{-j2\pi m\omega_o x} dx. \quad (2.3)$$

Hence, when a selective excitation centered at  $x_n$  is combined with a phase encoding step  $m$ , the resultant signal takes the form:

$$r_{n,m} = \int_{-\infty}^{\infty} f(x) \cdot W(x - x_n) \cdot e^{-j2\pi m\omega_o x} dx. \quad (2.4)$$

In other words, the measured signal is the windowed Fourier transform coefficient corresponding to translation  $n$  and modulation  $m$  of the basic window  $W(x)$ . As a result, by properly choosing the selective excitation profile such that the basic window and its translations and modulations form a frame for  $L^2(\mathcal{R})$ , the object spatial distribution can be reconstructed from these coefficients covering the area of interest in the phase-space. An important observation that should be noted here is that the acquired coefficients are exactly the result of the continuous integration form, not of a discrete approximation.

Hence, to apply the theory, excitation profiles are chosen to be members of the class of functions with frequency spectra  $\hat{W}(\omega - n\omega_o)$ , where  $\hat{W}(\cdot)$  is a basic window and  $n$  takes the values  $1, 2, \dots, N_s$ . In other words, these excitations have spatial profiles given by

$$W(x - x_n) = \hat{W}(\gamma \cdot G \cdot (x - nx_o)), \quad (2.5)$$

which represent repetitions of the same excitation profile with different frequency shifts. It can be shown that Eqn.(2.4) can be expressed in the form of a convolution as:

$$r_m(x_n) = \left( f(x_n) \cdot e^{j2\pi\omega_m \cdot x_n} \right) * W(-x_n). \quad (2.6)$$

Assuming sufficient sampling, the discrete-time Fourier transform (**DTFT**) can be applied to this convolution with respect to  $x_n$  to obtain:

$$R_m(\omega) = \text{DTFT} \{r_m(x_n)\} = F(\omega + \omega_m) \cdot w(-\omega). \quad (2.7)$$

Here  $F(\cdot)$  is the Fourier transform of the signal intensity,  $w(\cdot)$  is the Fourier transform of  $W(\cdot)$  with a constant term dropped out, and  $\omega_m$  is the spatial frequency of the phase encoding frequency step  $m$ . Hence, if the excitation profile  $w(\cdot)$  has a compact support,  $R_m(\omega)$  will essentially be a windowed version of the original k-space of the object. Moreover, it can be seen that the effect of phase encoding  $\omega_m$  in this formula is to shift the focus of this k-space window to scan different parts of the original

$k$ -space. Hence, by properly selecting the number and step of phase encoding such that the overall span of this windowing forms a complete cover of the  $k$ -space interval of interest, it is possible to find an analytical solution to  $F(\omega)$  in the form:

$$F(\omega) = \frac{\sum_{m=1}^M R_m(\omega - \omega_m)}{\sum_{m=1}^M w(-\omega + \omega_m)} \quad (2.8)$$

where  $M$  is the number of phase encoding steps. It should be noted that this solution is valid only for  $\omega$  values within the support of the denominator. This is equivalent to the condition that the basic window and its translations and modulations form a frame to  $L^2(\mathcal{R})$ . Moreover, it is possible to reconstruct a limited  $k$ -space approximation of the object by acquiring a set of windowed Fourier transform coefficients to uniformly cover the phase-space area of interest. Block diagrams of the data acquisition and the reconstruction procedure of PFI are shown in Figs.(2.1) and (2.2).

### 2.2.3 Formal reconstruction stability conditions

It is important here to state and discuss the formal validity conditions under which the above result is true and the reconstruction is stable. First, in Eqn.(2.7), to be able to invoke the discrete-time Fourier transform without encountering aliasing problems, the sampling along  $x$  should satisfy the Nyquist condition. This requirement is clearly determined by the basic window used in the data acquisition, not the extent of the  $k$ -space to be covered in the reconstruction. Given that the received signal is actually a windowed version of the original  $k$ -space, the sampling scheme is dictated by this much narrower spectrum. The second validity condition is that the set of coherent states used in the reconstruction form a frame for  $L^2(\mathcal{R})$ . It can be easily shown that this condition is satisfied when  $w_o \cdot x_o \leq 1$  and the combined support of the basic window and its translations in either the time or the frequency domains forms a complete cover to the real line interval of interest in that domain. This condition can be alternatively visualized from the fact that the reconstruction formula will have

poles when the support of the denominator contains some holes. It should be noted that this condition does not require the support of the different shifts of the basic window to be non-overlapping, i.e., their union being a *tight* cover of the real line  $\mathcal{R}$  corresponding to the spatial frequency. Nevertheless, any degree of overlapping is an inefficiency in the implementation since some parts of the k-space will be covered more than once during the data acquisition. This translates into extra acquisition time since more phase encoding steps will be needed to form the  $k$ -space cover. An efficient implementation should therefore be as close as possible to a tight cover.

### 2.3 Example of Applying PFI Theory

As an example of the above theory, let us now consider the case when a square pulse is used. That is, the basic RF excitation envelope function is given by:

$$w(t) = \begin{cases} 1 & \text{for } |t| \leq \tau/2 \\ 0 & \text{for } |t| > \tau/2 \end{cases} \quad (2.9)$$

where  $\tau$  is the temporal support of the pulse. The spatial profile of this excitation is approximately a Sinc function peaked at the slice location for flip angles below  $30^\circ$ . In this case, the imaging window of PFI in the k-space approximately takes the form of a rectangular window as shown in Fig.(2.3). To assess the validity of this approximation, the slice profiles were computed from the exact solution of the Bloch equations [16] for the above RF excitation at different flip angles and the results are shown in Fig.(2.4). The corresponding imaging window shapes of PFI computed by Fourier transforming the excitation profiles are shown in Fig.(2.5). As can be seen, the approximation of a Sinc excitation profile and a rectangular imaging window asserted above is valid. The spatial frequency span of the excited profile is approximately equal to  $\gamma \cdot G \cdot \tau$  ( $m^{-1}$ ), where  $\gamma$  is the gyromagnetic ratio,  $G$  is the slice selection gradient in use.

Suppose now that it is required to compute a band-limited k-space approximation

of the the imaged object within  $\pm BW_{max}/2$ . To satisfy the reconstruction stability conditions, the support of the excitation  $\tau$  should be related to the number of required phase encoding steps  $M$  as,

$$M \cdot (\gamma \cdot G \cdot \tau) \geq BW_{max} \text{ or } \tau \geq \frac{BW_{max}}{M \cdot \gamma \cdot G} \quad (2.10)$$

The spacing of acquired slices should satisfy the Nyquist criterion for spatial frequency bandwidth  $\gamma \cdot G \cdot \tau$  ( $m^{-1}$ ). Consequently, the required number of slices for an object of length  $L$  is given by:

$$N_s \geq \text{ceiling} \left\{ \frac{L \cdot BW_{max}}{M} \right\} \quad (2.11)$$

The object  $k$ -space is constructed by concatenating segments of it from different excitations as shown in Fig.(2.2). It is worth noting that in the above example the coverage of the  $k$ -space can be made tight. In this case, all parts of the  $k$ -space are acquired only once, making this implementation most efficient.

## 2.4 Implementation under Practical Conditions

In practice, possible gradients and pulse envelope shapes are limited by the slew rates of the available imaging system. This means that the exact theoretical rectangular pulse and gradient shapes considered in the above example or other similar shapes may not be feasible to generate in the exact sense on practical systems. Therefore, the problem of generating the excitation profiles corresponding to these theoretical pulses by using RF pulses and gradients with finite ramp-up and ramp-down periods is considered here.

The Bloch equations of nuclear magnetization in the rotating frame can be put in the following matrix form [16]:

$$\dot{\vec{M}} = \begin{bmatrix} -1/T_2 & \gamma \vec{G} \cdot \vec{x} & -\gamma B_{1,y} \\ -\gamma \vec{G} \cdot \vec{x} & -1/T_2 & \gamma B_{1,x} \\ \gamma B_{1,y} & -\gamma B_{1,x} & -1/T_1 \end{bmatrix} \cdot \vec{M} \quad (2.12)$$

Where  $\vec{M}$  is the magnetization vector in the Cartesian coordinates, and  $\dot{\vec{M}}$  is its time derivative;  $B_{1,x}$  and  $B_{1,y}$  are the two components of the RF pulse;  $\vec{G} \cdot \vec{x}$  is the dot product between the gradient system and the spatial location, and  $T_1$  and  $T_2$  are the spin-lattice and spin-spin relaxation time constants respectively. For most practical applications, the pulse duration is very small compared to the values of  $T_1$  and  $T_2$  of interest. Hence, the above equation can be simplified by neglecting the effect of relaxation. This amounts to the same matrix equation but with zeros on the diagonal elements of the system matrix. In the most general form of this equation, the quantities  $B_{1,x}$ ,  $B_{1,y}$  and  $\vec{G}$  are all time varying. That is, the system is in the form of a bilinear time-varying homogeneous state equation in the form:

$$\dot{\vec{\phi}} = \mathbf{A}(t; \vec{G}, B_{1,x}, B_{1,y}) \cdot \vec{\phi}. \quad (2.13)$$

In a typical spin manipulation problem, it is required to design an excitation in terms of  $\vec{G}$ ,  $B_{1,x}$ , and  $B_{1,y}$  such that the magnetization vector at a given time becomes a given desired vector. Therefore, possible methods to find solutions to the above state equation should be investigated. It can be shown that a sufficient condition for the existence of a unique solution to this system is that all the elements of the matrix  $\mathbf{A}$  should be continuous. This condition is usually satisfied in all magnetic resonance problems of interest. When the gradients and RF pulse shapes are all constant, a direct solution to the problem can be obtained of the form,

$$\vec{x}(t) = e^{\mathbf{A} \cdot (t-\tau)} \cdot \vec{x}(\tau) \quad (2.14)$$

Nevertheless, there is no direct method to obtain this unique solution for any general gradient/RF pulse combination. Also, the available numerical solutions to this system lack the clear perspective into the relationships between the different control parameters that the closed form solution presents. Therefore, it is advantageous to look for closed form solutions for this problem under special conditions that apply to our physical system.

**Lemma 1** *Let  $\mathbf{B}(t, \tau) = \int_{\tau}^t \mathbf{A}(\xi) d\xi$ , then a solution to the general time varying homogeneous system  $\dot{\vec{x}}(t) = \mathbf{A}(t) \cdot \vec{x}(t)$  exists in the form  $\vec{x}(t) = e^{\mathbf{B}(t, \tau)} \vec{x}(\tau)$  if  $\mathbf{A}(t)$  and  $\mathbf{B}(t, \tau)$  commute. That is, whenever  $\mathbf{B}(t, \tau) \cdot \mathbf{A}(t) = \mathbf{A}(t) \cdot \mathbf{B}(t, \tau)$ .*

*Proof:* Differentiating both sides of the proposed solution with respect to  $t$ , it can be shown that,  $\dot{\vec{x}}(t) = e^{\mathbf{B}(t, \tau)} \cdot \mathbf{A}(t) \cdot \vec{x}(\tau)$ . If  $\mathbf{A}(t)$  and  $\mathbf{B}(t, \tau)$  commute, it follows that  $\mathbf{A}(t)$  commutes with any finite-order polynomial of  $\mathbf{B}(t, \tau)$ . Given that the matrix exponential of  $\mathbf{B}(t, \tau)$  can be expressed as a finite-order polynomial of  $\mathbf{B}(t, \tau)$  from Cayley-Hamilton theorem, it commutes with  $\mathbf{A}(t)$ . Invoking this property to rearrange the right-hand side, the equation takes the form,  $\dot{\vec{x}} = \mathbf{A}(t) \cdot e^{\mathbf{B}(t, \tau)} \cdot \vec{x}(\tau) = \mathbf{A}(t) \cdot \vec{x}(t)$ . Therefore, The proposed form is a solution to to the time-varying system equation. From the uniqueness of the solution of this problem, this solution must be the unique solution.

**Theorem 1 (Profile invariance)** *For a magnetic resonance imaging system with general but similar RF pulse envelope and gradient shapes up to a constant multiplier, the resultant excitation profile will be the same for all shapes that integrate to the same value over the pulse duration.*

*Proof:* Since the gradient and RF pulse profiles have the same shape up to a constant, then  $\mathbf{A}(t)$  can be decomposed into the multiplication of a constant matrix  $\mathbf{A}_c$  multiplied by a function of time  $\eta(t)$ . Hence,  $\mathbf{B}(t, \tau)$  can also be decomposed into a similar multiplication of  $\mathbf{A}_c$  and the integral of  $\eta(t)$  over the excitation duration. As a result,  $\mathbf{A}(t)$  and  $\mathbf{B}(t, \tau)$  commute in this case and it follows directly that the solution to the Bloch equations is in the form given by the lemma. Since the state of the magnetization vector is only important at the end of the excitation period, the solution will be the same for all integrable functions with the same integration value over the excitation period.

**Corollary 1** *RF pulse shapes and gradients with similar ramp-up and ramp-down times will produce excitation profiles similar to that of a rectangular pulse with the same area.*

As a consequence of the above theorem, it can be seen that in principle practical gradients and pulse envelopes can indeed be used with PFI without losing the efficiency associated with the ideal rectangular pulse and gradient shapes. It should be noted that the derivation of the above theorem did not involve any assumptions regarding the flip angle. Therefore, it can be applied to large flip angles as well.

## 2.5 Signal-to-Noise Ratio of PFI

Now consider the evaluation of the signal-to-noise ratio (SNR) in the general case of the new technique. The only source of noise is assumed to be the random noise arising from the combined resistance of the imaged subject and the receiver coil. Assuming that  $N_s$  slices at  $M$  phase encoding steps are acquired to reconstruct an  $N$ -point object, these samples will undergo the following steps in the reconstruction process:

1.  $N_s$ -point discrete Fourier transform.
2. Inverse filtering (scaling by constants).
3.  $N$ -point inverse discrete Fourier transform.

These steps can be described mathematically as follows. First, the acquired samples take the form:

$$\hat{r}_m(x_i) = \int_{-\infty}^{\infty} f(x) \cdot W(x - x_i) \cdot e^{j2\pi k_m x} dx + n_{i,m}. \quad (2.15)$$

where  $n_{i,m} \sim \mathcal{N}(0, \sigma^2)$ , an independent and identically distributed additive zero-mean Gaussian white noise with variance  $\sigma^2$ . Hence, the noise contamination of different

samples will be uncorrelated from the properties of the Gaussian distribution. Given the  $N_s$  samples obtained at a phase encoding step  $m$ , an  $N_s$ -point discrete Fourier transform is applied thus yielding,

$$\hat{R}_m(k) = \mathbf{DFT} \{ \hat{r}_m(x_i) \} = F(k + k_m) \cdot w(-k) + \tilde{n}_{k,m}. \quad (2.16)$$

where  $\tilde{n}_{k,m} \sim \mathcal{N}(0, N_s \sigma^2)$ . Since the discrete Fourier transform is an orthogonal transformation,  $\tilde{n}_{k,m}$  values are uncorrelated.

The next step in the reconstruction process is the possible use of inverse filtering to restore general imaging window shapes to the ideal rectangular shape. This process can be expressed as:

$$\bar{R}_m(k) = \hat{R}_m(k) \cdot g(k) = F(k + k_m) \cdot w(-k) \cdot g(-k) + \bar{n}_{k,m}. \quad (2.17)$$

Here,

$$g(k) \cdot w(k) = \begin{cases} 1 & \text{for } k \in \text{Support}\{w(k)\} \\ 0 & \text{for } \text{otherwise.} \end{cases} \quad (2.18)$$

Now the noise term becomes  $\bar{n}_{k,m} \sim \mathcal{N}(0, N_s \sigma^2 |g(k)|^2)$ . In the ideal case of a rectangular profile,  $g(k) = 1$  and  $\bar{n}_{k,m} \sim \mathcal{N}(0, N_s \sigma^2)$ . Since this step does not involve any mixing of k-space samples, the noise within each of these samples continue to be uncorrelated after inverse filtering.

In the final step, the full k-space is composed by concatenating these pieces and an  $N$ -point inverse discrete Fourier transformation is performed to obtain the final image. That is,

$$\bar{f}(x) = \mathbf{IDFT} \{ \bar{F}(k) \} = \mathbf{IDFT} \left\{ \sum_{m=1}^M \bar{R}_m(k - k_m) \right\} = f(x) + n'_x \quad (2.19)$$

where  $M \cdot N_s = N$ , the total number of points. Since the noise components in the k-space samples are uncorrelated, the noise in the final image is given as  $n'_x \sim \mathcal{N}(0, \sigma^2 \sum_{k=1}^{N_s} |g(k)|^2 / (M \cdot N_s))$ . It can be seen that the noise power is independent of the location  $x$  and therefore will be uniform in the obtained image. It should be noted

the noise in different pixels will be correlated when an inverse filter  $g(k) \neq 1$  is applied. Two special cases of interest should be pointed out from the above expression. In the first case of volume imaging where  $N_s = 1$  and  $M = N$ , the noise variance is  $\sigma^2/N$ . On the other hand, for the second special case of selective excitation,  $N_s = N$  and  $M = 1$ , and therefore, the noise variance is simply  $\sigma^2$ . These two values mark the two ends of the range of possible values for the noise variance. Other values within this range can be achieved with the choice of  $N_s$  and  $M$  of the pseudo-Fourier imaging.

Another important ratio that can be computed for pseudo-Fourier imaging is the *efficiency figure of merit* defined as [11],

$$\eta = \frac{SNR}{\sqrt{time}}. \quad (2.20)$$

This ratio is used mainly to compare different imaging techniques having different SNR values and acquisition times. For example, when selective excitation is compared to Fourier imaging, the ratio takes the form,

$$\frac{\eta_{Fourier}}{\eta_{Selective}} = \sqrt{N}, \quad (2.21)$$

where imaging times are assumed to be the same for both techniques. Similarly, the comparisons between pseudo-Fourier imaging and these two techniques can be computed as:

$$\frac{\eta_{PFI}}{\eta_{Selective}} = \sqrt{\frac{N}{\sum_{k=1}^{N_s} |g(k)|^2}}, \quad (2.22)$$

and,

$$\frac{\eta_{PFI}}{\eta_{Fourier}} = \sqrt{\frac{1}{\sum_{k=1}^{N_s} |g(k)|^2}}. \quad (2.23)$$

It should be noted that the efficiency figure of merit does not take into account slice interleaving. Therefore, the actual efficiency for selective excitation and pseudo-Fourier imaging may be higher in practice.

## 2.6 Potential Applications of PFI

As a general encoding method, PFI can be applied in a number of areas in MRI. In the following, three possible applications are discussed in some detail as examples.

### 2.6.1 Volume imaging

Currently, volume imaging is performed through either the acquisition of multiple thin slices or phase encoding in the slice direction. Multiple slice acquisition has the advantage of slice interleaving which allows the use of suitable  $TR$  values for proper contrast. On the other hand, multi-slice imaging suffers from slice profile limitations as well as low SNR. With PFI, interleaving can be used to excite the slabs while keeping Fourier encoding which provides better resolution and SNR. Moreover, the trade-off between these characteristics can be controlled flexibly through the selection of the number of slices and phase encoding steps.

### 2.6.2 Magnetic resonance angiography (MRA)

In MRA based on time-of-flight contrast, problems are often encountered in association with both 2-D (multi-slice) and 3-D (thick volume) approaches. The 2-D acquisition provides excellent flow contrast but has a limited slice resolution and SNR. On the other hand, while the SNR and slice thickness are not problematic in 3-D acquisition, saturation of the moving spins in the blood from repeated excitations degrades flow contrast. Hence, a hybrid between the two techniques can be advantageous. PFI provides a natural vehicle for such a hybrid technique. It should be noted here that PFI is different from the MOTSA (multiple overlapped thin-slab acquisition) technique which is based on conventional Fourier imaging [11]. Moreover, MOTSA suffers from a high degree of redundancy in data acquisition as a result of overlapping between consecutive slabs. In contrast, Pseudo-Fourier imaging can be implemented without any redundancy in the data acquisition process.

### 2.6.3 Dynamic imaging

Many authors have suggested different methods of reduced data acquisition, either in the k-space or the spatial domain [17, 18]. The objective of these methods is to obtain fast updates of the dynamic information within a given image. Wavelet encoding can be potentially used to limit the dynamic information in both domains [12]. However, its implementation is cumbersome, if not impractical, for many reasons [19, 20]. From the above description of the pseudo-Fourier technique, it can be seen that PFI readily permits reduced data acquisition in both domains. For example, to reduce the updated k-space data, one can acquire only the low phase encoding steps. On the other hand, when the dynamic event is known *a priori* to be localized to within only a small portion of the image, one can limit the number of updated slices. In this case, the pseudo-Fourier technique will only acquire those selective excitations that are localized around the dynamic object, providing a better temporal resolution for the dynamic imaging sequence.

## 2.7 Experimental Verification of PFI

To experimentally demonstrate the new technique, PFI was implemented on a Siemens Magnetom Vision MR scanner (Siemens Medical Systems, Iselin, NJ). Volume data were acquired for a standard resolution phantom in which the pseudo-Fourier technique was used to reconstruct the slice direction. The data were obtained using a FLASH sequence [22] with a flip angle  $\alpha$  of  $25^\circ$ , a  $TR$  of 15 ms, and a  $TE$  of 6 ms. A  $512 \mu s$  square excitation pulse profile was used in the presence of a 2.9 mT/m gradient for selective excitation. The number of acquired slices ( $N_s$ ) was 19 and these slices were 16 mm apart. In addition to the in-plane encoding ( $25.6cm \times 25.6cm$  FOV and  $256 \times 96$  matrix), the number of phase encoding steps along the slice direction for the pseudo-Fourier technique ( $M$ ) was 16. The data were then used to reconstruct a total of 304 slices 1-mm thick using Eqn.(2.8). Reformatted images along the PFI and fre-

quency encoding directions from the volume data reconstructed using PFI are shown in Fig.(2.6) along with a zoomed version to show the 1-mm bars obtained with both PFI and conventional 2-D Fourier encoding for comparison in Fig.(2.7). The pseudo-Fourier technique was used in the horizontal direction. The images exhibit 1-mm resolution in the PFI direction, in agreement with what the pseudo-Fourier theory predicted. The comparison between the two images indicates that the new technique provides a similar resolution as the conventional Fourier encoding. Nevertheless, the flexibility of the new technique in combining desirable features of multi-slice and volume imaging is a definite plus for many applications.

Examples of using PFI in MRA are shown in Figs.(2.8) and (2.9) for window sizes of 8 mm and 16 mm respectively. A volume of  $200 \times 200 \times 128 \text{ cm}^3$  was covered by a  $256 \times 192 \times 128$  matrix with PFI in the third dimension. The total acquisition time in both sequences was 12 minutes. As can be seen, the smaller window provides better detail while the larger window has a better SNR. The images also exhibited good vessel contrast despite the fact that the sequences are not yet optimized.

To demonstrate the potential of PFI for dynamic imaging applications, both spatial and k-space localization are utilized in this example. Images were reconstructed with various amounts of data omitted to simulate reduced data acquisition. In Fig.(2.10), different portions of the image were reconstructed using fewer phase encoding steps. This was done by using only five encoding steps for the slices covering these regions while the full data for the other slices was used in the reconstruction. As can be seen, the resultant image presents a localized low-pass filtered portion in the corresponding slice locations. In the case of one slice, the image portions corresponding to this slice in the volume of interest can be updated at a rate of 75 ms for each image in the volume.

## 2.8 Discussion

To illustrate the hybrid nature of PFI, two extreme cases of the technique can be considered. In the first, when the excitation profile covers the entire volume, the technique becomes equivalent to the conventional volume imaging. In this case, the number of points in the PFI reconstruction is equal to the number of phase encoding steps ( $N = M$ ) with a single slice ( $N_s = 1$ ). This represents the approach in volume imaging where the  $k$ -space is sampled by phase encoding. On the other extreme, when the excitation profile is very thin, PFI corresponds to the conventional multi-slice imaging. This is the case when the number of points in the PFI reconstruction is equal to the number of slices ( $N = N_s$ ) with no phase encoding applied ( $M = 1$ ). Therefore, by selecting the parameter  $M$ , one can basically move anywhere between these two extreme cases to obtain a tailored hybrid technique for the specific application at hand.

From the Fourier uncertainty principle, any function and its Fourier transform cannot both have compact support. Applying this principle to the compact windowed  $k$ -space acquisitions of PFI, it can be shown that the spatial domain representation of each of these windows is infinite in extension in principle. As a result, to perform the discrete-time Fourier transform operation in Eqn.(2.7) in the exact sense, an infinite number of samples is required. In practice, a truncated sampling is obtained. In our implementation, due to the implicit approximation in using the truncated sampling in the discrete Fourier transform, the resultant  $k$ -space is basically the convolution of the Fourier transform of the sampling window function with the true  $k$ -space, corresponding to blurring in the computed  $k$ -space. This blurring is usually negligible since the  $k$ -space is often smooth.

As an unconventional spatial encoding technique, an interesting comparison arises between PFI and other experimental techniques such as SVD or wavelet encoding. The SVD technique is based on the availability of *a priori* knowledge regarding the

object to be imaged [13]. Using this knowledge, it may be possible to determine a reduced set of acquisitions to obtain images that are closest to the original in a least-squares sense. One potential problem of the SVD approach is that in many cases the singular value decomposition of the object yields a set of singular values that are very close making the reduced representation impossible. The main problem for the SVD technique arises from the availability and applicability of the needed *a priori* information [21]. This is especially problematic in applications such as dynamic imaging where the image content may undergo drastic changes in a dynamic event. In other words, the singular values of the dynamic information may not be similar to those of the static images known *a priori*. The pseudo-Fourier technique does not assume such *a priori* description of the imaged object.

Now consider the comparison between PFI and the wavelet encoding technique [12]. The motivation of implementing wavelet decomposition in most of its original applications is to have basis functions maintaining localization properties in both the spatial and k-space domains. This translates into less ringing artifacts in both domains while retaining the completeness and invertibility of the transform. The main difference between the wavelet encoding and PFI is that the space-frequency plane in the wavelet encoding is sampled non-uniformly, unlike with PFI where it is uniformly sampled on a Gabor grid. Both wavelet encoding and pseudo-Fourier techniques are based on reconstructing the object through obtaining windowed versions of the object spectrum. Nevertheless, the windows used in wavelet encoding are usually overlapping and of different widths, whereas the windows in PFI are identical. This makes the implementation of PFI much easier than wavelet encoding.

The computational complexity of PFI is estimated to be  $O(N \log N)$  flops for reconstructing an  $N$ -point line. This estimate is independent of the window shape used (or equivalently the basis functions used) with a possible increase of less than 10% in acquisition time in the case of overlapping windows (non-orthogonal basis functions). This presents a significant reduction of the reconstruction complexity over encoding

techniques using Hadmard or wavelet basis functions which have reconstruction algorithms with a complexity of  $O(N^2)$  flops. This reduction in the computational complexity amounts to several orders of magnitude reduction in the reconstruction time with PFI. The main reason for this reduction is the special structure of the PFI basis functions which allows the use of FFT.

The performance of PFI in the presence of  $B_0$  inhomogeneity can also be easily understood. Since the slice profile is the same for all excitations, the associated gradient strength is uniform all along the experiment time. Given that the  $B_0$  inhomogeneity effect depends mainly on the gradient strength and that the reconstruction process involves only Fourier transformations, the effect of magnetic field inhomogeneity in the direction encoded by PFI will be very similar to that encountered with Fourier imaging. The stronger the field gradient, the less the image distortion resulting from the magnetic field inhomogeneity becomes.

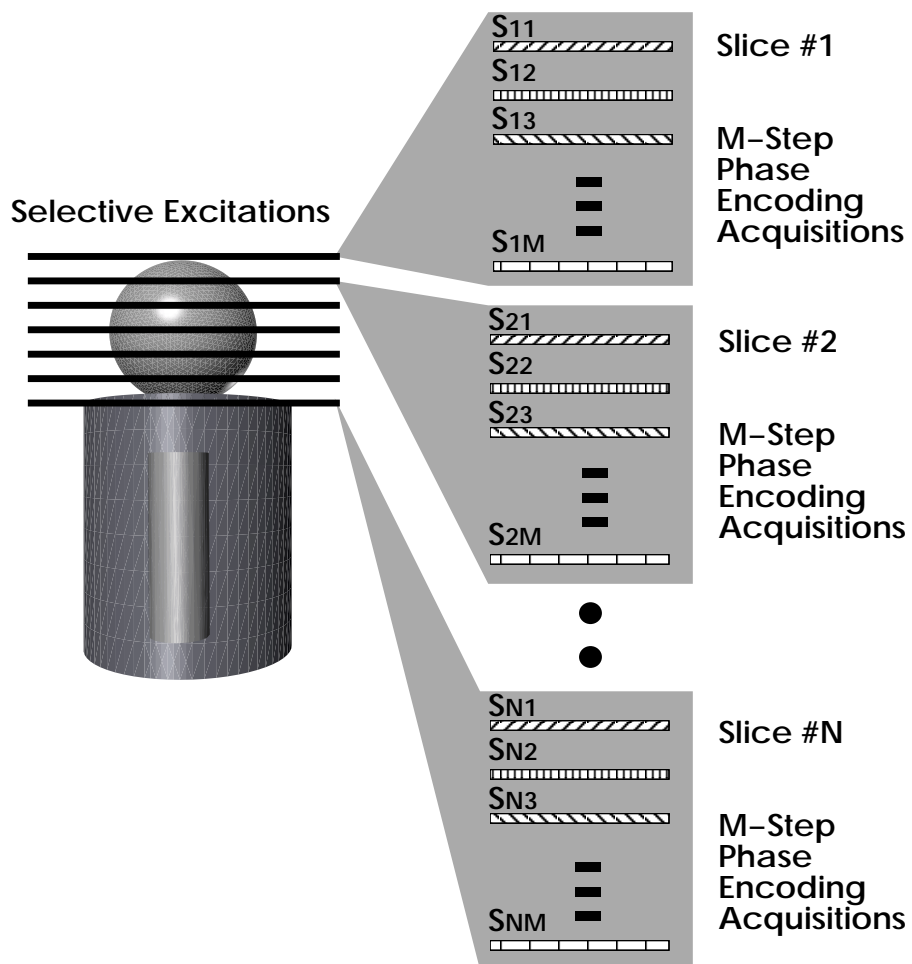


Figure 2.1: Data acquisition in PFI.

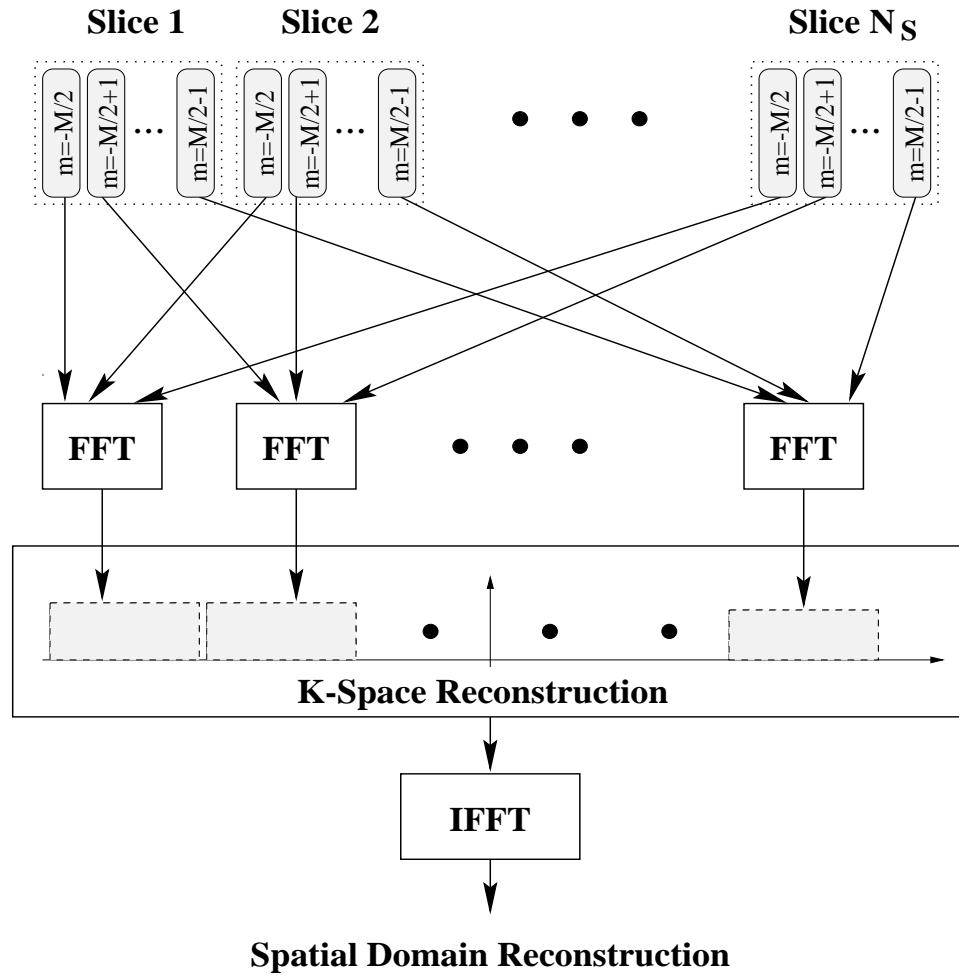


Figure 2.2: Block diagram of the reconstruction procedure in PFI. Starting from the  $N_s$  slices acquired at  $M$  phase encoding steps, the reconstruction procedure computes an  $N$ -point spatial distribution for the imaged object.

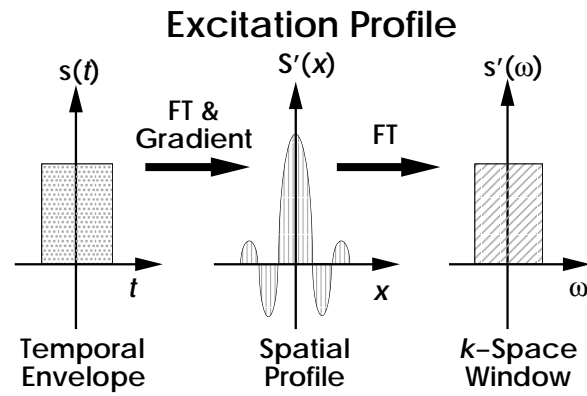


Figure 2.3: RF excitation related to the imaging window of PFI. A rectangular excitation pulse yields a Sinc profile in the spatial domain which in turn provides a rectangular window of the k-space of the imaged object.

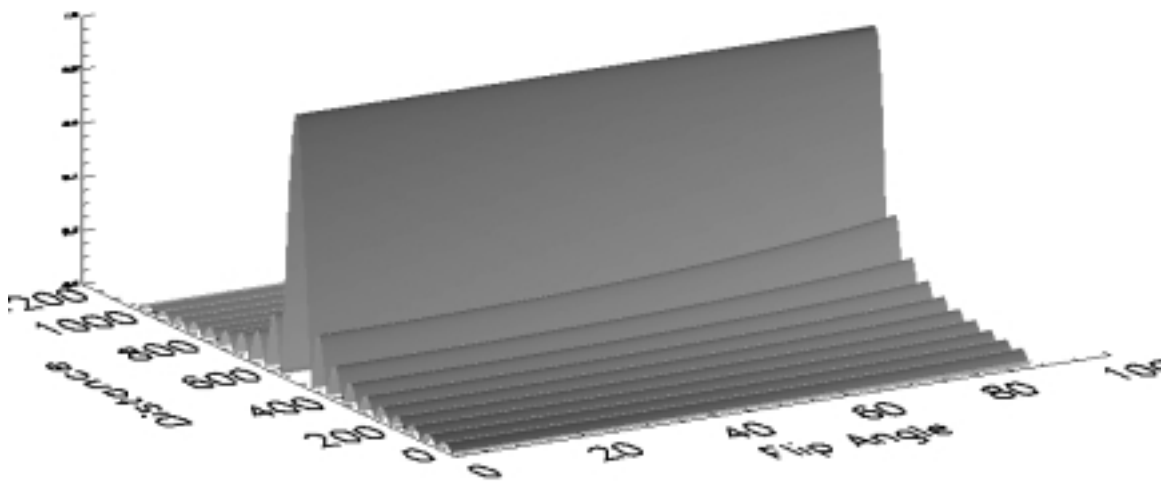


Figure 2.4: PFI excitation profiles using a rectangular RF pulse at different flip angles. The deviation from the ideal Sinc profile is evident at high flip angles.

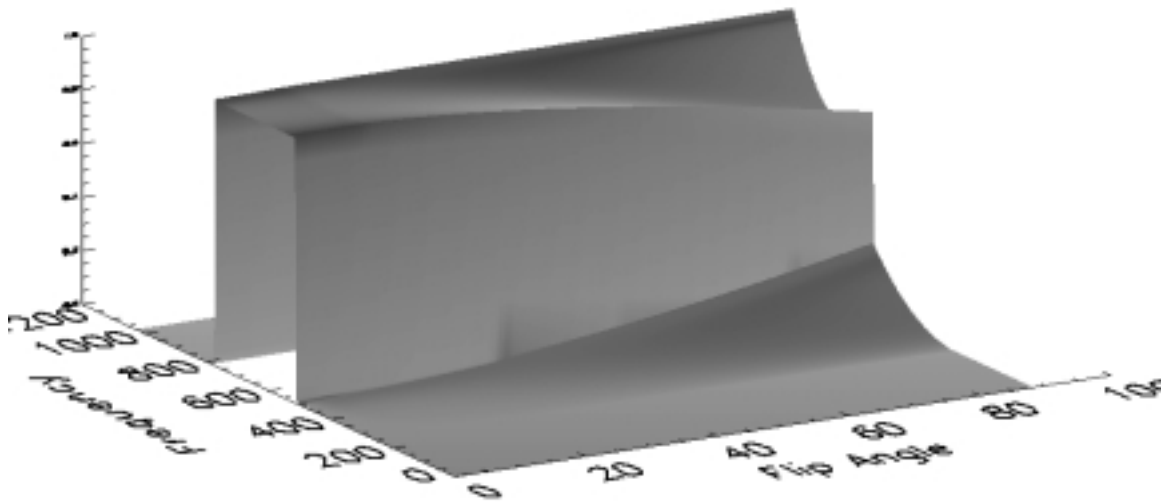


Figure 2.5: PFI Imaging windows using a rectangular RF pulse at different flip angles. The deviation from the ideal Sinc profile is evident at high flip angles.

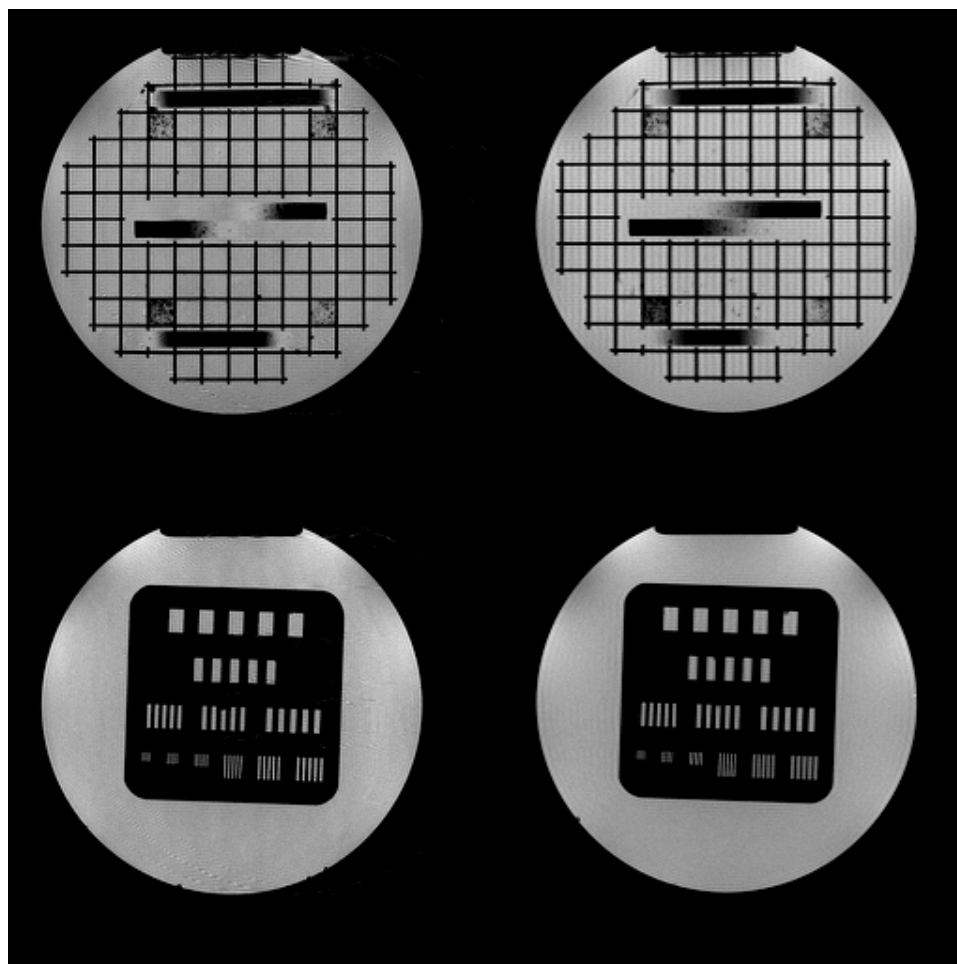


Figure 2.6: Experimental result of imaging a resolution phantom with PFI. The PFI images (left) exhibit a similar resolution to the comparison images obtained with Fourier imaging (right) in the PFI direction (horizontal).

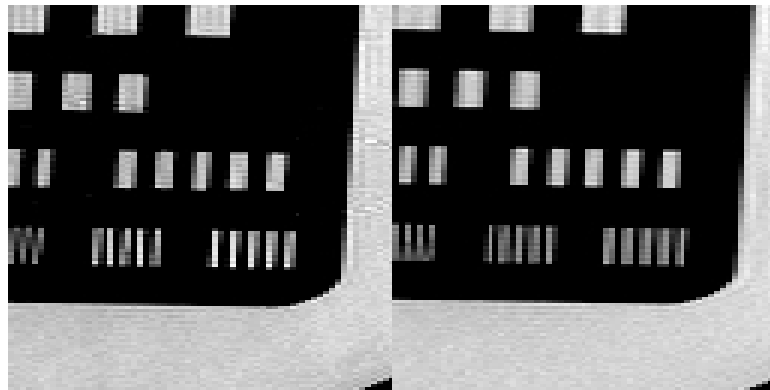


Figure 2.7: Zoomed version of Fig.(2.6) to show the 1 mm resolution lines.

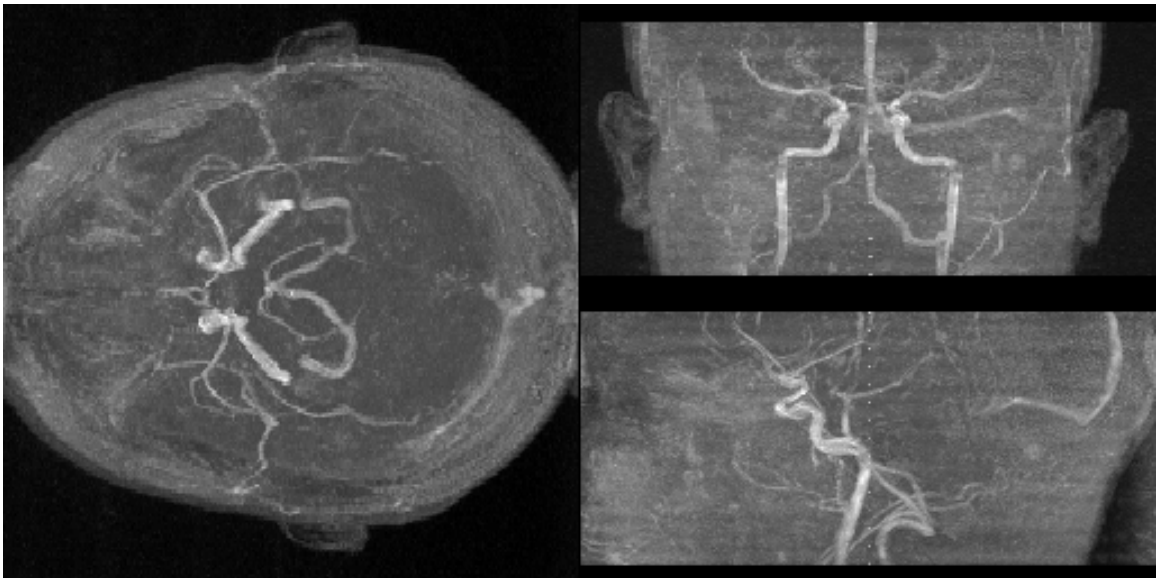


Figure 2.8: MIP images obtained with PFI with window size of 8 mm. PFI was used to encode the axial direction.

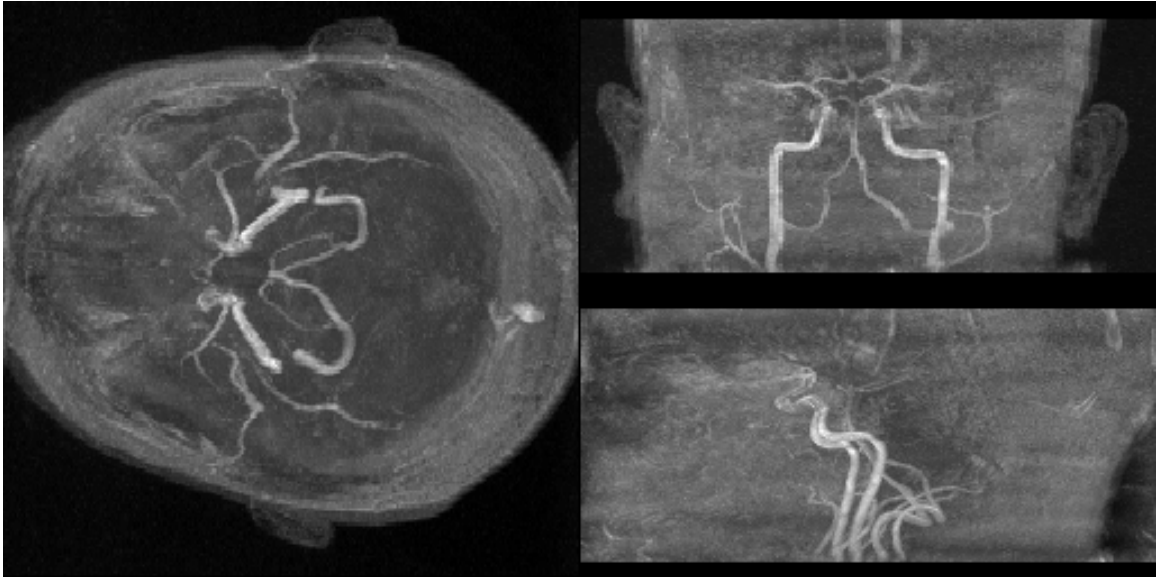


Figure 2.9: MIP images obtained with PFI with window size of 16 mm. The images look less noisy but detail visualization is not as good as Fig.(2.8).

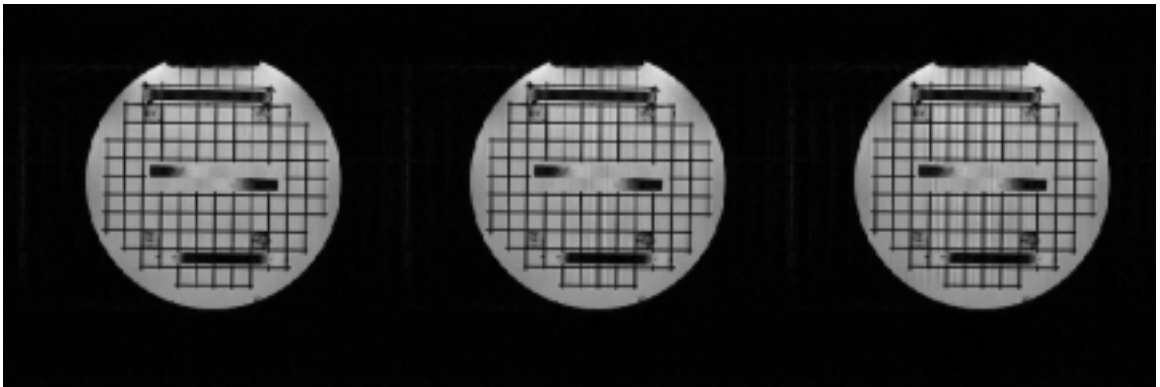


Figure 2.10: Example of spatial/k-space localization capabilities of PFI for potential use in dynamic imaging: usual PFI reconstruction (left), reduced k-space acquisition in 1 PFI slice (middle), and reduced k-space acquisition in 3 PFI slices (right).

## Chapter 3

# SIMULATED PHASE EVOLUTION REWINDING (SPHERE)

### 3.1 Background

In magnetic resonance imaging, linear magnetic field gradients are applied to achieve spatial encoding. Such an encoding scheme can be sensitive to static field ( $B_0$ ) inhomogeneity because of its similar effect to that of the applied gradients. Consequently, image degradation often arises when significant  $B_0$  inhomogeneity exists. In sequences where the traversal of the k-space in a given direction is linearly related to the time within the sampling window (e.g., single-shot EPI), image degradation appears as local displacement and intensity modulation. For more complicated sequences such as segmented EPI with centric reordering and spiral EPI, the relationship between the k-space variable and the time within the acquisition window is nonlinear. In this case, the  $B_0$  inhomogeneity effect generally leads to a position-dependent local blurring that degrades the spatial resolution achievable with these sequences. In such clinical applications as stereotactic localization and radiotherapy treatment planning, geometric accuracy is essential and  $B_0$  inhomogeneity-induced distortions in MRI cannot be tolerated [4, 5]. Also, in functional MRI, severe distortions in EPI images make anatomic referencing using images obtained with other sequences difficult. Therefore, it is necessary to correct for such distortions in order to expand the use of MRI in these fields in addition to improving the obtainable image quality in general.

Many authors have suggested and implemented different methods to overcome the problem of inhomogeneity-induced image distortions. These techniques can be

generally classified into two main categories according to the way the inhomogeneity inverse operator is designed. The first category includes the methods based on estimating an approximate inhomogeneity inverse operator through field mapping. Field maps can be used to correct shift distortions in the spatial domain by computing the corresponding pixel shifts and unwarp the image [7, 28, 29, 31]. Alternatively, they can also be used to modify the k-space while computing the spatial domain as with the conjugate phase method [30, 37]. Other techniques also used the computed field maps to derive analytical models for the distorted space-frequency mapping in different simplified forms that allow for fast correction [26, 39, 40]. Finally, there was an attempt to solve the inhomogeneity problem algebraically by inverting a very large approximate matrix operator to solve for a vector composed of the whole image [41].

The second category of correction techniques includes the methods that do not require field mapping. The most important of such methods is the one that uses two images acquired with reversed gradients [32]. Since the inhomogeneity effect does not change between the two images, the direction of the resultant distortions will be different between the two. Hence, by comparing the two, it is possible to derive a distortion-free image. It should be noted, however, that this method corrects only shift distortions.

In this chapter, a general approach for reducing  $B_0$  inhomogeneity effects is proposed [23, 24]. Observing that image degradation due to  $B_0$  inhomogeneity arises from the phase accrual in the long data acquisition window, the present approach introduces the concept of phase rewinding by numerically generating a corrected k-space data set based on an initial estimate of the image and a corresponding field map. After phase rewinding, the k-space data set is Fourier transformed to obtain the corrected image. This approach is termed Simulated PHase Evolution REwinding (SPHERE). In the simplest case, SPHERE resembles the Fourier space shift technique introduced by Weisskoff and Davis [31]. However, since SPHERE is conceptualized based on the data acquisition process, it is more general and can be applied to other data

acquisition schemes. With proper approximations, the computational complexity is comparable to existing techniques [37, 38, 39]. This chapter describes the technical details of SPHERE and provides a rigorous and complete theoretical analysis of the technique. Finally, the technique is experimentally demonstrated using data obtained with different scanning sequences.

## 3.2 Theory

Consider imaging an object  $f(\vec{r})$  in the presence of magnetic field inhomogeneity  $\Delta B(\vec{r})$  which corresponds to an off-resonance frequency  $\Delta\nu(\vec{r}) = \gamma \cdot \Delta B(\vec{r})$ . Ignoring relaxation effects, gradient imperfections, and T2\* decay, the signal acquired from this object in the presence of Fourier encoding takes the form:

$$D(\vec{k}) = \int f(\vec{r}) \cdot e^{j2\pi\Delta\nu(\vec{r})t(\vec{k}) - j2\pi\vec{k}\cdot\vec{r}} d\vec{r} \quad (3.1)$$

where  $D(\vec{k})$  is the signal sampled with Fourier encoding  $\vec{k}$ , and  $t(\vec{k})$  is the time at which  $D(\vec{k})$  is sampled. When the data acquisition window is small relative to the off-resonance frequency, i.e.  $(\max(t(\vec{k})) - \min(\vec{k})) \cdot |\Delta\nu(\vec{r})| \ll 1$ , the inhomogeneity term in Eqn.(3.1) is essentially independent of  $\vec{k}$  and leads to a  $TE$ -dependent phase factor in the estimate of  $f(\vec{r})$  that is eliminated in the magnitude image. For sequences such as EPI and spiral where the data acquisition window is very wide (e.g., 100 ms) and the inhomogeneity term is  $\vec{k}$ -dependent, severe image distortion and blurring can occur.

To remove the inhomogeneity induced effects in the acquired data, it is necessary to undo the phase effect in Eqn.(3.1), which depends on both  $\vec{r}$ , and  $\vec{k}$ . An exact solution to this problem can be achieved only if  $f(\vec{r})$  and  $\Delta\nu(\vec{r})$  are known. In this work, an approximate solution is derived based on this principle. Without the exact knowledge of  $f(\vec{r})$ , an initial estimate from the acquired data,  $\hat{f}(\vec{r})$ , is used. An estimate of the off-resonance function,  $\Delta\hat{\nu}(\vec{r})$ , is derived from the phase-difference of

images acquired at two different echo times using the sequence under consideration. With this approach,  $\Delta\hat{\nu}(\vec{r})$  is affected by the  $B_0$  inhomogeneity but exactly registered with the initial estimate of  $\hat{f}(\vec{r})$ . Mathematically, the rewinding process can be described as

$$\hat{D}(\vec{k}) = \int \hat{f}(\vec{r}) \cdot e^{-j2\pi\Delta\hat{\nu}(\vec{r})t(\vec{k}) - j2\pi\vec{k}\cdot\vec{r}} d\vec{r} \quad (3.2)$$

The rewinding process generates a simulated k-space data set,  $\hat{D}(\vec{k})$ , which is subsequently used to reconstruct the final image. An intuitive interpretation of the correction technique is that it essentially redistributes  $\hat{f}(\vec{r})$  according to the off-resonance frequency map and the characteristics of the imaging process. A block diagram of the correction process is shown in Fig.(3.1).

The effect of the phase-rewinding process described in Eqn.(3.2) can be understood with the following analysis in which a 1-D object is considered without loss of generality. The initial estimate,  $\hat{f}(x)$ , can be expressed as:

$$\hat{f}(x) = \int_{-\infty}^{\infty} e^{j2\pi kx} \int_{-\infty}^{\infty} f(\alpha) \cdot e^{j2\pi\Delta\nu(\alpha)t(k) - j2\pi k\alpha} d\alpha dk \quad (3.3)$$

which can be expressed as the inner product of  $f(x)$  and a *distortion kernel*,  $\Psi$ , such that,

$$\hat{f}(x) = \int_{-\infty}^{\infty} f(\alpha) \cdot \Psi(\alpha, x) d\alpha = \langle f, \Psi \rangle \quad (3.4)$$

with

$$\Psi(\alpha, x) = \int_{-\infty}^{\infty} e^{j2\pi\Delta\nu(\alpha)t(k)} \cdot e^{-j2\pi k(\alpha-x)} dk \quad (3.5)$$

being the distortion kernel. Note that Eqn.(3.4) is not a simple convolution since  $\Psi(\alpha, x)$  is not shift invariant. If the inhomogeneity function is zero, the distortion kernel is a  $\delta$ -function (the identity kernel). Otherwise, it is sparse in general and could be ill-conditioned. It is straightforward to show that the correction method described above applies a *correction kernel*,

$$\Gamma(\alpha, x) = \int_{-\infty}^{\infty} e^{-j2\pi\Delta\hat{\nu}(\alpha)t(k)} e^{-j2\pi k(\alpha-x)} dk \quad (3.6)$$

to  $\hat{f}(x)$  such that

$$\hat{f}_c(x) = \int_{-\infty}^{\infty} \hat{f}(\alpha) \cdot \Gamma(\alpha, x) d\alpha \quad (3.7)$$

Combining Eqns.(3.4) and (3.7),

$$\hat{f}_c(x) = \int_{-\infty}^{\infty} f(\xi) \cdot \Phi(\xi, x) d\xi \quad (3.8)$$

where

$$\Phi(\xi, x) = \langle \Gamma, \Psi \rangle = \int_{-\infty}^{\infty} \Gamma(\alpha, x) \cdot \Psi(\xi, \alpha) d\alpha \quad (3.9)$$

Eqns.(3.7) and (3.8) indicate that the effect of SPHERE is to process  $\hat{f}(x)$  with a restoration kernel such that the resultant estimate,  $\hat{f}_c(x)$ , corresponds to the original function integrated with a compound kernel,  $\Phi$ .

The effectiveness of the correction process (in terms of the residual error) is fully described by the compound kernel. For complete restoration, the compound kernel should be the identity kernel. Before a theoretical analysis is provided, the above formalism is illustrated with an example. In this example, discrete versions of the three kernels described above were computed for a practical case. A 1-D line along the phase-encoding direction is considered for a segmented EPI sequence with centric re-ordering. The distortion kernel is calculated using the field map derived from FLASH images obtained at two echo times (Fig.(3.2a)) and the correction kernel is calculated based on the field map derived from two segmented EPI images at different echo times (Fig.(3.2b)). The overall compound kernel is the result of the matrix product of the two. The result of the calculation is illustrated in panel (c) of Fig.(3.2). In this representation an identity kernel should be a diagonal line and any deviation from the diagonal indicates a deviation from the identity kernel. In particular, the splitting in the distortion kernel (panel a) shows the dispersion effect of the large field inhomogeneity in that region. In the correction kernel (panel b), a similar splitting in the same region compensates that in the distortion kernel. Consequently, the compound kernel (panel c) is very close to the identity kernel except at a small region where the

inhomogeneity effect is very severe and significantly violates the working conditions for the technique described below. This practical example demonstrates the ability of SPHERE to reduce the inhomogeneity distortions under realistic conditions. The formal description of the performance of SPHERE and these conditions are presented in the following section.

### 3.3 Performance Analysis of SPHERE

In the following, a theoretical analysis of SPHERE is presented. Since the compound kernel is determined by  $t(\vec{k})$  which is sequence-dependent, two special cases will be considered first to illustrate the idea before the general case is considered.

#### 3.3.1 Special case 1: Blipped-EPI

In this case, the trajectory function  $t(k)$  takes the form of a linear one-dimensional function of  $k$ , i.e.  $t(k) = a \cdot k$ , where  $a$  is a constant. The distortion and correction kernels take the following forms:

$$\Psi(\alpha, x) = \delta(x - \alpha - a\Delta\nu(\alpha)) \quad (3.10)$$

and

$$\Gamma(\alpha, x) = \delta(x - \alpha + a\Delta\hat{\nu}(\alpha)) \quad (3.11)$$

It follows that the compound kernel is:

$$\Phi(\alpha, x) = \delta(x - \alpha - a\Delta\nu(\alpha) + a\Delta\hat{\nu}(\alpha + a\Delta\nu(\alpha))) \quad (3.12)$$

When the distortion is in the form of a simple shift or when signals arising from different regions in the original image do not overlap, the terms containing the off-resonance effect in Eqn.(3.12) cancel and the compound kernel becomes the identity kernel, leading to complete restoration. In practice, this condition may be violated in certain areas such as tissue boundaries. Only a partial correction can be achieved in these locations.

### 3.3.2 Special case 2: Segmented-EPI with centric-reordering

This case is more complex since the overlap of the distortion shifts from neighboring pixels cannot be avoided in general. The 1-D formalism is still valid here since the field inhomogeneity mainly affects the phase-encoding direction. The form of  $t(k)$  in this case is a linear function of the absolute value of  $k$  rather than  $k$  itself as in the first case. The inhomogeneity phase function can be expressed as the sum of two linear terms over two non-overlapping windows of the  $k$ -space. That is,

$$e^{j2\pi\Delta\nu(x)\cdot a|k|} = e^{j2\pi\Delta\nu(x)\cdot ak} \cdot u(k) + e^{-j2\pi\Delta\nu(x)\cdot ak} \cdot u(-k) \quad (3.13)$$

where  $u(k)$  is a unit-step function and  $a$  is a constant. The corresponding distortion and correction kernels are:

$$\Psi(\alpha, x) = U_+(x - \alpha - a\Delta\nu(\alpha)) + U_-(x - \alpha + a\Delta\nu(\alpha)) \quad (3.14)$$

and

$$\Gamma(\alpha, x) = U_+(x - \alpha + a\Delta\hat{\nu}(\alpha)) + U_-(x - \alpha - a\Delta\hat{\nu}(\alpha)) \quad (3.15)$$

where  $U_+(\alpha)$  and  $U_-(\alpha)$  are the Fourier transforms of  $u(k)$  and  $u(-k)$ , respectively. It follows from (13) and (14) that the compound kernel is a sum of four terms, each corresponding to a possible combination of  $U_+(\cdot)$  and  $U_-(\cdot)$  in the two kernels. Specifically,

$$\begin{aligned} \Phi(\alpha, x) = & \int_{-\infty}^{\infty} U_+(\beta - \alpha - a\Delta\nu(\alpha)) \cdot U_+(x - \beta + a\Delta\hat{\nu}(\beta)) d\beta \\ & + \int_{-\infty}^{\infty} U_-(\beta - \alpha + a\Delta\nu(\alpha)) \cdot U_-(x - \beta - a\Delta\hat{\nu}(\beta)) d\beta \\ & + \int_{-\infty}^{\infty} U_+(\beta - \alpha - a\Delta\nu(\alpha)) \cdot U_-(x - \beta - a\Delta\hat{\nu}(\beta)) d\beta \\ & + \int_{-\infty}^{\infty} U_-(\beta - \alpha + a\Delta\nu(\alpha)) \cdot U_+(x - \beta + a\Delta\hat{\nu}(\beta)) d\beta \end{aligned} \quad (3.16)$$

Under the condition that the distortion is non-overlapping in space (hereafter referred to as the non-overlapping condition),  $\Delta\hat{\nu}(\beta)$  is constant and equal to  $\Delta\nu(\alpha)$  within

the non-zero portions of the integrands of the compound kernel. Hence, each of these four terms is equivalent to an inner product of shifted versions of  $U_+(\cdot)$  and  $U_-(\cdot)$ . Given that shifted versions of  $U_+(\cdot)$  and  $U_-(\cdot)$  correspond to  $u(k)$  and  $u(-k)$  multiplied by linear phase functions in the k-space respectively, the terms containing the multiplication of  $U_+(\cdot)$  with  $U_-(\cdot)$  vanish because their corresponding k-space functions are orthogonal. For example, the third term in Eqn.(3.15) becomes,

$$\begin{aligned} \int_{-\infty}^{\infty} U_+(\beta - \alpha - a\Delta\nu(\alpha)) \cdot U_-(x - \beta - a\Delta\nu(\beta)) d\beta = \\ \frac{1}{2\pi} \int_{-\infty}^{\infty} u(k)u(-k)e^{-j2\pi k(-\alpha-2\pi a\Delta\nu(\alpha))} \cdot e^{-j2\pi k(x-2\pi a\Delta\nu(\alpha))} dk = 0 \end{aligned} \quad (3.17)$$

This orthogonality can be deduced from the fact that the multiplication of  $u(k)$  and  $u(-k)$  is zero everywhere regardless of the presence of linear phase multipliers and by invoking Parseval's identity of the Fourier transform [47]. The remaining two terms take the form of the autocorrelations of  $U_+(x)$  and  $U_-(x)$  respectively, resulting in  $u(k)$  and  $u(-k)$  which add up to a constant in the k-space or a  $\delta$ -function in the spatial domain. In a mathematical form,

$$\begin{aligned} \Phi(\alpha, x) &= \frac{1}{2\pi} \left( \int_{-\infty}^{\infty} u(k)e^{j2\pi k(x-\alpha)} dk + \int_{-\infty}^{\infty} u(-k)e^{j2\pi k(x-\alpha)} dk \right) \\ &= \frac{1}{2\pi} \int_{-\infty}^{\infty} e^{j2\pi k(x-\alpha)} dk = \delta(x - \alpha) \end{aligned} \quad (3.18)$$

Consequently, the resultant compound kernel under the non-overlapping condition is an identity kernel and complete restoration is possible in this case.

### 3.3.3 General case of arbitrary trajectory

In the case of an arbitrary k-space trajectory, the complete restoration with SPHERE is first proven when the inhomogeneity phase factor is periodic with period  $K$ , which corresponds to the periodic extension with a finite coverage in the k-space. Subsequently, the proof is generalized to the infinite coverage by taking the limit as  $K \rightarrow \infty$  in the same way the Fourier transform is derived from the Fourier series expansion.

When the inhomogeneity factor is periodic, it can be decomposed into a Fourier series. That is,

$$e^{j2\pi\Delta\nu(x)\cdot t(k)} = \sum_n \eta_n(\Delta\nu(x)) \cdot e^{j2\pi ndk} \quad (3.19)$$

and

$$e^{-j2\pi\Delta\hat{\nu}(x)\cdot t(k)} = \sum_n \eta_n^*(\Delta\hat{\nu}(x)) \cdot e^{-j2\pi ndk} \quad (3.20)$$

with fundamental frequency  $d = 1/K$ . Hence, the corresponding distortion and correction kernels are:

$$\Psi(\alpha, x) = \sum_n \eta_n(\Delta\nu(x)) \cdot \delta(x - \alpha + nd) \quad (3.21)$$

and

$$\Gamma(\alpha, x) = \sum_m \eta_m^*(\Delta\hat{\nu}(x)) \cdot \delta(x - \alpha - md) \quad (3.22)$$

It follows that:

$$\Phi(\alpha, x) = \sum_m \sum_n \eta_n(\Delta\nu(\alpha - nd)) \eta_m^*(\Delta\hat{\nu}(x)) \cdot \delta(x - \alpha + nd - md) \quad (3.23)$$

The double sum in Eqn.(3.23) can be decomposed into two components: the diagonal terms obtained when  $m = n$  and the remaining cross-terms. In the ideal case where there is no overlap which also implies that  $\Delta\nu(x - nd) = \Delta\hat{\nu}(x) \forall n \ni \eta_n \neq 0$ , the cross-terms vanish based on the following argument. Since both the distortion and correction kernels are linear and bounded (i.e., the result of applying any of them to any function will be finite and can be expressed as a linear combination of elements of that function), operator theory states that the norm of the compound kernel must be less than or equal to the multiplication of their individual norms [42]. Given that the norms of the distortion and correction operators are less than or equal to unity (as can be deduced from the decomposition into orthogonal pure phase kernels and invoking the triangle inequality), the norm of the compound kernel must be less than or equal to one. Now consider the output of applying this kernel. This output is composed of two main components: the zero-shift component corresponding to the diagonal terms

of the compound kernel and the nonzero-shift component corresponding to the cross terms. Since these two components are orthogonal (non-overlapping in space), the norm of the output will be equal to their geometric sum. It can be shown that the outcome from the diagonal terms alone will have a unity norm. Since the maximum output norm is unity from the definition of the kernel norm and since the norm is always positive, it follows that the norm corresponding to the cross terms must be zero. As a result, all of its components must be zero from their orthogonality. In other words, the compound kernel is the identity kernel, and complete restoration is achieved.

Now let us consider the generalization of the above solution to the case for which the inhomogeneity phase factor is non-periodic and has an infinite support. As the period  $K$  approaches infinity, the periodic function tends to have only one cycle in the interval  $-\infty < k < \infty$  that is identical to the inhomogeneity phase factor [48]. In approaching the limit, the fundamental frequency  $d$  becomes smaller as  $K$  is made larger and the frequency spectrum becomes denser. In the limit as  $K \rightarrow \infty$ , the sums in Eqns.(3.23) become integrals. Given that the final result of the above analysis is not a function of the fundamental frequency, it can be shown that it is true in the limit as well. That is, complete restoration can be achieved for an arbitrary inhomogeneity phase factor when the non-overlapping condition is satisfied.

### 3.3.4 Point spread function of SPHERE

In the above analysis, it was shown that the correction kernel was able to restore the true image under the idealized non-overlapping condition. Without overlapping, the correction kernel was constructed using exact knowledge of the inhomogeneity. In practice, the non-overlapping condition is usually not fully satisfied. The overlap may introduce some ambiguity in the process of redistributing pixels in the corrected image due to errors in estimating the correction kernel. To see how SPHERE works in practice, the correction process is examined under these non-ideal conditions. Specif-

ically, the spatially-dependent point spread function (PSF) of the compound kernel is derived and assessed to see how it is affected by practical limitations.

In the following, discrete sampling in the  $k$ -space is considered, and for simplicity, the field of view is normalized to 1 without loss of generality. To derive the PSF, a single point in the original image located at  $x_o$  is considered. This point is first distorted by the distortion kernel constructed with an inhomogeneity value  $\Delta\nu(x_o)$ . To calculate the contribution of the original point in the corrected image at any arbitrary point  $(x_o + \Delta x)$ , a correction kernel centered at  $(x_o + \Delta x)$  and constructed using an inhomogeneity value of  $\Delta\hat{\nu}(x_o + \Delta x)$  is applied. Expressing  $\Delta\hat{\nu}(x_o + \Delta x)$  as  $\Delta\nu(x_o) + \delta\nu$ , the final result can be expressed as a function of both  $\Delta x$  and  $\delta\nu$  and defined here as the *correction ambiguity function* or CAF(.,.). In a mathematical form,

$$\begin{aligned} CAF(\Delta x, \delta\nu; x_o) &= \int_{-1/2}^{1/2} \Psi(x_o, \beta) \cdot \Gamma(\beta, x_o + \Delta x) d\beta \\ &= \int_{-1/2}^{1/2} \mathcal{F}_{k \rightarrow \beta}^{-1} \left\{ e^{j2\pi\Delta\nu(x_o)t(k)} e^{-j2\pi k x_o} \right\} \\ &\quad \cdot \mathcal{F}_{k \rightarrow \beta}^{-1} \left\{ e^{j2\pi(\Delta\nu(x_o) + \delta\nu)t(k)} e^{-j2\pi k(x_o + \Delta x)} \right\}^* d\beta \end{aligned} \quad (3.24)$$

where  $\mathcal{F}_{k \rightarrow \beta}^{-1}\{\cdot\}$  is the inverse Fourier transform from the  $k$  domain to the  $\beta$  domain and the forms of  $\Psi(\alpha, x)$  and  $\Gamma(\alpha, x)$  from Eqns.(3.5) and (3.6) are invoked. From Parseval's theorem of the Fourier transform, given two periodic functions  $F(x)$  and  $G(x)$  and their Fourier transforms as the discrete functions  $f(k)$  and  $g(k)$ , the following identity is true [47]:

$$\sum_k f(k) \cdot g^*(k) = \int_{-1/2}^{1/2} F(x) \cdot G^*(x) dx. \quad (3.25)$$

This theorem states that the inner product of two functions does not change when the Fourier transform is applied. Hence, Eqn.(3.24) can be written as:

$$\begin{aligned} CAF(\Delta x, \delta\nu) &= \sum_k \left( e^{j2\pi\Delta\nu(x_o)t(k)} \cdot e^{-j2\pi k x_o} \right) \cdot \left( e^{-j2\pi(\Delta\nu(x_o) + \delta\nu)t(k)} \cdot e^{j2\pi k(x_o + \Delta x)} \right) \\ &= \sum_k e^{-j2\pi\delta\nu \cdot t(k)} \cdot e^{j2\pi k \cdot \Delta x}. \end{aligned} \quad (3.26)$$

Given this form of the ambiguity function, the spatially-dependent PSF is given by:

$$PSF(x, x_o, \Delta\hat{\nu}(x) - \Delta\nu(x_o)) = CAF(x - x_o, \Delta\hat{\nu}(x) - \Delta\nu(x_o)). \quad (3.27)$$

With this formalism, the PSF essentially corresponds to a curved profile of the 2-dimensional CAF, where the curve is determined by the functional form of  $\delta\nu$ . Eqns. (3.26) and (3.27) allow us to evaluate the PSF for any particular k-space trajectory. When  $\delta\nu$ , i.e.,  $(\Delta\hat{\nu}(x) - \Delta\nu(x_o))$ , is zero, the ambiguity function approaches a  $\delta$ -function. When  $\delta\nu$  is non-zero but small, the ambiguity function is still very close to a  $\delta$ -function. In Fig.(3.3), an example of the correction ambiguity function for the case of a centric-reordered segmented EPI sequence is presented as a surface plot (a) to depict the relative magnitude of the various components of the function and as a grey scale image (b) to illustrate the spatial dispersion. The PSF derived for this sequence before and after the correction process are illustrated in Fig.(3.4a) and (3.4b) respectively. The inhomogeneity was  $\Delta\nu = 2/T$  and the correction was applied such that  $\delta\nu = 1/2T$ , where  $T$  is the data acquisition period. Also, the two-dimensional extension of the above analysis is applied to evaluate the PSF of a spiral sequence with inhomogeneity  $\Delta\nu = 2/T$  and after the correction when  $\delta\nu = 1/2T$ ; the results are shown in Fig.(3.5). As can be observed, the resultant point spread functions are close to an ideal  $\delta$ -function.

The importance of Eqn.(3.27) lies in that it illustrates when SPHERE is a good approximation. It is a good approximation when  $\delta\nu$  is small. Observing that  $\Delta\hat{\nu}(x)$  is the result of mixing original signal magnitude, it is therefore bounded by the range of  $\Delta\nu(x)$  in a neighborhood defined by the blurring function. Under most practical situations,  $\Delta\nu(x)$  is smooth, and  $\delta\nu$  is usually small. Therefore, the approximation utilized in SPHERE is valid for most conditions. This observation also explains that the deviation of the compound kernel from the identity kernel in Fig.(3.2) occurred only in a location where  $\delta\nu$  is large.

### 3.4 Method

The technique requires an initial estimate of the image and an inhomogeneity map. In this implementation, the inhomogeneity map is derived from the phase difference of two images acquired at different  $TE$  values with the sequence of interest. The maps are smoothed with a spatial filter to improve the signal-to-noise ratio and thresholded based on the image magnitude to remove the background pixels. To eliminate phase-wrapping in the resultant phase map, Schafer's unwrapping procedure [43] was used. The resultant field map, along with the initial estimate of the image to be corrected, was used in the discrete version of Eqn.(3.2) to generate the simulated k-space data for the final image.

Since each point in the k-space is acquired at a different time in general, the exact implementation of SPHERE calls for a point by point correction, requiring a long reconstruction time. In practice, this stringent requirement can be relaxed to a large extent by suitable approximations based on the characteristics of the sequence of interest. Specifically, to reduce the computational complexity of SPHERE, it is implemented by dividing the data acquisition window into a number of non-overlapping partitions and treating each partition as an instant, or a time step, in the correction. The computational complexity of SPHERE is thus proportional to the number of time steps rather than the number of k-space points. In our implementation of SPHERE for EPI sequences, since the time required to scan individual k-space lines along the readout direction is relatively short and the inhomogeneity effects in this direction can be ignored, the k-space correction is performed on lines instead of points. In applying SPHERE to spiral scanning, the partitioning is achieved by dividing the k-space into equally spaced annular rings where each ring is considered to be acquired instantaneously. Note that this implementation corresponds to a nonuniform partitioning of the data acquisition window that is aimed at emphasizing the correction accuracy in the low k-space areas.

To illustrate the performance of this technique, it is applied to data obtained on a 1.5T Siemens Magnetom Vision MR scanner using sequences in which  $B_0$  inhomogeneity induced degradation has varying degrees of complexity. The first sequence was a single-shot blipped-EPI sequence. Experimental data were acquired in phantoms and normal human volunteers. For the phantom study, the imaging parameters are TR/TE: 200/70 ms, blip spacing: 0.96 ms, matrix:  $128 \times 128$ , slice thickness: 5 mm, and FOV: 31 cm  $\times$  31 cm. On the volunteers, sagittal and coronal images were obtained with imaging parameters identical to those used in the phantom study.

The second sequence studied was a segmented EPI sequence with centric reordering [34]. In this case, the off resonance degradation is more complicated and leads to a sum of two shifted versions of the original image. Experimental data in both phantoms and normal volunteers were obtained (same imaging parameters as blipped-EPI with 2 segments). These images were corrected with SPHERE and the resultant images were compared with images obtained using FLASH.

SPHERE was also applied to image different phantoms in addition to normal human volunteers using a spiral imaging sequence. The field map required for correction was obtained from two spiral acquisitions with different echo times. The k-space was covered by 16 interleaved spirals, each taking approximately 11 ms. The gradient waveforms used in this sequence were chosen according to previously described spiral scanning methods [44, 45]. The imaging parameters were: TR/TE: 1000/6 ms, FOV 31 cm  $\times$  31 cm, matrix:  $128 \times 128$ .

### 3.5 Results

Results obtained from single-shot blipped-EPI studies are presented in Fig.(3.6). Panel (d) illustrates images obtained using FLASH for comparison.  $B_0$  maps in these slices derived from two single shot EPI images after smoothing and phase unwrapping are shown in panel (a) (the shims are somewhat misadjusted in the phantom study

to accentuate the off-resonance effect). The  $B_0$  variation was in the range from  $-126$  to  $+138$  Hz for the phantom study and  $-100$  to  $+100$  Hz for the human study. EPI images obtained without correction (panel b) are highly distorted. Images obtained after line by line correction using SPHERE (128 time steps) (panel (c)) are virtually free of geometric distortion and structurally comparable to the corresponding FLASH images (panel (d)). Significant improvement can be noted in several areas in the corrected images. In particular, in the sagittal image obtained from the normal volunteer, substantial distortions in the frontal area of the brain due to the presence of large susceptibility-induced field inhomogeneity were successfully removed in the SPHERE corrected image.

In Fig.(3.7), results of a phantom study with the centrally reordered segmented EPI sequence are presented. Panels (b-d) illustrate the images obtained with the segmented EPI sequence without correction, with SPHERE correction (64 time steps), and the corresponding FLASH images respectively. The corresponding field maps are shown in panel (a) and the off-resonance frequency varied between  $-126$  to  $+138$  Hz for the first phantom,  $-33$  to  $+143$  Hz for the second, and  $-164$  to  $+167$  Hz for the third. The original images are degraded with spatial distortion as well as blurring. As a result of centric reordering, areas with substantial off-resonance frequency are ghosted on both sides of their original position. The corrected images in panel (c) exhibited both improved geometric accuracy and spatial resolution. In particular, areas that were substantially ghosted are brought back to their original position. These images demonstrate that, despite  $B_0$  inhomogeneity induced blurring, image degradation was significantly reduced by SPHERE. Fig.(3.8) presents results obtained with the same sequence in a normal volunteer. The first two images correspond to sagittal scans obtained with the phase-encoding direction vertical, while the third corresponds to a coronal scan with the phase encoding direction horizontal. The field inhomogeneity for the sagittal scans was between  $-100$  to  $+100$  Hz, and that of the coronal scan was between  $-94$  to  $+100$  Hz. Distortions seen in the original images

are essentially eliminated, markedly improving the quality of the image.

The results of a phantom study using a spiral sequence are illustrated in Fig.(3.9). The  $B_0$  field inhomogeneity maps are shown in Panel (a). The off-resonance frequency ranges for the phantoms starting from the leftmost were between  $-72$  to  $+170$  Hz,  $-89$  to  $+269$ , and  $-76$  to  $+247$  respectively. The spin-echo comparison images are shown in Panel (d). Panel (b) presents the spiral images reconstructed without correction. The images are degraded by blurring arising from the off-resonance effect. The images reconstructed using SPHERE (64 time steps) are shown in panel (c). The blurring in the original images is significantly reduced, providing a better definition of the small structures in the phantoms. Fig.(3.10) illustrates the results of applying SPHERE to correct the human brain images obtained with the same spiral sequence. The off-resonance frequency in these images varied from  $-228$  to  $+217$  Hz,  $-231$  to  $+213$  Hz, and  $-236$  to  $+200$  Hz starting from the leftmost image to the right respectively. The corrected images are sharper than the original images.

### 3.6 Discussion

The technique described in this chapter for reducing  $B_0$  inhomogeneity degradation in MR images was demonstrated theoretically and experimentally to be effective, even for cases with severe inhomogeneity. The Fourier space shift approach [31] which applies to sequences where only simple pixel shift occurs can be shown to be a special case of the present technique. Both SPHERE and the Fourier space shift method avoid the spatial domain interpolation needed by pixel shift based approaches. The significance of SPHERE is that it not only corrects for  $B_0$  inhomogeneity induced shifts, but also reduces the blurring commonly encountered in complex k-space trajectory sequences. Therefore, the new technique is general and can be applied to all types of sequences.

The correction ambiguity function (CAF) formalism provides a useful way of look-

ing at SPHERE as a space-varying matched filtering process. What the CAF describes is the response of SPHERE to errors in the matched filter estimation and the cross-talk between neighboring matched filters. In the ideal case when there is no overlap for example, the distortion functions to be detected are orthogonal yielding an ideal PSF of a  $\delta$ -function after the correction using SPHERE. On the other hand, when these functions are not orthogonal, there will be a certain amount of cross-talk between neighboring distortions indicating that an exact correction may not be possible in this case. This can be readily understood mathematically in the case of overlap by observing that the inverse problem of estimating the corrected image becomes ill-posed. This condition can be visualized by looking at the CAF of the imaging system. For example, for segmented EPI with centric reordering shown in Fig.(3.3), the ideal response is represented by the zero of the  $\delta\nu$  scale where the response is an exact  $\delta$ -function in the  $\delta x$  direction. When the overlap starts to cause bias errors in the estimation of the correction kernel (or equivalently when  $\delta\nu$  gets larger), the resultant response begins to deviate from the ideal response and a finite support function results instead of the ideal  $\delta$ -function. This is reflected as a weaker response peak magnitude and a wider response bandwidth. When the deviation from the ideal conditions becomes too significant, the correction process may fail to provide good results and a large portion of the original distortion remains as can be seen near the edges of Fig.(3.3b). Nevertheless, it should be noted that under most practical conditions, the inhomogeneity function is locally smooth and the correction is expected to be reasonably localized within the middle portion of the CAF, thereby providing effective correction. Even when this condition does not hold, the outcome of the technique can be shown to exhibit a reduced version of the original distortion. Therefore, it is clear that SPHERE is effective in reducing the  $B_0$  inhomogeneity under most practical imaging conditions.

It is interesting to compare SPHERE to other correction techniques in the literature. Many of the available techniques are based on pixel shifting in various forms

either in the spatial domain or the frequency domain by using Fourier shift theorem [25, 27, 28, 29, 31]. These techniques work only with linear k-space trajectory sequences such as blipped-EPI and cannot remove the blur encountered with the more complex imaging sequences such as centric reordered segmented EPI and spiral imaging. On the other hand, the conjugate phase method is based on an approximate inverse transformation from the k-space to the corrected spatial domain and can be used with complex sequences [30]. This method requires the acquisition of undistorted field maps, usually obtained using gradient echo sequences, and derives each point in the corrected image from the distorted k-space data and the estimated field inhomogeneity only at that point. In contrast, SPHERE derives each point in the corrected image space in terms of the estimated field inhomogeneity of all points, which is potentially advantageous besides being relatively immune to misregistrations between the distorted image and its field map. For example, when the distortion causes pixel shifts into areas outside the support of the undistorted object, the field map of the undistorted object in this area will be identically zero since these areas will be empty in the gradient echo field mapping images. As a result, the correction procedure in the conjugate phase method will leave these pixels unaltered, which in turn remain as artifacts near the boundaries. In contrast, this problem will not arise in SPHERE since the field map is derived based on the distorted image. An illustration of the comparison of conjugate phase and SPHERE is shown in Fig.(3.11) in which both methods were applied to the human data of Fig.(3.8). As can be seen, the edges in the SPHERE-corrected image are better defined when compared to the conjugate phase corrected image. This difference between SPHERE and the conjugate phase method also applies to other conjugate phase-based techniques such as those currently used for spiral imaging [37, 38]. The method in [38] has the advantage of not requiring a field map and therefore, is useful if field mapping is not available. The method described in [39] is quite efficient; however, it is applicable only when the field map is predominantly linear in nature. It should be noted that SPHERE can be

readily combined with this method instead of [38] with no additional data acquisition requirements to take advantage of the already available field mapping information.

Two practical scenarios of using SPHERE for dynamic imaging and functional imaging can be envisioned. The first is to acquire a reference scan for the volume of interest using a sequence that has a slightly different echo time from the one used in the actual data acquisition. Each image in the actual data is corrected based on the field map obtained from the image and the corresponding reference scan. Although this scenario requires that the object remains still between the acquisition of the reference data and the subsequent imaging, it has been successfully used with other artifact correction schemes in functional imaging applications [46]. The second scenario might be more suitable for dynamic imaging applications where the imaged object may change dramatically during the acquisition period. In this case, the slice or slices of interest can be scanned with alternative echo times such that all the odd acquisitions correspond to one echo time while the even acquisitions correspond to another slightly different echo time. Any given image with acquisition order  $n$  in the obtained sequence of images is corrected based on the field map obtained from the images  $n$  and  $(n - 1)$ . This approach allows the correction process to effectively track the changes in the field during the acquisition period because the reference image is also changing with time. Therefore, it is particularly suitable for dynamic imaging applications in which this property provides much more accurate field maps than the fixed reference scan method. It should be noted that these scenarios are also applicable with other correction techniques.

Let us now address the computational complexity of SPHERE. Consider first the 1-D case when the distortion is negligible along one of the two dimensions of an  $M \times N$  image, say the first dimension. The number of time steps used in SPHERE is equal to  $N$ . The technique first computes the field map from two images ( $O(M \cdot N)$  flops/image). Subsequently, for each line in the k-space along the first dimension, a space varying filter is applied to derive the corrected k-space

( $O(M \cdot N + M \cdot \log(M))$  flops/line, repeated for  $N$  lines/image). The corrected image is obtained by applying an inverse Fourier transform to the corrected k-space ( $O(M \cdot N \cdot \log(N) + N \cdot M \cdot \log(M))$  flops). Hence, the computational complexity for 1-D SPHERE is  $O(M \cdot N^2)$  flops/image. Using a similar argument, it can be shown that the complexity for the general case of using  $L$  time steps is  $O(L \cdot M \cdot N)$ , where  $L$  can be chosen by the user according to the desired accuracy/complexity. It should be noted that the step-wise implementation for SPHERE is similar to a method suggested for use with conjugate phase method [37]. Such an implementation corresponds to an approximation of 2-D SPHERE by repeated applications of 1-D SPHERE, providing a compromise between the accuracy and the computational complexity. In such an approximation, the accuracy is determined by the temporal width of each step. Consequently, with segmented data acquisition schemes where the sampling windows of each segment is reduced by the number of segments, the number of steps in the SPHERE implementation can also be reduced proportionally. An example of using SPHERE with different numbers of steps is illustrated in Fig.(3.12) to show the gradual improvement in the reconstruction as compared to the corresponding computational complexity.

Since the original image is multiplied by simple phase factors in Eqn.(3.2), noise in the original image is not amplified in the final image. However, the presence of noise in the field map will introduce additional noise in the final image. Therefore, in the current implementation, field maps are smoothed and thresholded based on the image magnitude. Several spatial and frequency domain filters were evaluated in this study, and it was found that a smoothing spatial domain kernel with a size of 5 pixels provided the best results. Our results confirmed that the uncertainties in field maps do not contribute substantially to the noise in the final image. Another effect of noise in the field map arises from changes in the CAF. Any additive noise superimposed on the field map will amount to a shift in the CAF in the direction  $\delta\nu$ , causing the point spread function to broaden. As a result, additive noise with large variance may bring

about some problems in the correction process and must therefore be filtered out. From our experience, the smoothing process described above kept the uncertainty in the field inhomogeneity estimation below 3% introducing negligible blurring in the correction process. Therefore, SPHERE can be considered robust in the presence of additive noise.

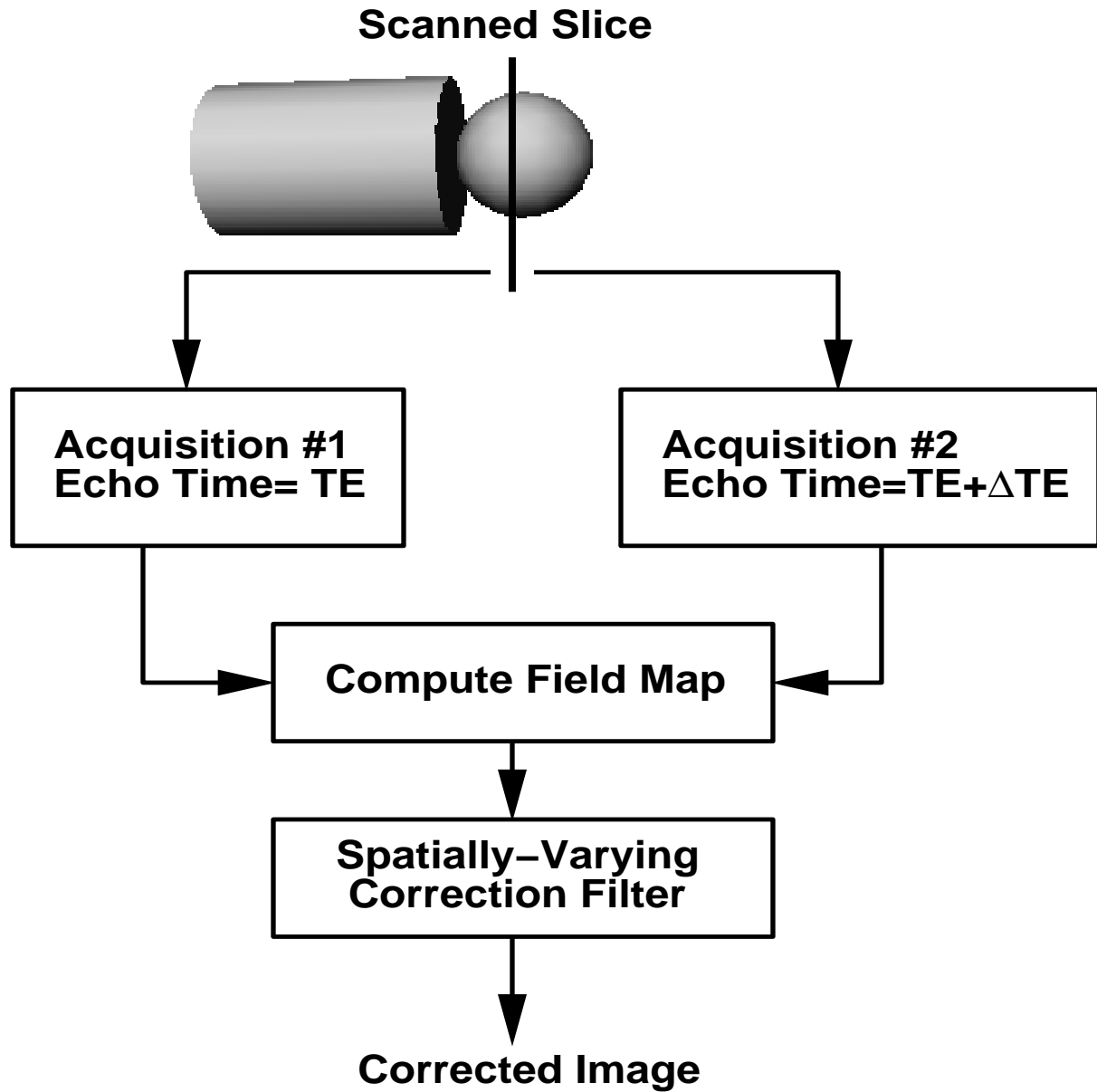


Figure 3.1: Block diagram of SPHERE.

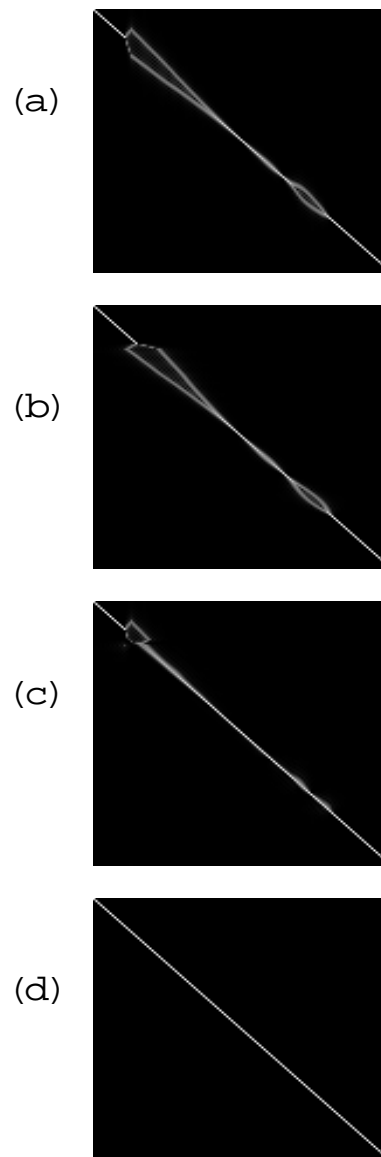


Figure 3.2: An illustration of the kernels encountered with the proposed SPHERE formalism in segmented EPI with centric reordering. (a) The distortion kernel. (b) The correction kernel used with SPHERE. (c) The resultant compound kernel which indicates a good correction. (d) ideal kernel with zero inhomogeneity.

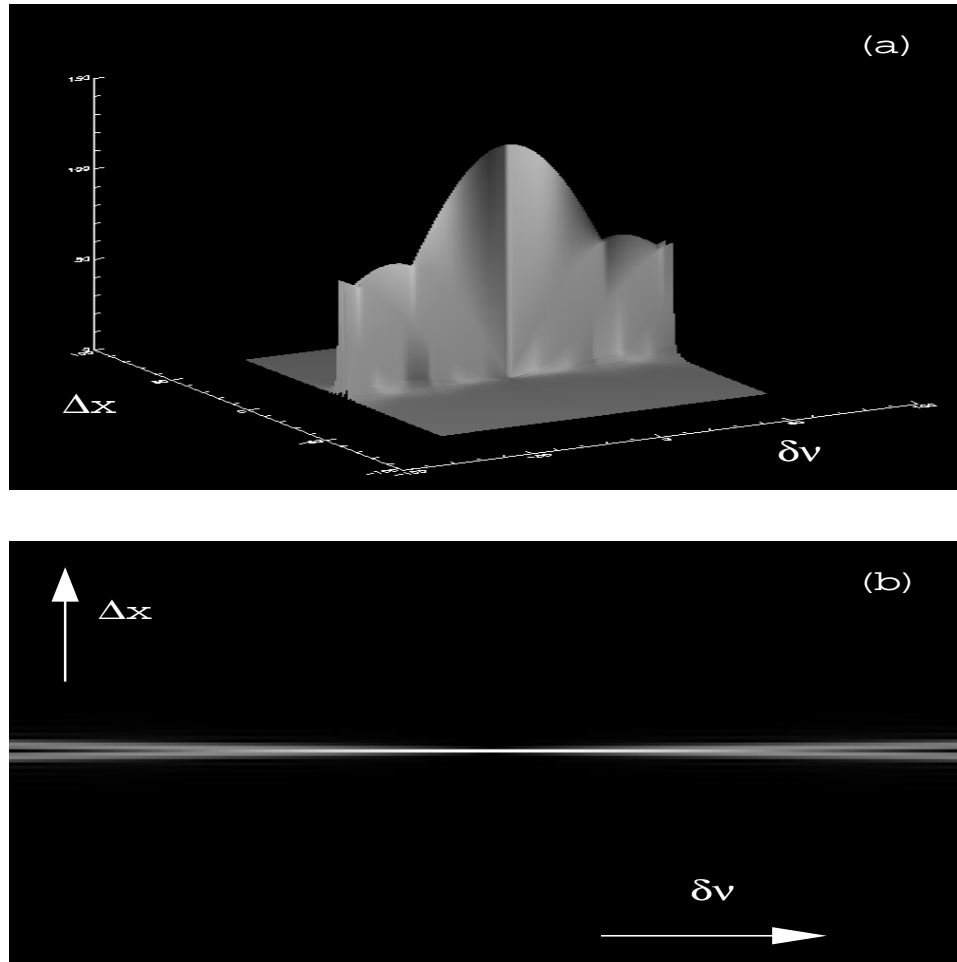


Figure 3.3: An illustration of the correction ambiguity function (CAF) for the case of segmented EPI with centric reordering. (a) Surface plot. (b) Image representation.

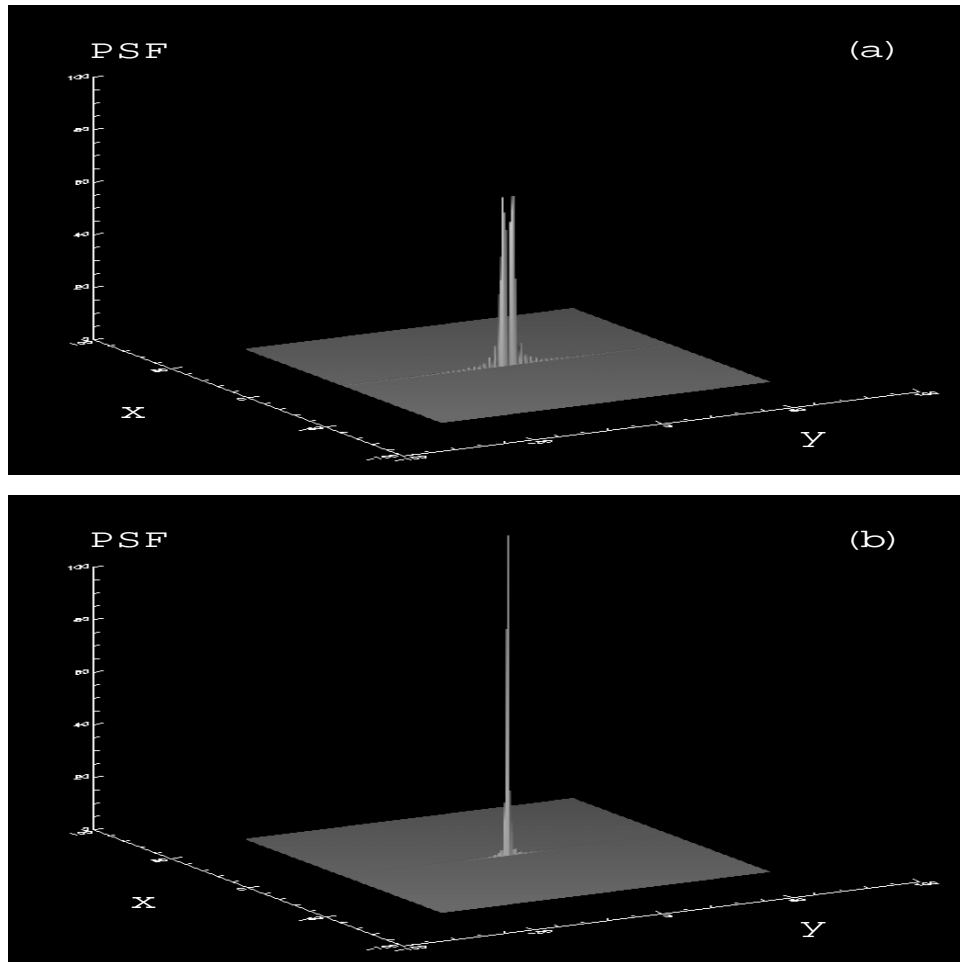


Figure 3.4: An illustration of the point spread function (PSF) for the case of segmented EPI with centric reordering. (a) Before correction. (b) After SPHERE correction.

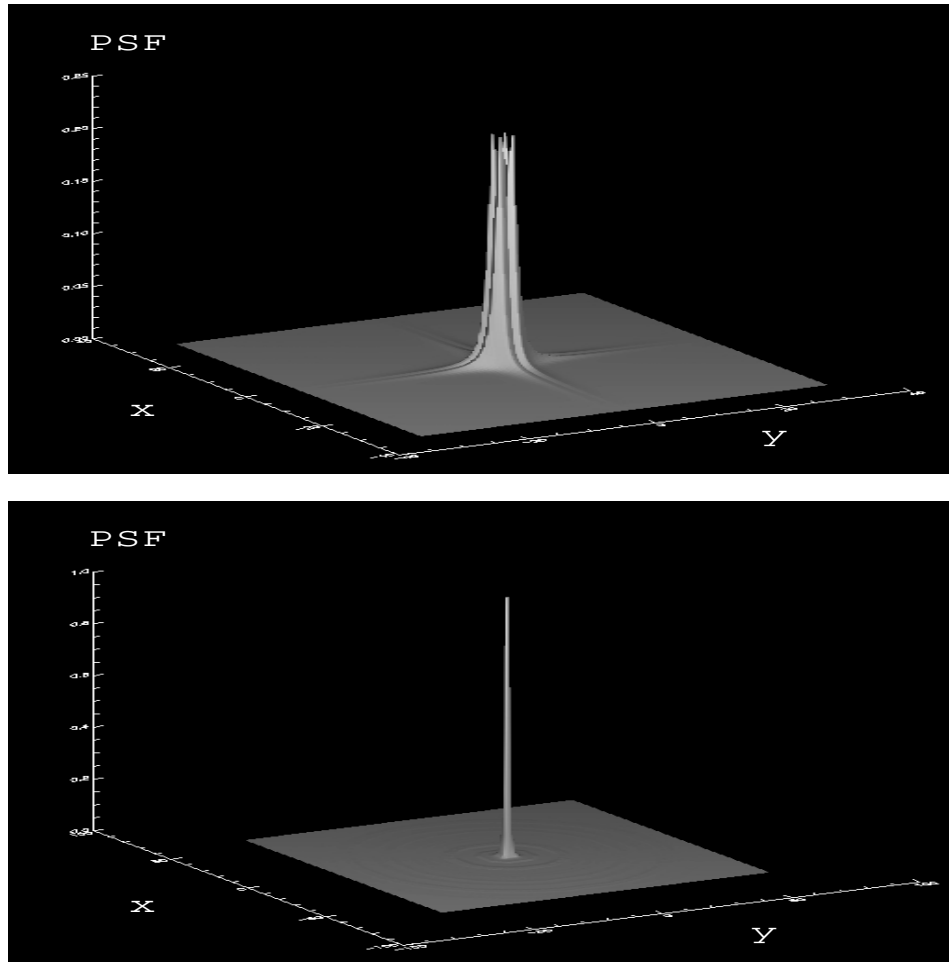


Figure 3.5: An illustration of the point spread function for the case of spiral imaging. (a) Before correction. (b) After SPHERE correction.

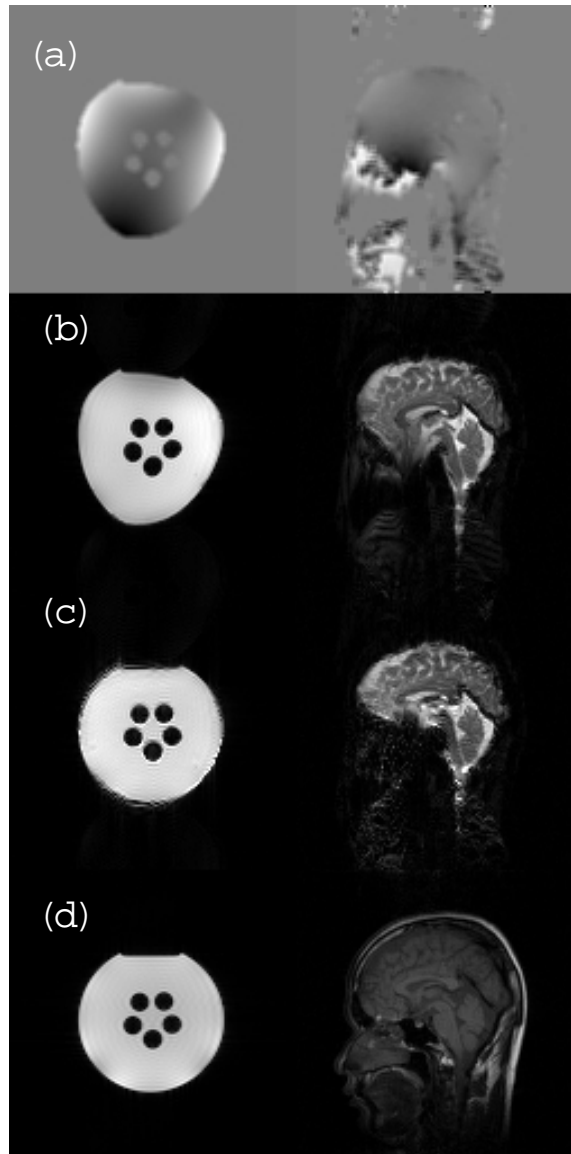


Figure 3.6: Phantom and human blipped-EPI data correction results using SPHERE. (a) Field maps. (b) Distorted images. (c) Corrected images. (d) Comparison gradient-echo images.

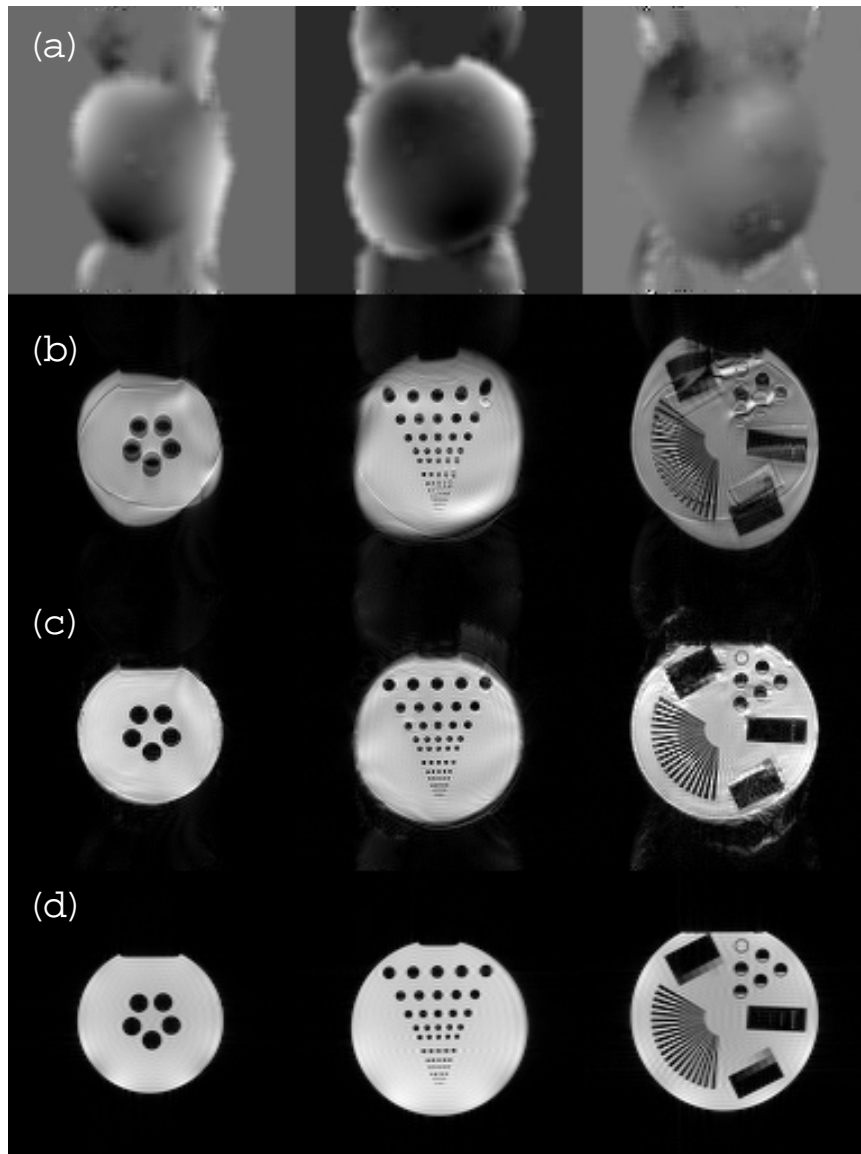


Figure 3.7: Results of using SPHERE to correct phantom data acquired with a segmented EPI sequence with centric reordering. (a) Field maps. (b) Distorted images. (c) Corrected images. (d) Comparison gradient-echo images.

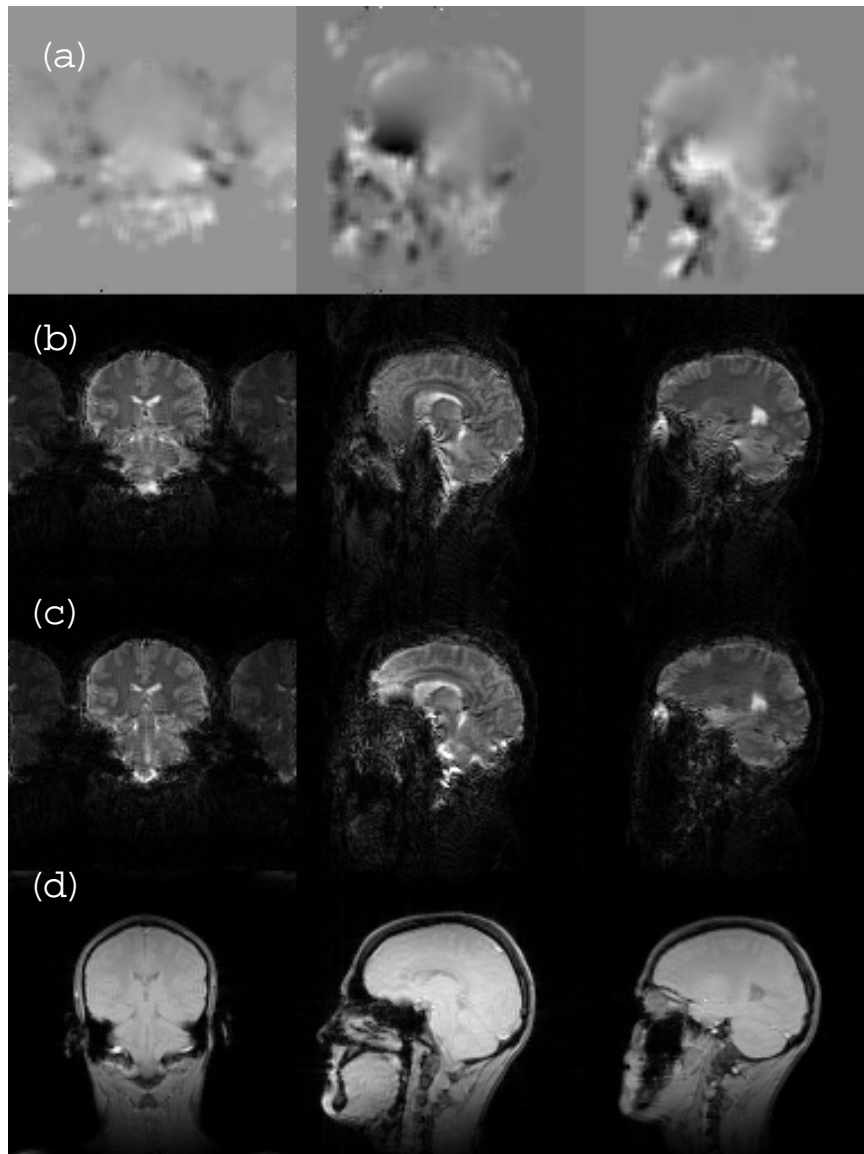


Figure 3.8: Results of using SPHERE to correct human data acquired with a segmented EPI sequence with centric reordering. (a) Field maps. (b) Distorted images. (c) Corrected images. (d) Comparison gradient-echo images.

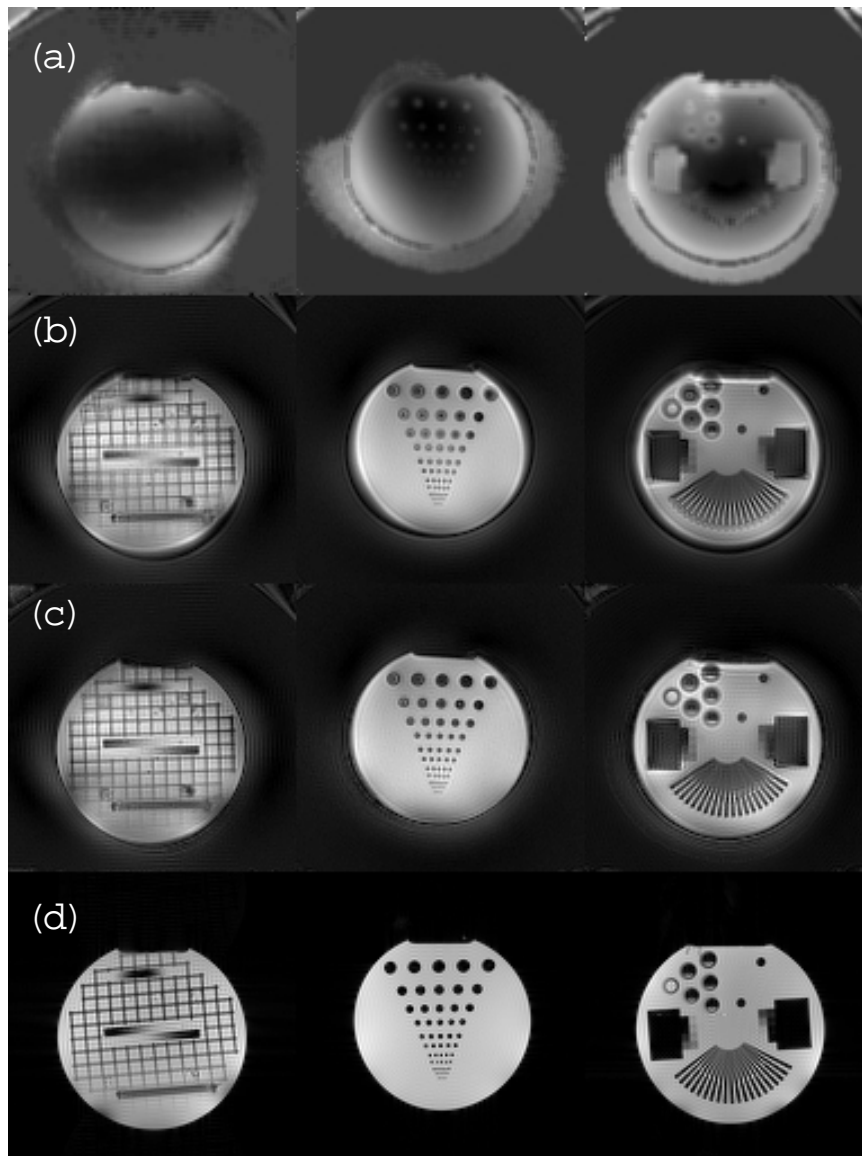


Figure 3.9: Results of using SPHERE to correct spiral scans of different phantom. (a) Field maps. (b) Distorted images. (c) Corrected images. (d) Comparison gradient-echo images.

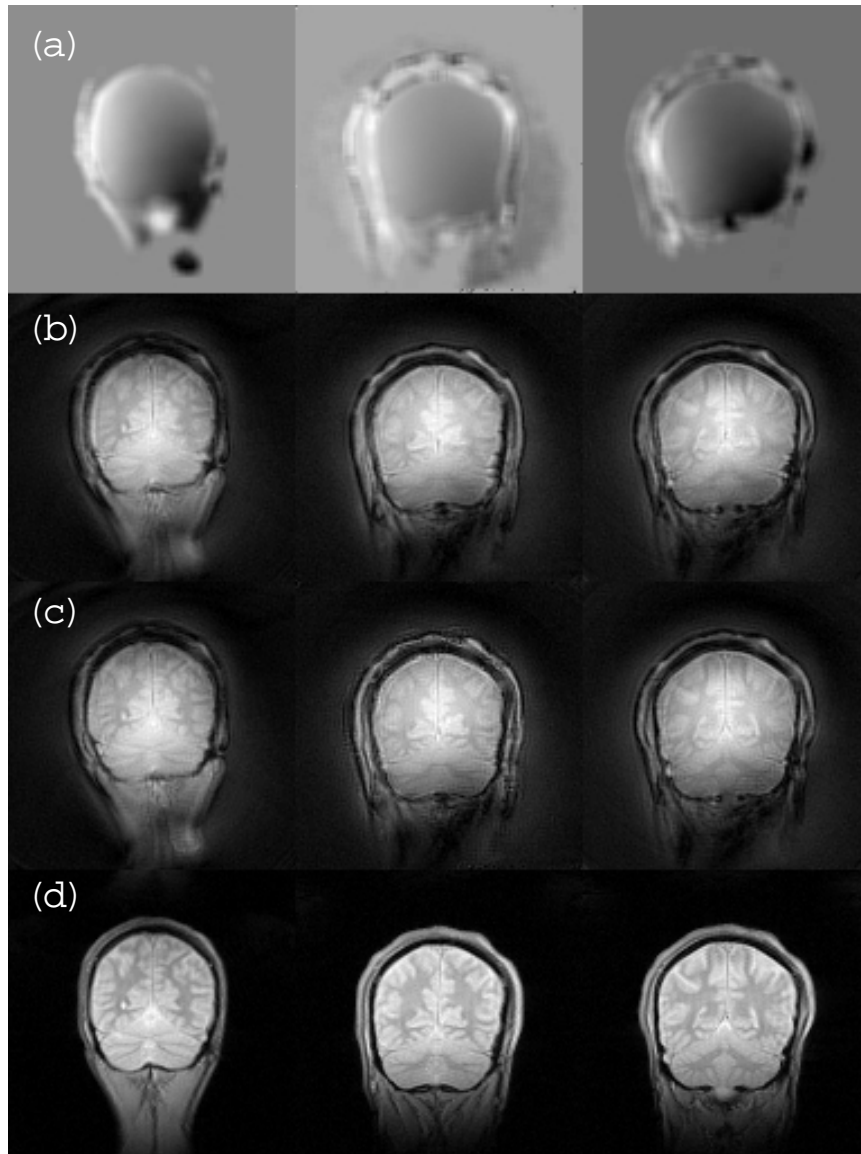


Figure 3.10: results of using SPHERE to correct spiral brain scans of a normal human volunteer. (a) Field maps. (b) Distorted images. (c) Corrected images. (d) Comparison gradient-echo images.

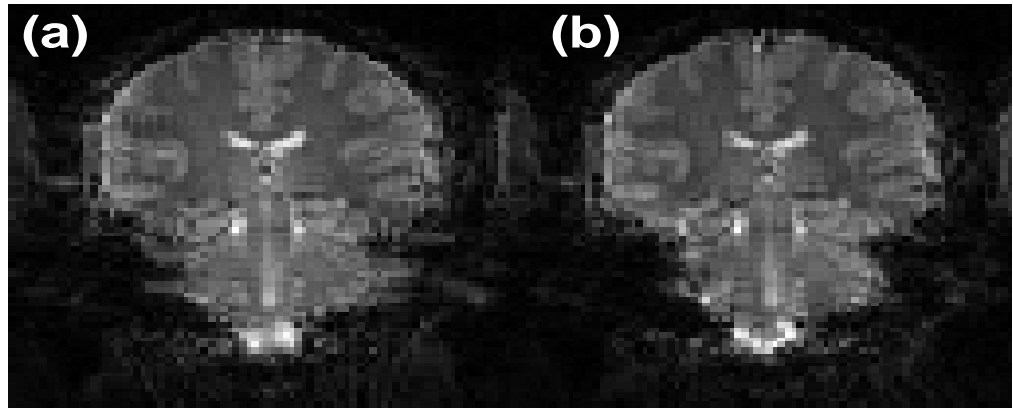


Figure 3.11: Comparison between SPHERE and the conjugate phase method as applied to correct the coronal scan of Fig.(3.8).

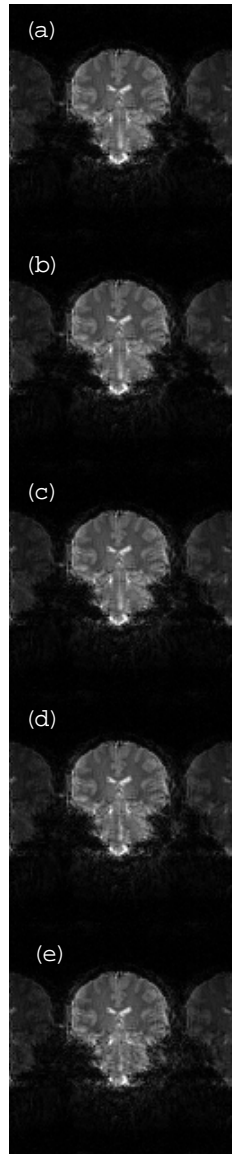


Figure 3.12: An illustration of correction segmentation using SPHERE with different numbers of steps. (a) 64 steps. (b) 32 steps. (c) 16 steps. (d) 8 steps. (e) 4 steps.

## Chapter 4

# ALGEBRAIC RECONSTRUCTION FOR MAGNETIC RESONANCE IMAGING UNDER $B_0$ INHOMOGENEITY

### 4.1 Introduction

The process of image reconstruction in magnetic resonance imaging can be expressed as an inverse problem of a generally known imaging operator. While existing reconstruction techniques provide satisfactory results in many situations, they correspond to approximate inverses of the imaging operator when  $B_0$  inhomogeneity is severe and the imaging operator ceases to be unitary. Consequently, the reconstructed images are not optimal. Therefore, a reconstruction method that is based on solving for the inverse of the imaging operator such that the norm of the error is minimum can be advantageous.

In this chapter, an algebraic model and an optimal solution to the problem of  $B_0$  inhomogeneity distortion correction when the distortion is rather severe along only one of the image dimensions. The 1-D continuous case is first considered and shown to be a Fredholm integral equation of the first kind. Discretization strategies are proposed to translate the continuous problem into a linear system of equations that can be solved numerically to obtain the least-squares solution. Several computational methods of different characteristics are described to compute this solution in an accurate and stable fashion under linear constraints. The issue of selecting an imaging sequence to provide the best results with the algebraic reconstruction method is addressed, and

it is shown that in general nonlinear k-space trajectories provide better results than linear ones. Finally, the performance of the approach is demonstrated by computer simulations and experimental data [49, 50].

## 4.2 General Problem formulation

### 4.2.1 Continuous problem formulation

Consider the case of Fourier imaging of a 1-D object of spatial intensity  $f(x)$  in the presence of field inhomogeneity represented by  $\Delta B(x)$ . The resultant continuous k-space of this object  $F_d(k)$  takes the form:

$$F_d(k) = \int_{-\infty}^{\infty} f(x) \cdot e^{j2\pi\gamma\Delta B(x)\cdot t(k)} \exp\{-j2\pi kx\} dx. \quad (4.1)$$

Here,  $\gamma$  is the gyromagnetic ratio and  $t(k)$  is a time function that depends on the k-space trajectory of the imaging sequence. This equation represents a linear Fredholm integral equation of the first kind with kernel,  $K_I(x, k) = e^{j2\pi\gamma\Delta B(x)\cdot t(k)} \exp\{-j2\pi kx\}$  [56]. That is, the k-space data can be expressed as the outcome of applying a linear operator  $\mathcal{T}$  to the original or *true* spatial intensity such that:

$$F_d = \mathcal{T}(f). \quad (4.2)$$

Throughout this paper,  $\mathcal{T}$  will be referred to as the *transformation* operator since it performs the mapping between the original object and the k-space. An equivalent formulation can be generated by premultiplying Eqn.(4.2) with  $\mathcal{T}^*$ . In this case, the operator equation is expressed in terms of the *Grammian* operator defined as  $\mathcal{G} = (\mathcal{T}^* \cdot \mathcal{T})$ . Moreover, premultiplying by  $\mathcal{F}^*$ , the inverse Fourier transform operator, another interesting operator equation arises in which the original object function  $f$  is mapped directly to the resultant distorted spatial distribution  $f_d$ . The operator in this equation will be referred to as the *deformation* operator  $\mathcal{D} = (\mathcal{F}^* \cdot \mathcal{T})$ . Since these three operator equations are equivalent, the choice of the one to use depends on their

relative advantages as applied to the specific solution method at hand. Examples of such features include the transformation operator being Vandermonde in some cases, the Gramian operator being Hermitian, and the deformation operator being sparse.

In general, an operator  $\mathcal{A}$  can be fully described by a mapping rule from the Hilbert space of its domain to that of its range that is defined by the available information about data acquisition. The reconstruction problem then becomes the one of finding an inverse operator  $\mathcal{A}^\dagger$  such that,

$$(\mathcal{A}^\dagger \cdot \mathcal{A}) = \mathcal{I} \quad (4.3)$$

where  $\mathcal{I}$  is the *identity operator*. Then, the solution to the original problem of finding  $f$  is given by,

$$\mathcal{A}^\dagger(F_d) = (\mathcal{A}^\dagger \cdot \mathcal{A})(f) = \mathcal{I}(f) = f \quad (4.4)$$

In general, the mapping rule that defines the operator may not be one-to-one. In this case, the operator is *singular*, and it is not possible to construct the inverse operator. In some other cases, the operator maps different points in its domain to different yet very close points in its range. If these points are too close, slight contamination with additive noise can render them indistinguishable, making it difficult to compute the inverse operator. The operator in such cases is *ill-posed* [54]. In this case, it is only possible to seek a regularized inverse operator to obtain a solution.

Any linear operator over the Hilbert space can be completely defined by its eigen- or singular value decomposition. When the operator is ill-posed or singular, the domain of the operator can be divided into two orthogonal subspaces. The first is defined by the eigen-functions or singular functions corresponding to the eigenvalues or singular values that are above a selected threshold, while the second is spanned by the remainder of those functions. The first subspace is termed the *minimum-norm* space, since it defines the space of all minimum-norm solutions to the inverse problem involving this operator. The second subspace is the *null space* of the operator. When the inhomogeneity operator has blind spots defined by the null space in its domain,

the components of the input spatial distribution that lie within these spots cannot be recovered. Since the null and minimum-norm subspaces are orthogonal and together they are complete, the least squares solution corresponds to the addition of two components: the inversion of the well-posed projection of the original operator onto the minimum-norm subspace applied to the available data, and any function in the null subspace. The process of obtaining the minimum-norm part of the solution is called *pseudo-inversion*.

Several forms of optimal solutions to the general class of inhomogeneity problems represented by linear integral equations of ill-posed operators can be considered. The first one is the minimum-norm or minimal least-squares solution. This solution is a special case when  $f_{NULL}$  is chosen to be zero. Given the definition of the null space of the operator and some general constraints based on *a priori* information about the imaged object, possible alternative solutions can be obtained by adding functions in the null space to the minimum norm solution such that these constraints are satisfied.

Observing that the operator in this problem is a linear operator, it is possible to obtain a solution based on full-rank operator composition achieved by reducing the size of the null space with over-sampling. Oversampling can be achieved by using multiple scans with different k-space trajectories. In the absence of magnetic field inhomogeneities, oversampling would be considered redundant. Nevertheless, when magnetic field inhomogeneities exist, it plays a significant role in improving the conditioning of the operator equation and eliminating the null space.

#### 4.2.2 Discretization

For practical implementation, it is necessary to discretize the original problem before attempting to obtain the solution. The discretization can be done in a variety of ways that approximate the integral with a finite sum. In general, the discretized problem

takes the form:

$$\sum_{n=1}^N w_n K_I(k, x_n) \cdot f(x_n) = F_d(k) \quad (4.5)$$

where  $w_n$  are weights that are direct functions of the discretization rule. Notice that in practice it is only possible to collect limited extent, discrete samples in the  $k$ -space. Therefore, *collocation* is invoked to convert the above equation to the desired finite-dimensional problem [56]. That is, to force the continuous equation to hold at specified collocation points such that,

$$\sum_{n=1}^N w_n K_I(k_m, x_n) \cdot f(x_n) = F(k_m) \quad , \quad m = 1, 2, \dots, M \quad (4.6)$$

In this case, the original integral equation is approximated by an  $M \times N$  linear system,  $\mathbf{A}\vec{f} = \vec{F}_d$ , where  $\mathbf{A}$  is an  $M \times N$  matrix with entries  $[w_n K_I(k_m, x_n)]$ ,  $\vec{f}$  is an  $N \times 1$  vector with entries  $[f(x_n)]$ , and  $\vec{F}_d$  is an  $M \times 1$  vector with entries  $[F_d(k_m)]$ . The most common approach to evaluate the weights  $w_n$  is the *midpoint rule*. In this method, a numerical integration rule (e.g., Simpson's rule) is applied to the continuous integral, yielding a sum with equal and constant weights (ignoring edge effects). Therefore, up to a constant multiplier, the weights for the midpoint rule are given as:

$$w_n^{midpoint} = 1 \quad , \quad n = 1, 2, \dots, N \quad (4.7)$$

Another method of discretization assumes that  $f(x)$  can be modeled as a piecewise constant function. In this case, within any given interval  $[x_n, x_{n+1})$ , the intensity and inhomogeneity functions are expressed as

$$f(x) = c_n \quad \text{and} \quad \Delta B(x) = \alpha_{n,0} + \alpha_{n,1} \cdot (x - x_n) \quad (4.8)$$

with  $c_n$ ,  $\alpha_{n,0}$  and  $\alpha_{n,1}$  are evaluated by matching the model to the available values of  $f(x)$  and  $\Delta B(x)$  at  $x_n$  and/or  $x_{n+1}$ . Assuming uniform intervals of constant width  $\Delta x$ , the weights in the finite-dimensional equation take the form:

$$w_n^{piecewise}(k_m) = \text{Sinc}(\pi(1 - \alpha_{n,1}) \cdot \Delta x \cdot k_m) \quad (4.9)$$

When  $\Delta x$  becomes very narrow, this approximation and the midpoint rule become equivalent. Otherwise, the two models may provide different results.

It should be noted that the discretization of an ill-posed integral equation of the first kind yields an *ill-conditioned* linear system. In general, the higher the resolution of this discretization, the closer the finite-dimensional problem to the ill-posed continuous problem and consequently, the more ill-conditioned the algebraic problem becomes [56]. Given that the size of common MRI inhomogeneity correction problems is usually large (around 128), the ill-conditioning of the algebraic problem is expected to be severe. Therefore, numerical solution methods proposed to solve this problem must be able to maintain robust performance under these conditions in order to obtain a stable inverse to this system.

### 4.2.3 Inhomogeneity problem in EPI: from 2-D to 1-D

In EPI, the data acquisition time is negligible along one of dimensions and  $t(k_x, k_y)$  can be considered as a function of one component, i.e.,  $t(k_x, k_y) \approx t(k_y)$  without loss of generality. In this case, the 2-D k-space data take the form:

$$F_d(k_x, k_y) = \int \int_{-\infty}^{\infty} f(x, y) \cdot e^{j2\pi\gamma\Delta B(x,y)\cdot t(k_y)} \cdot \exp[-j2\pi(k_x x + k_y y)] dx dy \quad (4.10)$$

where  $f(\cdot, \cdot)$  is the true signal within the imaged slice,  $F_d(\cdot, \cdot)$  is the obtained distorted k-space,  $\Delta B(\cdot, \cdot)$  is the corresponding inhomogeneity field map, and  $t(\cdot)$  is a function of the k-space time trajectory. Performing a 1-D inverse Fourier transform operation with respect to  $k_x$  on both sides of the above formula, the resultant form can be expressed as:

$$\hat{F}_d(x_o, k_y) = \int_{-\infty}^{\infty} f(x_o, y) \cdot e^{j2\pi\gamma\Delta B(x_o,y)\cdot t(k_y)} \cdot \exp[-j2\pi k_y y] dy \quad (4.11)$$

where  $\hat{F}_d(\cdot, \cdot)$  is the inverse Fourier transform of  $F_d(\cdot, \cdot)$  with respect to the first dimension. As can be seen, this form is similar to the 1-D problem where the given

data are the k-space representation of the object, the inhomogeneity field map, and the k-space time trajectory; while the unknown is the spatial distribution along a particular line in the image defined by  $x = x_o$ . Hence, by solving a set of 1-D problems that sufficiently sample the image structure in the  $x$ -dimension, the solution to the 2-D problem is obtained.

It should be noted that the above discussion is general for EPI since no particular form for  $t(k_y)$  in Eqn.(4.11) was assumed. Examples of possible forms of this function include  $t(k) = \text{constant} \times k$  for blipped-EPI, and  $t(k) = \text{constant} \times |k|$  for segmented-EPI with centric reordering.

#### 4.2.4 Example of a matrix operator

As an example, the case of a blipped-EPI imaging sequence is examined in this section. The midpoint discretization method is used and the corresponding linear system is derived. In this particular case, the discrete transformation operator  $\mathcal{T}$  takes a Vandermonde matrix form with a constant phase function in the solution. The Vandermonde matrix takes the form [57],

$$\mathbf{V} = \begin{bmatrix} 1 & 1 & \cdots & 1 \\ \lambda_o & \lambda_1 & \cdots & \lambda_N \\ \lambda_o^2 & \lambda_1^2 & \cdots & \lambda_N^2 \\ \vdots & \vdots & & \vdots \\ \lambda_o^N & \lambda_1^N & \cdots & \lambda_N^N \end{bmatrix} \quad (4.12)$$

This matrix can be completely defined by only one row in the form:  $[\lambda_o \lambda_1 \cdots \lambda_N]$ , which is usually called the Vandermonde coefficient vector. This can be of great advantage for reducing the storage space when the matrix is large or when the number of systems to be solved is large. For our problem, the elements of the Vandermonde coefficient vector corresponding to the transformation operator take the form,

$$\lambda_n = e^{j2\pi\gamma\Delta B(x_o, y_n) \cdot \Delta k} \cdot \exp[-j2\pi y_n \cdot \Delta k] \quad (4.13)$$

where  $\Delta k$  is the step size in the  $k$ -space. On the other hand, the matrix corresponding to the Gramian operator of this Vandermonde system is a member of the class of Hilbert matrices [61]. On the other hand, the columns of the deformation operator are related to the Vandermonde transformation operator through a Fourier transform. Given that each column of the Vandermonde matrix corresponds to samples of a complex exponential, it is expected that each column of the deformation matrix will contain only a few non-zero elements. In fact, if the sampling scheme happens to be ideal for the particular frequency of a given column, its corresponding deformation matrix column will contain exactly one element. In other words, the number of nonzero elements depends on the severity of the leakage problem in the sampling scheme used, but is generally much smaller than the size of the matrix. Hence, the deformation matrix is *sparse* [55]. Moreover, the elements of this matrix are generally expected to be somewhat centered around the main diagonal. Therefore, it can be considered as a constant bandwidth sparse matrix with a bandwidth determined by the maximum inhomogeneity.

Beyond the apparent possible computational and storage advantages of this formulation, the deformation matrix also provides an explicit visual interpretation of the inhomogeneity problem. When there is no inhomogeneity at a particular location, the matrix column corresponding to this location is equal to the corresponding column of an identity matrix. Conversely, if there is an inhomogeneous field at a certain location, two possible scenarios can be encountered: corresponding to a shifted version of an identity matrix column, and a blur extending over a number of locations around the nonzero element. Given the deformation matrix, it is possible to identify the presence of overlap among distortions from neighboring pixels by inspecting its rows. In general, when there are many such overlaps, shift-based correction methods fail. Therefore, it may be advantageous to use this matrix to analyze the inhomogeneity effects before resorting to a particular correction method. It should be noted that this matrix is similar to the distortion kernel shown in Fig.(3.2) for the case of

segmented EPI with centric reordering.

Of note is that a similar analysis can also be derived for the general case of nonlinear  $t(k)$  such as segmented-EPI. The transformation operator is not a Vandermonde matrix in this case, and the deformation matrix is still sparse but expected to have a wider bandwidth because of the extra blur associated with the point spread functions of such sequences.

### 4.3 Imaging Sequence Dependence

It is interesting to consider the dependence of the conditioning of the operators on the imaging sequence. As can be seen from the above example, the operator matrix is a function of  $t(k)$ , which is defined by the k-space trajectory of the imaging sequence. Therefore, the conditioning of the operators depends on the form of  $t(k)$ .

In general, ill-posed operators are operators that are close to singular operators. Therefore, a good criterion for assessing the well-posedness of an operator is to check for possible singularities under small perturbations in its parameters. When singularities exist, it is expected that the operator will generally be ill-posed in practice. On the other hand, if there are no singularities, the operator is expected to maintain its well-posedness.

In order to apply this criterion here, consider an inhomogeneity operator applied to two points at different locations in the field of view (without loss of generality). To derive the singularity condition is equivalent to deriving the conditions under which the outcome of applying the operator in both cases is the same. If such conditions exist, the operator is said to have singularities and practical matrix operators are expected to be ill-conditioned, and vice versa. The signals from two points located at  $x_1$  and  $x_2$  with magnetic field inhomogeneities  $\Delta B(x_1)$  and  $\Delta B(x_2)$  are given by,

$$r_1(k) = e^{-j2\pi kx_1} \cdot e^{j2\pi\gamma\Delta B(x_1)t(k)} \quad (4.14)$$

and

$$r_2(k) = e^{-j2\pi k x_2} \cdot e^{j2\pi\gamma\Delta B(x_2)t(k)}. \quad (4.15)$$

Usually these signals are observed for a finite interval, say  $[-1/2, 1/2]$ . In order to assess the independence of these signals, the inner product of the two signals over the observation period is evaluated as,

$$\langle r_1, r_2 \rangle = \int_{-1/2}^{1/2} e^{-j2\pi k(x_2-x_1)} \cdot e^{j2\pi\gamma(\Delta B(x_2)-\Delta B(x_1))t(k)} dk. \quad (4.16)$$

Let  $\Delta n = x_2 - x_1$  and  $\Delta b = \gamma(\Delta B(x_2) - \Delta B(x_1))$ , and define the distortion function  $d(k; \Delta b) = e^{j2\pi\gamma(\Delta B(x_2)-\Delta B(x_1))t(k)}$ . Assuming the periodicity of the k-space and invoking Parseval's identity of the Fourier transform, the inner product can be written in the form,

$$\langle r_1, r_2 \rangle = \sum_n \delta(n - \Delta n) D(n; \Delta b) = D(\Delta n; \Delta b). \quad (4.17)$$

Here  $D(n; \Delta b)$  is the inverse discrete-time Fourier transform of  $d(k; \Delta b)$ . Hence, the result of the inner product depends mainly on the value of the Fourier transform of the distortion function. When singularities exist, this inner product becomes equal to the square of the norm of either signal, indicating that the two signals are identical.

Now consider the two main functional form categories of  $t(k)$ , namely, linear and nonlinear functions. In the first,  $t(k) = k$  up to a constant such as with blipped-EPI. In this case, the outcome of the inner product can be shown to take the form:

$$\langle r_1, r_2 \rangle_{linear} = \delta(\Delta n - \Delta b) \quad (4.18)$$

As a result, the operator in this case will be singular at all points with locations and inhomogeneities satisfying  $\Delta n = \Delta b$ . Hence, the matrix operators in this case are expected to be ill-conditioned. On the other hand, for nonlinear functional forms of  $t(k)$ , it is generally not possible to find such operator singularities. For example, consider the case of a segmented-EPI with centric-reordering, where  $t(k) = |k|$  up to a constant. In this case, it can be shown that the inner product takes the form:

$$\langle r_1, r_2 \rangle_{non-linear} = \frac{1}{2} (\delta(n - \Delta n + \Delta b) + \delta(n - \Delta n - \Delta b))$$

$$+\frac{1}{j} \left( \frac{1}{n - \Delta n + \Delta b} - \frac{1}{n - \Delta n - \Delta b} \right) \quad (4.19)$$

Two main conclusions can be drawn from this form. First, the inner product becomes a single  $\delta$ -function only in the trivial case when  $\Delta n = \Delta b = 0$ . Second, the maximum values of this form occur at  $n = \pm\Delta b$ , and is equal to approximately half the result in the trivial case. As a result, the matrix operators obtained with this sequence are expected to be better-conditioned than linear trajectories in practice. Therefore, from a theoretical point of view, it is always advantageous to use nonlinear k-space trajectories when inhomogeneity distortions exist and are to be corrected for in the reconstruction.

## 4.4 Numerical Solution Methods

### 4.4.1 SVD matrix solver

As discussed above, eigen-decomposition or singular value decomposition can be used to identify the null space of a given linear system and to obtain the least squares solution. Given the superior numerical properties of the singular value decomposition (SVD), it is usually the method of choice for this computation. Using SVD, any  $N$ -dimensional matrix operator,  $\mathbf{A}$ , can be expressed in an orthogonal representation of the form:

$$\mathbf{A} = \mathbf{U}\mathbf{\Sigma}\mathbf{V}^T = \sum_{n=1}^N \sigma_n \vec{u}_n \vec{v}_n^T \quad (4.20)$$

where  $\sigma_n$  is the  $n$ -th singular value and  $\vec{u}_n$  and  $\vec{v}_n$  are members of the orthonormal sets of vectors in the columns of  $\mathbf{U}$  and the rows of  $\mathbf{V}$ , spanning the space of  $N$ -D vectors. In the case when the system is well-conditioned, the inverse of the matrix operator  $\mathbf{A}$  is given directly as:

$$\mathbf{A}^\dagger = \sum_{n=1}^N \frac{1}{\sigma_n} \vec{u}_n \vec{v}_n^T \quad (4.21)$$

On the other hand, when the system is ill-conditioned, some singular values are too small to distinguish from the usual numerical noise encountered in this computation.

Consequently, the solution given above will be dominated by artifacts from the basis vectors corresponding to those very small singular values. In this case, the method of truncated singular value decomposition (TSVD) can be used to provide stable solutions that are optimal in the least square sense. In this method, the singular values are thresholded and only those values above the threshold are included in the above expansion to derive the inverse. With appropriate selections of the truncation level, TSVD is a regularization method. Hence, as with any regularization method for ill-posed problems, the choice of this truncation level is critical. For a fixed amount of noise, the TSVD will begin to diverge if the truncation level is increased beyond a certain level. It should be noted that choosing the truncation level can be shown to be equivalent to imposing a quadratic constraint on the solution.

#### 4.4.2 Conjugate gradient method (CGM) matrix solver

Among known robust linear system solvers, the conjugate gradient method (CGM) proposed originally by Hestenes and Stiefel [59, 60] is considered one of the most efficient. This method describes a class of iterative techniques that has the desirable property of guaranteed convergence in a finite number of iterations. Also, even when the system is ill-conditioned, good estimates of the largest and smallest eigenvalues are not needed to determine the algorithm parameters. The basic idea of this method is to eliminate the residual error  $\vec{e} = \mathbf{A} \cdot \vec{x}_{sol} - \vec{b}$  in a linear system  $\mathbf{A}\vec{x} = \vec{b}$ , along mutually  $\mathbf{A}$ -orthogonal directions spanning the space of the solution [60, 62]. The original formulation of this technique requires the system to be real, square, symmetric and positive definite for the algorithm to work and provide the unique solution to the system. Nevertheless, a direct modification of the technique can be applied to complex Hermitian, positive semidefinite linear systems to compute the minimal least square solution. Therefore, it can be used to solve the normal equations of the system given the properties of the Gramian matrix defined by  $\mathbf{G} = \mathbf{T}^* \cdot \mathbf{T}$ .

The conjugate gradient algorithm to solve the normal equation  $\mathbf{A}^* \mathbf{A} \vec{x} = \mathbf{A}^* \vec{b}$  is

described as follows:

1. Choose the initial solution  $\vec{x}_o$  as the distorted object.
2. Compute the initial residual  $\vec{r}_o = \vec{b} - \mathbf{A}\vec{x}_o$ .
3. Compute first direction  $\vec{p}_o = \mathbf{A}^* \vec{r}_o$ .
4. Compute  $c_m = \|\mathbf{A}^* \vec{r}_m\|_2^2$ ,  $d_m = \|\mathbf{A} \vec{p}_m\|_2^2$ , and  $a_m = c_m/d_m$ .
5. Update solution  $\vec{x}_{m+1} = \vec{x}_m + a_m \cdot \vec{p}_m$ , and update residual  $\vec{r}_{m+1} = \vec{r}_m - a_m \cdot \mathbf{A} \vec{p}_m$ .
6. Compute  $e_m = \|\mathbf{A}^* \vec{r}_{m+1}\|_2^2 / c_m$ , and update direction  $\vec{p}_{m+1} = \mathbf{A}^* \vec{r}_{m+1} + e_m \cdot \vec{p}_m$ .
7. Increment counter  $m = m + 1$ , and repeat steps 4 through 6 until one of the following termination conditions is satisfied:  $e_m = 0$ ,  $c_m$  is below a given threshold, or the number of iterations reached  $N$ .

Two main issues about this algorithm should be pointed out. First, the initial solution vector is chosen as the distorted image. Unlike any other initial selection, this particular choice uses the available information to ensure that the solution obtained after any number of iterations is better in the least-squares sense than the distorted object. This choice may also reduce the number of iterations needed to reach a given accuracy. Second, the termination conditions should ideally be that the norm of the residual  $\vec{r}_k$  goes to zero if the system has a full rank or when the parameter  $c_k$  goes to zero if the system is rank-deficient. Even though these conditions will eventually be met in a finite number of iterations, a large number of iterations amount to an insignificant improvement in the solution. In particular, when  $c_k$  is extremely small yet nonzero, the added correction term is multiplied by a very small value and hence do not amount to a noticeable change in the results. Therefore, in our implementation, the termination condition was set as  $c_k$  being smaller than a predetermined threshold.

In theory, the CGM reaches the unique solution or the minimal least square solution in less than  $N$  steps, where  $N$  is the size of the linear system [60]. Moreover, if the linear system matrix can be expressed as the sum of the identity matrix and another matrix  $\mathbf{C}$  of rank  $r_C$ , then the algorithm converges in no more than  $r_C + 1$  steps. Hence, the convergence is fast in general and only a few steps may be needed to reach a reasonable accuracy. The complexity of this method is estimated as  $O(N^2)$  flops/iteration/line, which can be significantly lower than that of SVD when a few iterations are used.

The computational load of the CGM can be traded off with the solution accuracy in the following manner. With a constraint on computation time, the termination condition can be modified to be the maximum number of iterations that are allowed within this time. In this case, the solution is considered optimal in the least-squares sense for the given number of iterations. This direct control over the time/accuracy trade-off is not available with many other techniques such as SVD where the correction process cannot be divided into independent pieces and the algorithm must proceed to the end regardless of the accuracy required.

#### 4.4.3 Solution constraining

When the linear system matrix is ill-conditioned, it is always advantageous to impose certain constraints on the solution based on *a priori* information about the physical system being imaged. In general, constraining improves the accuracy of the result and amounts to regularization in some cases. The type of constraints that can be useful for our problem is linear equality constraints, which are often invoked when certain parts of the field of view are known *a priori*. For example, when the field of view is larger than the imaged object, equality constraints can be applied to force the solution at the points outside the object boundaries to be zero. In general, equality constraints can be expressed as  $\mathbf{B} \cdot \vec{x} = \vec{d}$ , where  $\mathbf{B}$  is a  $P \times N$  full-rank matrix and  $\vec{d}$  is a  $P$ -dimensional vector. The exact application of the general form of this equation involves

a QR decomposition step, which is rather computationally prohibitive, especially when the solver is chosen to be the conjugate gradient method [62]. Nevertheless, when  $\mathbf{B}$  matrix is diagonal, the solution method can be modified. Nevertheless, in practice, it is sufficient to adhere to the constraints only approximately. This allows the constraints to be invoked with only a small added complexity. This can be done by concatenating the constraint equation to the original linear system with a weighting factor and the composite system is then solved. In this case, it can be shown that the solution satisfies the constraint more closely as the weighting factor gets larger. It should be noted, however, that numerical stability can be affected rather severely for large values of this weighting factor. A reasonable value for this parameter is of the order of the estimated average singular value of the linear system matrix, usually of the order of 10. When  $\mathbf{B}$  matrix is diagonal, the solution method can be modified to solve only for all pixels that are not assigned values by the constraints. In this case, the solution satisfies the constraints in the exact sense.

Unlike linear constraints which impose localized conditions on individual pixel values, quadratic constraints describe global conditions that must be satisfied by the 2-norm of the solution. These constraints are particularly useful when the solution is ill-conditioned where imposing the quadratic constraints amounts to a regularization. In its general form, the quadratic constraints can be expressed as:  $\|\mathbf{B} \cdot \vec{x} - \vec{d}\|_2 \leq \alpha$ , where  $\mathbf{B}$  is a full rank  $P \times N$  matrix,  $\vec{d}$  is a  $P$ -dimensional vector and  $\alpha$  is a prespecified limiting value. For our problem,  $\mathbf{B}$  is the identity matrix and  $\vec{d}$  is zero, and the linear system solution is therefore constrained to lie within a sphere of radius  $\alpha$ . In this case, the solution method amounts to adding an identity matrix multiplied by a factor to the solution, which is exactly what regularization does [62]. It should be noted however that imposing such constraints requires the SVD of the linear system matrix to be available. Therefore, its application may be practical only with SVD solvers where it can be used instead of TSVD to compute the regularized solution. However, since there is no direct relationship between the norms of the distorted and original

objects, there is no particular advantage for any of the two method over the other.

## 4.5 Experimental Results

The reconstruction methods described here were applied to experimental data of different phantoms and human volunteers on a 1.5T Siemens Magnetom Vision MR scanner. The images were acquired using a blipped-EPI sequence or a segmented EPI with centric reordering with a TE of 70ms and a TR of 200 ms. The FOV was  $31\text{cm} \times 31\text{cm}$  and the matrix size used was  $128 \times 128$ . The field maps were derived from two gradient-echo FLASH images with a 3 ms difference in echo time. In Fig.(4.1), the results of using different discretization methods with a CGM solver on phantom data are illustrated. The  $B_0$  variation was in the range  $-66$  to  $+210$  Hz. As can be shown, the piecewise constant intensity models with constant or linear inhomogeneities look rather blurred. The reason for that is the apodization of the k-space values imposed by these models. In general, the quality of the midpoint discretization looks better and it seems that this model better represents practical data. In Fig.(4.2), the results of using a 2-step CGM iteration on human data obtained with blipped-EPI are illustrated. The off-resonance frequencies in these images varied in the range  $-94$  to  $+100$  Hz for the coronal scan and from  $-100$  to  $+100$  Hz for the sagittal scan. The system matrix was composed of two scans with opposite traversal directions to obtain a full-rank composition. By comparison to the FLASH images, it can be seen that the correction visibly improves the geometric accuracy in both coronal and sagittal images. In Fig.(4.3), a comparison between the quality of the obtainable correction with blipped-EPI and segmented EPI with centric reordering as examples of linear and non-linear trajectory sequences. The range of  $B_0$  variation was between  $-164$  and  $+167$  Hz. Even though the images obtained with the latter sequence exhibit more severe distortion artifacts combining shift and blur, the quality of corrected images from this sequence is superior to that with blipped-EPI. This is

in full agreement with the theoretical prediction. Also, Figs.(4.4) and (4.5) confirm the same conclusion in human data of coronal and sagittal scans of a normal human volunteer. The ranges of  $B_0$  variation in these images were from  $-94$  to  $+100$  Hz for the coronal scan and from  $-100$  to  $+100$  Hz for the sagittal scan.

## 4.6 Discussion

In practice, the experimental information is usually contaminated with additive noise. As a result, the processes of eigen- and singular value decomposition are perturbed by this noise thus producing all non-zero eigenvalue and singular value sets even when the operator is singular. In this case, the theoretical null space is equivalent to the noise subspace that can be detected using one of many likelihood ratio criteria. If a zero-mean white Gaussian noise model is assumed, this detection process amounts to a simple absolute value thresholding to the obtained eigenvalues or singular values as in TSVD. It is also important to consider the contamination of field maps with noise and its effect on the reconstruction. To assess this problem, a combination of measurements and simulations were performed to arrive at the following observations. After performing a number of independent field mapping measurements for the same slice, the results from all measurements were found to be within only 4% from their average, assumed to be closest to the true field map. From computer simulations, it was evident that when the field map values are within 5% of the original values, fairly accurate reconstruction is expected. Therefore, the results from the field mapping procedure can be generally considered stable. Smoothing and low intensity masking of field maps were also found to be of important value to improve the stability of the procedure even further.

When the matrix operator takes the form of a Vandermonde matrix as in the above example, the first solver that comes to mind is the Vandermonde matrix solver proposed by Bjork and Pereyra [57] which is known for its reduced complexity. How-

ever, when the Vandermonde matrix form is ill-conditioned or rank-deficient as with cases of severe inhomogeneity, this solver cannot be used since regularization disrupts the characteristic form of the matrix used to derive this solver. Without regularization, the solution becomes dominated by numerical instabilities that are functions not only of the condition number of the system matrix but also of the machine epsilon [58]. Therefore, this solver cannot be used for our application because of its lack of robustness.

Two important features should be noted about the SVD solution method. First, it explicitly computes the inverse operator and in doing that, it requires only information about the system matrix  $\mathbf{A}$ . It is not necessary to have the data vector containing the outcome of applying the operator at this point. Given that the matrix operator is usually estimated by field mapping before the actual acquisition of the distorted data, the process of SVD computation can be performed even before the actual data acquisition, assuming perfect registration between the field map and the subject imaged subsequently. The second important feature of SVD is that it explicitly identifies the null space of the matrix operator. Hence, when a number of k-space traversal methods are available for data acquisition, they can be compared based on the dimensionality of their corresponding null spaces. In other words, it is possible to make *a priori* determination of the scanning method that would yield the best solution in one scan. For example, if the operator matrix forms for blipped-EPI and segmented EPI with centric reordering sequences are examined, it can be shown that the the latter is more stable and is therefore expected to maintain full rank under the same conditions that causes the former to be rank-deficient. Moreover, if a full-rank solution is required, it is possible to devise a k-space traversal strategy to provide a full-rank operator equation from several scans. In this case, the tradeoff between the amount of acquired data and the solution accuracy can be directly addressed with this method. Although this solver is flexible, it is associated with a rather high computational complexity ( $O(N^3)$  flops/line) that is a determining disadvantage in

many situations.

As suggested by the theory, given a field map, it is possible to compare the performance of different scanning sequences prior to the actual data acquisition by comparing the condition numbers of their system matrices. An interesting observation in this aspect is that only linear trajectory sequences may have rank-deficient system matrices. This is a direct result of their linear phase evolution characteristics, which are quite similar to those of the Fourier transform matrix columns. With other nonlinear scanning sequences such as segmented EPI or spiral, the phase evolution characteristics are rather distinct from those of Fourier vectors and, hence, their system matrices are of full-rank. Hence, our theoretical result indicate that the use of non-linear k-space trajectories provides better reconstructions under  $B_0$  inhomogeneity.

It should be noted that the CGM does not explicitly identify the null space of the system and the remaining residual after algorithm termination lies in that space. It is therefore not possible to define the null space using CGM. As a result, this method cannot be used to derive a strategy for full-rank system composition from oversampling as with SVD. Also, CGM requires that the result of applying the operator in addition to the field mapping information be available before the algorithm starts, which is again in contrast with SVD.

An interesting special case of the CGM procedure occurs when only one iteration is used. In this case, the conjugate gradient method amounts to an approximate correction method similar to the conjugate phase method proposed by Maeda et al [30]. In fact, it can be shown that the conjugate phase method is a special case of the conjugate gradient iterative solver when the initial solution is zero and the number of iterations is exactly one. Hence, several strategies can be proposed to take advantage of this observation. First, a generalized multi-step conjugate phase method can be directly implemented by using the conjugate gradient iterations. An alternative approach to the conjugate phase method can also be proposed when the

initial solution is chosen to be the distorted object. The possible advantage of using this method is the guaranteed lower error norm. This is not generally the case with the conjugate phase method.

Even though the computational complexity of the SVD solver seems rather prohibitive in general, this might not be the case for applications where repeated images of the same slices are obtained. For example, in functional imaging (fMRI), a time sequence of as many as hundreds of acquisitions of the same slice is obtained to assess brain activation during the time course of an experiment. In this case, SVD inverse matrix operator can be computed once and used to correct all images in the time sequence. The resultant complexity will be comparable to that of the conjugate phase method while maintaining the least-squares optimality of the correction.

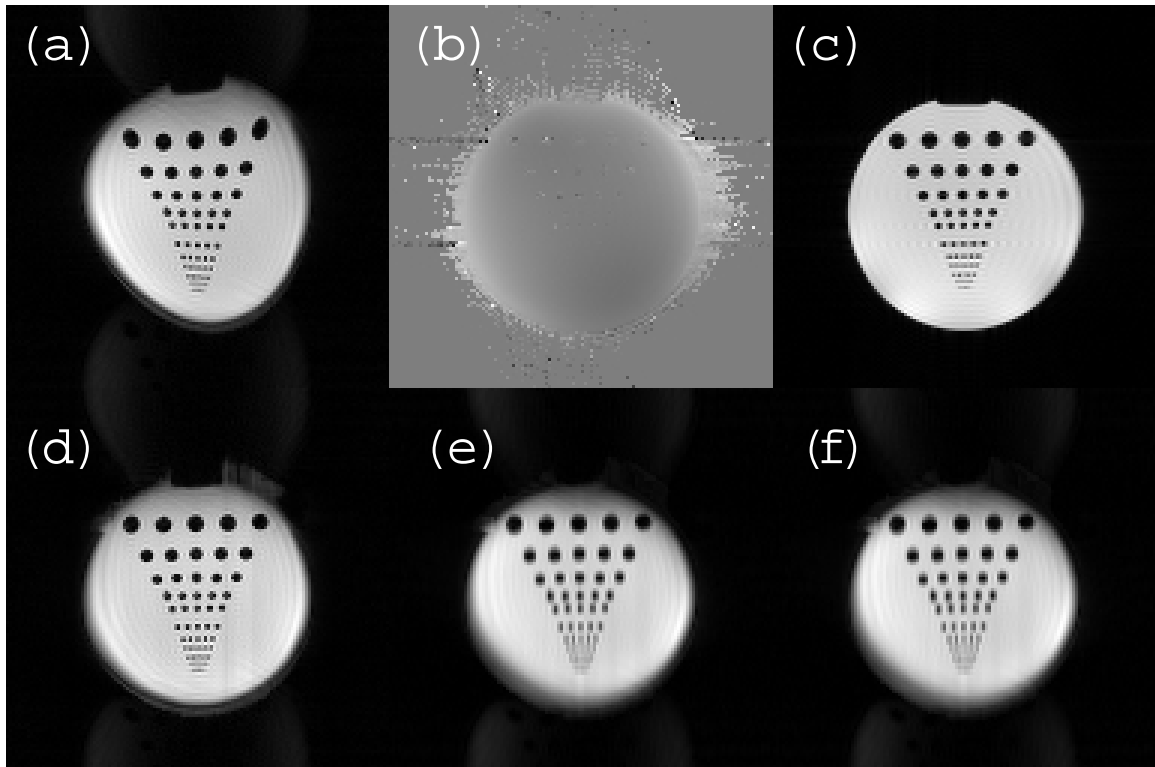


Figure 4.1: Comparison of different discretization methods as applied to correcting phantom data collected with blipped-EPI sequence. (a) Distorted EPI image. (b) Field map. (c) Comparison FLASH image. (d) corrected image using midpoint discretization model. (e) corrected image using piecewise constant intensity model and piecewise constant inhomogeneity. (f) corrected image using piecewise constant intensity model and piecewise linear inhomogeneity.

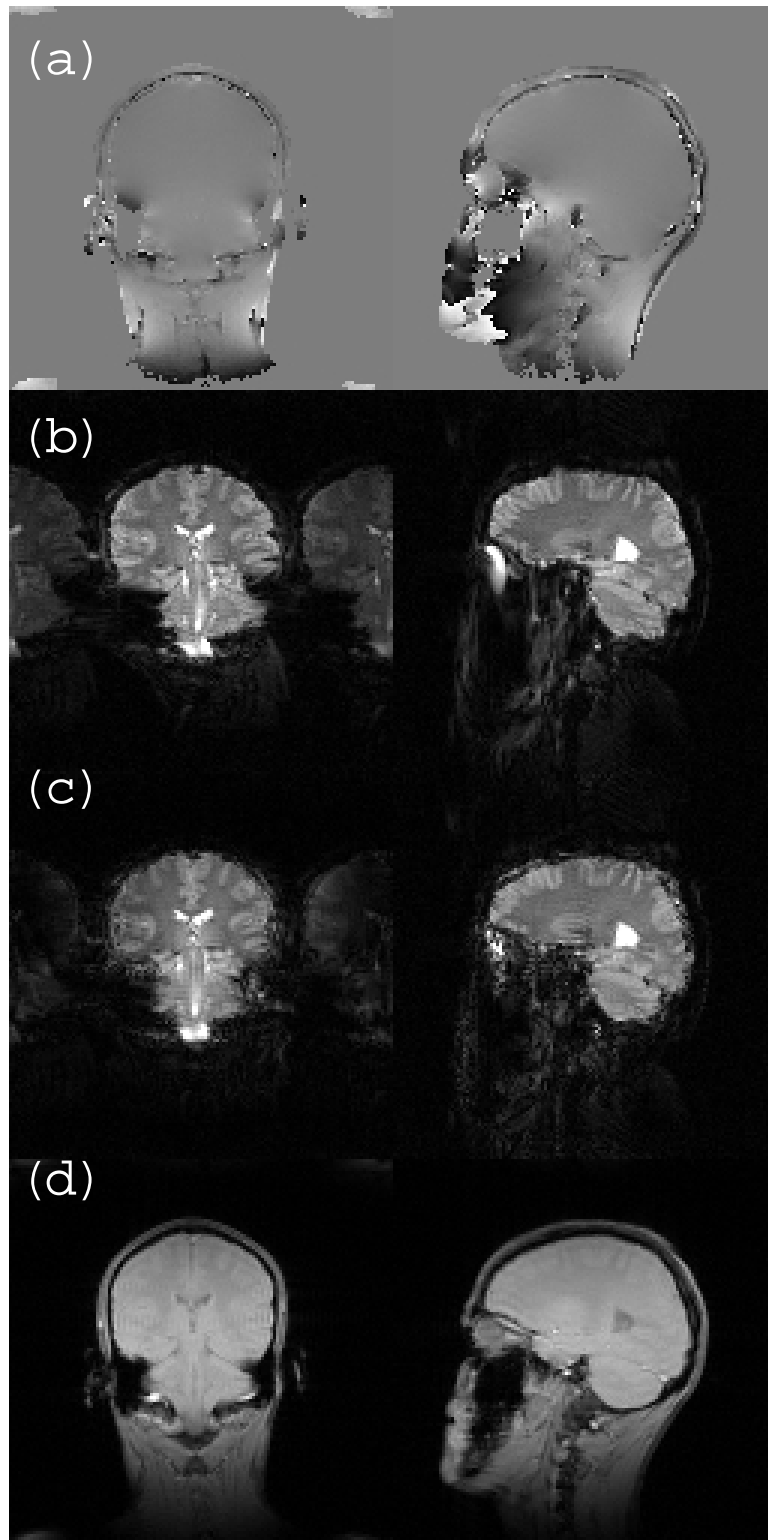


Figure 4.2: Correction of human data with 2-step conjugate gradient iteration. (a) Field maps. (b) Distorted images. (c) corrected images. (d) FLASH comparison images.

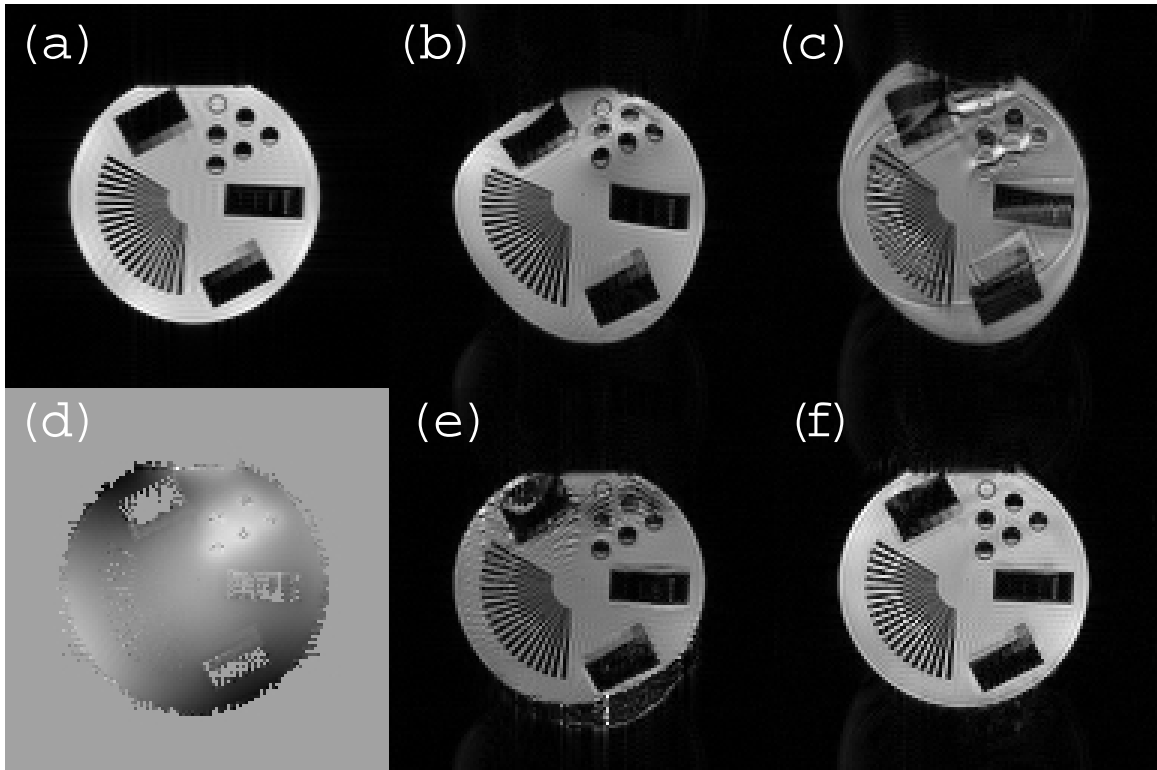


Figure 4.3: Comparison of blipped-EPI and segmented EPI with centric reordering for phantom data. The FLASH comparison image and the field map are shown in plates (a) and (d) respectively. The distorted and SVD corrected images with blipped-EPI are shown in plates (b) and (e), while those in (c) and (f) are for segmented EPI with centric reordering.

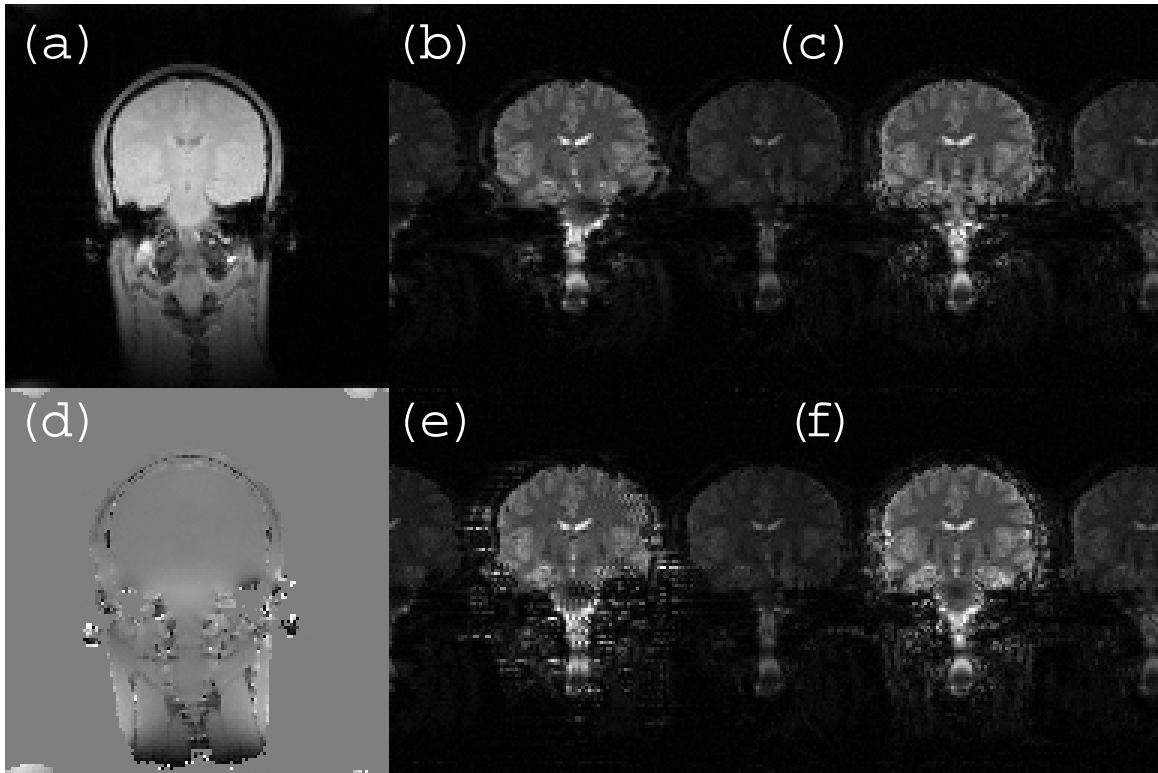


Figure 4.4: Comparison of blipped-EPI and segmented EPI with centric reordering for a coronal human brain scan. The FLASH comparison image and the field map are shown in plates (a) and (d) respectively. The distorted and SVD corrected images with blipped-EPI are shown in plates (b) and (e), while those in (c) and (f) are for segmented EPI with centric reordering.

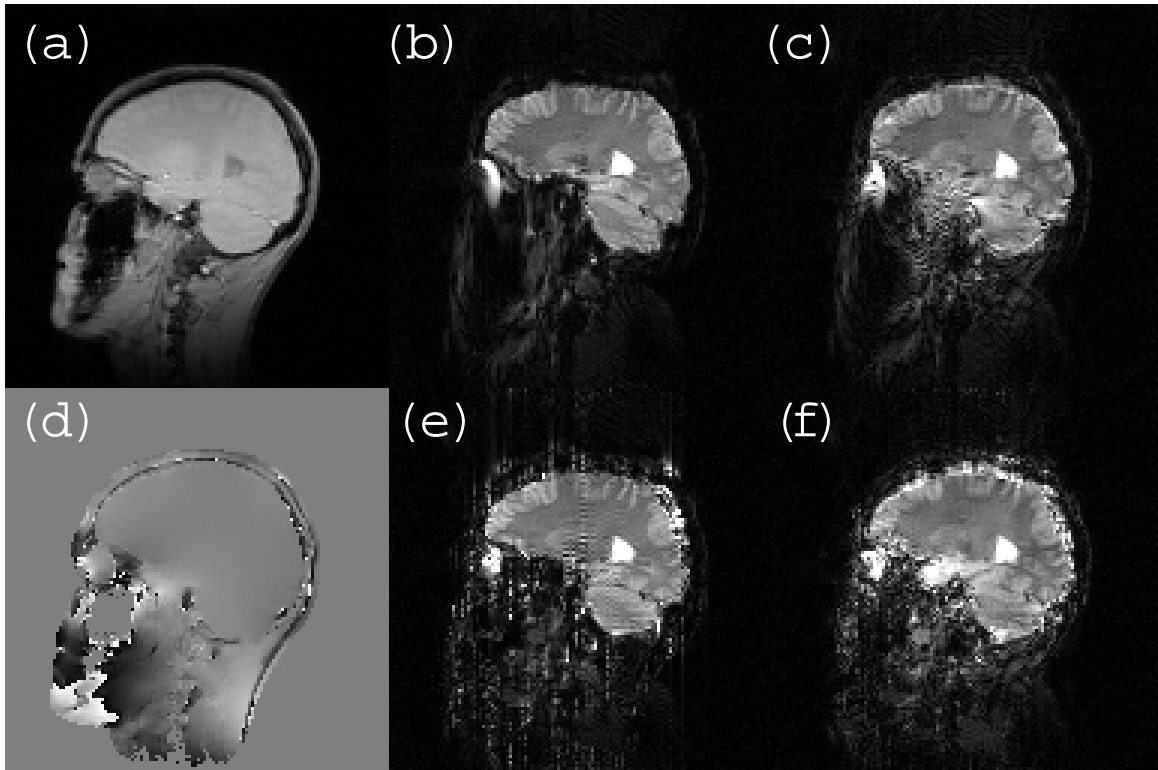


Figure 4.5: Comparison of blipped-EPI and segmented EPI with centric reordering for a sagittal human brain scan. The FLASH comparison image and the field map are shown in plates (a) and (d) respectively. The distorted and SVD corrected images with blipped-EPI are shown in plates (b) and (e), while those in (c) and (f) are for segmented EPI with centric reordering.

## Chapter 5

### CONCLUSIONS

Three novel reconstruction techniques have been discussed in this thesis. First, The theory and experimental verification of a new spatial encoding technique, the pseudo-Fourier imaging (PFI), was presented. This technique is based on a uniform sampling of the phase-space on a Gabor grid and allows for controlled mixing of selective excitation and Fourier encoding. The technique has potential applications in many areas such as volume imaging, magnetic resonance angiography, and dynamic imaging.

The second technique is for reducing  $B_0$  inhomogeneity-induced degradation in MR images. The technique utilizes simulated phase rewinding to generate a corrected k-space data based on the initial estimate of the image and an estimate of the field map. A theoretical analysis of the technique shows that it is exact under ideal conditions of non-overlapping spatial distortions or constant field inhomogeneity within these distortions. Under practical circumstances, the technique provides a good approximation to the exact correction and its accuracy improves uniformly as the ideal conditions are approached or the field inhomogeneity becomes smoother. The technique was verified on a resolution phantom and successfully applied to head images from normal human subjects. Experimental studies have demonstrated that it is robust for a variety of sequences.

Finally, stable algebraic reconstruction for magnetic resonance imaging under severe magnetic field inhomogeneity were formulated and experimentally demonstrated. This reconstruction can be applied to all imaging sequences in which the inhomogeneity distortion is much more severe along one of the image dimensions. The new

approach is based on estimating the operator that produces the distorted images and computing least-squares inverse operators that can be applied to correct distorted images. The corrected images are therefore optimal in the Frobenius norm sense. This formalism allows the theoretical comparison of imaging sequences with different trajectories in terms of the image quality after the reconstruction under  $B_0$  inhomogeneity. This analysis suggests that non-linear k-space trajectory sequences such as segmented EPI with centric reordering provide better results than linear trajectory sequences as blipped-EPI.

Based on the results of this thesis, further research can be proposed in the following points:

- The application of pseudo-Fourier imaging (PFI) in magnetic resonance angiography can be further optimized by conducting more studies on normal human volunteers and then on patients. The parameters of the imaging sequence that need to be optimized are the width of the imaging window, slice excitation sequencing,  $TR$  as related to contrast, and the use of magnetization transfer pulses.
- The application of pseudo-Fourier imaging in dynamic imaging can be further investigated by human studies. The use of multi-dimensional selective excitation pulses in order to enable the use of the new technique in 2-D can be attempted to enhance the practicality of the technique.
- The implementation of simulated phase evolution rewinding (SPHERE) on single-instruction multiple-data (SIMD) parallel computing machines is possible and can help speed up the reconstruction using this method.
- Motion models can be directly included in the algebraic model in order to make it more general. The solution methods should still be the same after this change.

- The extension of the reconstruction techniques in this thesis to three-dimensions can be investigated. For example, instead of using SPHERE for multi-slice phase correction, it can be used in a volumetric fashion for use with 3-D EPI sequences.
- The application of MRI in stereotactic neurosurgery and radiotherapy treatment planning can be re-investigated. In particular, studies to compare the geometric accuracy of corrected MRI images to those of CT can be conducted for each of these applications.
- The application of simulated phase evolution rewinding and algebraic reconstruction in the area of functional magnetic resonance imaging can be examined. In particular, the value of the new techniques in reducing the misregistration problem often encountered between functional maps and anatomical images in anatomic referencing should be assessed with regard to the implementation and the accuracy of registration as compared to the required computational overhead.

## BIBLIOGRAPHY

- [1] A.L. Horowitz, *MRI physics for radiologists - a visual approach, 3rd ed.*, Springer-Verlag, New York, 1995.
- [2] P.T. Callaghan, *Principles of nuclear magnetic resonance microscopy*, Clarendon Press, Oxford, 1991.
- [3] M.J. Bronskill and P. Sprawls, eds., *The physics of MRI: 1992 AAPM summer school proceedings*, AAPM, 1992.
- [4] J. Michiels, H. Bosmans, P. Pelgrims, D. Vandermeulen, J. Gybels, G. Marchal, and P. Suetens, "On the problem of geometric distortion in magnetic resonance images for stereotactic neurosurgery," *Magn. Reson. Med.*, vol. 12, pp. 749-765, 1994.
- [5] E. Piovan, P.G. Zampieri, F. Alessandrini, M.A. Gerosa, A. Nicolato, A. Pasoli, R. Foroni, M.G. Giri, A. Bricolo, and A. Benati, "Quality assessment of magnetic resonance stereotactic localization for gamma knife radiosurgery," *Stereotact. Funct. Neurosurg.*, vol. 64 (suppl. 1), pp. 228-232, 1995.
- [6] M.A. Moerland, R. Beersma, R. Bhagwandien, H.K. Wijrdeman, and C.J.G. Bakker, "Analysis and correction of geometric distortions in 1.5T magnetic resonance images for use in radiotherapy treatment planning," *Phys. Med. Biol.*, vol. 40, pp. 1651-1664, 1995.
- [7] L.R. Schad, H.-H. Ehricke, B. Wowra, G. Layer, R. Engenhart, H.-U. Kauczor, H.-J. Zabel, G. Brix, and W.J. Lorenz, "Correction of spatial distortion in magnetic resonance angiography for radiosurgical treatment planning of cerebral arteriovenous malformations," *Magn. Reson. Imag.*, vol. 10, pp. 609-621, 1992.
- [8] Y.M. Kadah and X. Hu, "Pseudo-Fourier Imaging: A novel approach for spatial encoding in MRI," *Proc. ISMRM-96*, New York, May 1996.
- [9] Y.M. Kadah and X. Hu, "Pseudo-Fourier Imaging (PFI): A technique for spatial encoding in MRI," *submitted to IEEE Trans. Med. Imag.*, December 1996.

- [10] Y.M. Kadah and X. Hu, "Pseudo-Fourier Imaging (PFI): A technique for spatial encoding in MRI," *U.S. Patent Pending*.
- [11] D.L. Parker, C. Yuan, and D.D. Blatter, "MR angiography by multiple thin slab 3D acquisition," *Magn. Reson. Med.*, vol. 17, pp. 434-451, 1991.
- [12] D.M. Healy, Jr. and J.B. Weaver, "Two applications of wavelet transforms in magnetic resonance imaging," *IEEE Trans. Info. Theory*, vol. 38, no. 2, pp. 840-860, 1992.
- [13] G.P. Zientara, L.P. Panych, and F.A. Jolesz, "Dynamically adaptive MRI with encoding by singular value decomposition," *Magn. Reson. Med.*, vol. 32, pp. 268-274.
- [14] A.I. Zayed, *Advances in Shannon's Sampling Theory*, CRC Press, London, 1993.
- [15] P.P. Vaidyanathan, *Multirate Systems and Filter Banks*, Printice-Hall, New Jersey, 1993.
- [16] E.T. Jaynes, "Matrix treatment of nuclear induction," *Physical Review*, vol. 98, no. 4, pp. 1099-1105, 1955.
- [17] J.J. van Vaals, M.E. Brummer, W.T. Dixon, H.H. Tuithof, H. Engels, R.C. Nelson, B.M. Gerety, J.L. Chezmar, J.A. den Boer, "Keyhole method for accelerating imaging with contrast agent uptake," *J. Magn. Reson. Imag.*, vol. 3, pp. 671-675, 1993.
- [18] X. Hu and T. Parrish, "Reduction of field of view for dynamic imaging," *Magn. Reson. Med.*, vol. 31, pp. 691-694, 1994.
- [19] L.P. Panych and F.A. Jolesz, "A dynamically adaptive imaging algorithm for wavelet-encoded MRI," *Magn. Reson. Med.*, vol. 32, pp. 738-748, 1994.
- [20] L.P. Panych, P.D. Jacob, and F.A. Jolesz, "Implementation of wavelet-encoded MR imaging," *J. Magn. Reson. Imag.*, pp. 649-655, 1993.
- [21] L.P. Panych, C. Oesterle, G.P. Zientara, and J. Hennig, "Implementation of a fast gradient-echo SVD encoding technique for dynamic imaging," *Magn. Reson. Med.*, vol. 35, pp. 554-562, 1996.
- [22] J. Frahm, A. Haase, and D. Matthaei, "Rapid three-dimensional MR imaging using the FLASH technique," *J. Comput. Assist. Tomogr.*, vol. 10, no. 2, pp.363-8, 1986.

- [23] Y.M. Kadah and X. Hu, "Simulated phase evolution rewinding (SPHERE): a technique for reducing  $B_0$  inhomogeneity effects in MR images," *To appear in Proc. ISMRM-97*, Vancouver, Canada, April 1997.
- [24] Y.M. Kadah and X. Hu, "Simulated phase evolution rewinding (SPHERE): a technique for reducing  $B_0$  inhomogeneity effects in MR images," *To appear in Magn. Reson. Med.*, 1997.
- [25] K. Sekihara, M. Kuroda, and H. Kohno, "Image restoration from non-uniform magnetic field influence for direct Fourier NMR imaging," *Phys. Med. Biol.*, vol. 29, pp. 15-24, 1984.
- [26] Y.M. Ro, and Z.-H. Cho, "Susceptibility magnetic resonance imaging using spectral decomposition," *Magn. Reson. Med.*, vol. 33, pp. 521-528, 1995.
- [27] K. Sekihara, S. Matsui, and H. Kohno, "NMR imaging for magnets with large nonuniformities," *IEEE Trans. Med. Imag.*, vol. MI-4, pp. 193- 199, 1985.
- [28] K. Sekihara and H. Kohno, "Image restoration from nonuniform static field influence in modified echo-planar imaging," *Med. Phys.*, vol. 14, pp. 1087-1089, 1987.
- [29] P. Jezard and R.S. Balaban, "Correction for geometric distortion in echo planar images from  $B_0$  field variations," *Magn. Reson. Med.*, vol. 34, pp. 65-73, 1995.
- [30] A. Maeda, K. Sano, and T. Yokoyama, "Reconstruction by weighted correlation for MRI with time-varying gradients," *IEEE Trans. Med. Imag.*, vol. 7, pp. 26-31, 1988.
- [31] R.M. Weisskoff and T.L. Davis, "Correcting gross distortions on echo planar images," *Proc. SMRM 11th Annual Meeting*, Berlin, pp. 4515, 1992.
- [32] H. Chang and J.M. Fitzpatrick, "A technique for accurate magnetic resonance imaging in the presence of field inhomogeneity," *IEEE Trans. Med. Imag.*, vol. 11, pp. 319-329, 1992.
- [33] R. Bowtell, D.J.O. McIntyre, M.-J. Commandre, P.M. Glover, and P. Mansfield, "Correction of geometric distortion in echo planar images," *Proc. SMR 2nd Meeting*, San Francisco, pp. 411, 1994.
- [34] S. Kim, X. Hu, G. Adriany, and K. Ugurbil, "Fast interleaved echo-planar imaging with navigator: high resolution anatomic and functional images at 4 Tesla," *Magn. Reson. Med.*, vol. 35, pp. 895-902, 1996.

- [35] D.A. Feinberg and K. Oshio, "GRASE (gradient- and spin-echo) MR imaging: a new fast clinical imaging technique," *Radiology*, vol. 181, pp. 597-602, 1991.
- [36] J.P. Mugler III and J.R. Brookeman, "Off-resonance image artifacts in interleaved-EPI and GRASE pulse sequences," *Magn. Reson. Med.*, vol. 36, pp. 306-313, 1996.
- [37] D.C. Noll, C.H. Meyer, J.M. Pauly, D.G. Nishimura, and A. Macovski, "A homogeneity correction method for magnetic resonance imaging with time-varying gradients," *IEEE Trans. Med. Imag.*, vol. 10, pp. 629-637, 1991.
- [38] D.C. Noll, J.M. Pauly, C.H. Meyer, D.G. Nishimura, and A. Macovski, "Deblurring for non-2d Fourier transform magnetic resonance imaging," *Magn. Reson. Med.*, vol. 25, pp. 319-333, 1992.
- [39] P. Irarrazabal, C.H. Meyer, D.G. Nishimura, and A. Macovski, "Inhomogeneity correction using an estimated linear field map," *Magn. Reson. Med.*, vol. 35, pp. 278-282, 1996.
- [40] M. Tincher, C.R. Meyer, R. Gupta, and D.M. Williams, "Polynomial modeling and reduction of RF body coil spatial inhomogeneity in MRI," *IEEE Trans. Med. Imag.*, vol. 12, no. 2, pp. 361-365, 1993.
- [41] L.-C. Man, J.M. Pauly, and A. Macovski, "Correcting severe local inhomogeneity blurs by spatially variant deconvolution," *Proc. SMRM 3rd Annual Meeting, Nice*, pp.738, 1995.
- [42] B. Choudhary and S. Nanda, *Functional Analysis with Applications*, John Wiley & Sons, New York, 1989.
- [43] J.M. Tribolet, "A new phase unwrapping algorithm," *IEEE Trans. Acous. Speech Sign. Proc.*, vol. ASSP-25, pp. 170-177, 1977.
- [44] C.J. Hardy and H.E. Cline, "Broadband nuclear magnetic resonance pulses with two-dimensional spatial selectivity," *J. Appl. Phys.*, vol. 66, pp. 1513-1516, 1989.
- [45] C.H. Meyer, B.S. Hu, D.G. Nishimura, and A. Macovski, "Fast spiral coronary artery imaging", *Magn. Reson. Med.*, vol. 28, pp. 202-213, 1992.
- [46] X. Hu and T.H. Le, "Artifact reduction in EPI with phase-encoded reference scan," *Magn. Reson. Med.*, vol. 36, pp. 166-171, 1996.

- [47] A.V. Oppenheim and R.W. Schaffer, *Discrete-Time Signal Processing*, Prentice Hall, New Jersey, 1989.
- [48] B.P. Lathi, *An Introduction to Random Signals and Communications Theory*, International Textbook Co., Scranton, 1968.
- [49] Y.M. Kadah and X. Hu, "Algebraic reconstruction for magnetic resonance imaging under  $B_0$  inhomogeneity," *Submitted to J. Magn. Reson.*, April 1997.
- [50] Y.M. Kadah and X. Hu, "Algebraic reconstruction for magnetic resonance imaging under  $B_0$  inhomogeneity," *To appear in Proc. ISMRM-97*, Vancouver, Canada, April 1997.
- [51] F. Farzaneh, S.J. Riederer, and N.J. Pelc, "Analysis of T2 limitations and off-resonance effects on spatial resolution and artifacts in echo-planar imaging," *Magn. Reson. Med.*, vol. 14, pp. 123-139, 1990.
- [52] T. Sumanaweera, G. Glover, S. Song, J. Adler, and Sandy Napel, "Quantifying MRI geometric distortion in tissue," *Magn. Reson. Med.*, vol.31, pp. 40-47, 1994.
- [53] T.S. Sumanaweera, G.H. Glover, T.O. Binford, and J.R. Adler, "MR susceptibility misregistration correction," *IEEE Trans. Med. Imag.*, vol. 12, no. 2, pp. 251-259, 1993.
- [54] A. Bakushinsky and A. Goncharsky, *Ill-posed problems: theory and applications*, Kluwer Academic Publishers, London, 1994.
- [55] U. Schendel, *Sparse Matrices*, John Wiley and Sons, New York, 1989.
- [56] C.W. Groetsch, *Inverse problems in the mathematical sciences*, Vieweg, Braunschweig/wiesbaden, 1993.
- [57] A. Bjorck and V. Pereyra, "Solution of Vandermonde systems of equations," *Mathematics of Computation*, vol. 24, pp.893-903, 1970.
- [58] W. Gautchi, "Optimally conditioned Vandermonde matrices," *Numerische Mathematische*, vol. 24, pp.1-12, 1975.
- [59] M.R. Hestenes and E. Stiefel, "Methods of conjugate gradients for solving linear systems," *J. Research Nat. Bur. Standards*, vol. 49, pp.409-436, 1952.

- [60] M.R. Hestenes, *Conjugate direction methods in optimization*, Springer-Verlag, Heidelberg, 1980.
- [61] G. Heinig and K. Rost, *Algebraic methods for Toeplitz-like matrices and operators*, Birkhauser Verlag, Stuttgart, 1984.
- [62] G.H. Golub and C.F. Van Loan, *Matrix Computations*, The Johns Hopkins University Press, Baltimore, 1989.